

Rochester Institute of Technology

**RIT Digital Institutional Repository**

---

Theses

---

1-2013

## **Subwavelength Surface Plasmons Based on Novel Structures and Metamaterials**

Ruoxi Yang

Follow this and additional works at: <https://repository.rit.edu/theses>



Part of the [Nanoscience and Nanotechnology Commons](#)

---

### **Recommended Citation**

Yang, Ruoxi, "Subwavelength Surface Plasmons Based on Novel Structures and Metamaterials" (2013). Thesis. Rochester Institute of Technology. Accessed from

This Dissertation is brought to you for free and open access by the RIT Libraries. For more information, please contact [repository@rit.edu](mailto:repository@rit.edu).

**SUBWAVELENGTH SURFACE PLASMONS BASED ON  
NOVEL STRUCTURES AND METAMATERIALS**

by

RUOXI YANG

A DISSERTATION

Submitted in partial fulfillment of the requirements  
For the degree of Doctor of Philosophy  
in  
Microsystems Engineering  
at the  
Rochester Institute of Technology

January 2013

Author: \_\_\_\_\_  
Microsystems Engineering Program

Certified by: \_\_\_\_\_  
Zhaolin Lu  
Assistant Professor of Microsystems Engineering

Approved by: \_\_\_\_\_  
Bruce W. Smith, Ph.D.  
Director of Microsystems Engineering Program

Certified by: \_\_\_\_\_  
Harvey J. Palmer, Ph.D.  
Dean, Kate Gleason College of Engineering

# NOTICE OF COPYRIGHT

© 2013

**Ruoxi Yang**

## **REPRODUCTION PERMISSION STATEMENT**

Permission Granted

### **TITLE:**

**“SUBWAVELENGTH SURFACE PLASMONS BASED ON NOVEL STRUCTURES AND METAMATERIALS”**

I, Ruoxi Yang, hereby grant permission to the Wallace Library of the Rochester Institute of Technology to reproduce my dissertation in whole or in part. Any reproduction will not be for commercial use or profit.

Signature of Author: \_\_\_\_\_ Date: \_\_\_\_\_

# Subwavelength Surface Plasmons Based on Novel Structures and Metamaterials

By

Ruoxi Yang

Submitted by Ruoxi Yang in partial fulfillment of the requirements for the degree of Doctor of Philosophy in Microsystems Engineering and accepted on behalf of the Rochester Institute of Technology by the dissertation committee.

We, the undersigned members of the Faculty of the Rochester Institute of Technology, certify that we have advised and/or supervised the candidate on the work described in this dissertation. We further certify that we have reviewed the dissertation manuscript and approve it in partial fulfillment of the requirements of the degree of Doctor of Philosophy in Microsystems Engineering.

## Approved by:

Dr. Zhaolin Lu \_\_\_\_\_ Date  
(Committee Chair and Dissertation Advisor)

Dr. Bruce W. Smith \_\_\_\_\_ Date

Dr. Michael Kotlarchyk \_\_\_\_\_ Date

Dr. Stefan F. Preble \_\_\_\_\_ Date

Dr. Zoran Ninkov \_\_\_\_\_ Date

MICROSYSTEMS ENGINEERING PROGRAM  
ROCHESTER INSTITUTE OF TECHNOLOGY

January 2013

## ABSTRACT

Kate Gleason College of Engineering  
Rochester Institute of Technology

**Degree:** Doctor of Philosophy                      **Program:** Microsystems Engineering

Name of Candidate: Ruoxi Yang

Title: Subwavelength Surface Plasmons Based on Novel Structures and Metamaterials

With the rapid development of nanofabrication technology and powerful computational tools over the last decade, nanophotonics has enjoyed tremendous innovation and found wide applications in ultrahigh-speed data transmission, sensitive optical detection, manipulation of ultra-small objects, and visualization of nanoscale patterns. Surface plasmon-based photonics (or plasmonics) merges electronics and photonics at the nanoscale, creating the ability to combine the superior technical advantages of photonics and electronics on the same chip. Plasmonics focuses on the innovation of photonic devices by exploiting the optical property of metals. In particular, the oscillation of free electrons, when properly driven by electromagnetic waves, would form plasmon-polaritons in the vicinity of a metal surface and potentially result in extreme light confinement, which may beat the diffraction limit faced by conventional photonic devices and enable greatly enhanced light-matter interactions at the deep subwavelength scale. The objective of this dissertation is to develop subwavelength or deep subwavelength plasmonic waveguides and explore their integration on conventional dielectric platforms for multiple applications. Three novel structures (or mechanisms) are employed to develop and integrate nanoplasmonic waveguides; each consists of one part of the dissertation. The first part of this dissertation covers the design, fabrication, and demonstration of two-dimensional and three-dimensional metal-insulator-metal plasmonic couplers for mode transformation between photonic and nanoplasmonic domains on the silicon-on-insulator platform. In particular, deep subwavelength plasmonic modes under 100-nm are achieved via end-fire coupling and adiabatic mode transformation at telecom wavelengths. The second part studies metallic gratings as spoof plasmonic waveguides hosting deep subwavelength surface propagation modes. Metallic gratings under different dielectric coatings are numerically investigated for terahertz and gigahertz regions. The third part proposes, explores, and experimentally demonstrates the “metametal” for super surface wave excitation based on multilayered metal-insulator stacks, where the dispersion of the supported surface modes can be engineered by insulator dopant films in a given metal. The final part discusses the potential applications of active plasmonics for optical sensing, modulation and photovoltaics.

Abstract Approval:

Committee Chair: \_\_\_\_\_

Program Director: \_\_\_\_\_

Dean, KGCOE: \_\_\_\_\_

## ACKNOWLEDGMENTS

I would like to thank my advisor Professor Zhaolin Lu for his generous support, detailed guidance and constant encouragement throughout my graduate studies at RIT. His expertise in optical science has greatly broadened my vision, and helped to establish plasmon optics as my major interest of study. His distinguished ability to envision complex physical models from an elegant and intuitive touch has shaped the way I approach any problem.

I am particularly grateful to Professor Bruce W. Smith for his effort as the department head to foresee the needs and monitor the progress of every doctoral student under the Microsystems Engineering program, including me, and his acute supervision as a dissertation committee member. I also wish to thank Professor Stefan F. Preble, Professor Michael Kotlarchyk and Professor Zoran Ninkov for serving on my dissertation committee, and for their generosity in sharing their invaluable ideas and all sorts of facility resources for the maximum good of my research.

The staff members at the Semiconductor & Microsystems Fabrication Laboratory (SMFL) deserve my sincere thanks as well. In particular, I would like to thank Mr. Sean O'Brien for his knowledge, willingness and readiness to help on almost everything related to micro-fabrications at any time. I would also like to thank staff members at Cornell NanoScale Science & Technology Facility (CNF) especially Mr. Daron Westly for their expertise and kindness.

I am grateful to the generous financial support for my research by various funding agencies, including the National Science Foundation (NSF), the Defense Advanced Research Projects Agency (DAPRA) and the American Chemical Society (ACS).

I am indebted to former and current nanophotonics group students Dr. Karthik Narayanan, Dr. Ali W. Elshaari, Mr. Abdelsalam A. Aboketaf and Mr. Liang Cao for guiding me into the LoboZZo Lab for sample preparation and measurement. I also want to express my greatest gratitude to Andrew Estroff for proofreading my dissertation. I'm grateful to Ms. Wangshi Zhao, Prof. Xiaoguang Liu at UC Davis and Mr. Ling Ouyang in Aptina Imaging Corp., not only for technical discussions but most importantly as my close friends. I wish all of them the best of luck all the way with their studies, future careers and personal lives.

Finally I would like to thank my parents, Mr. Xiaoying Yang and Ms. Daping Jiang, for their support of my education both mentally and economically. Without their love, dedication and sacrifice, none of this work can be accomplished.

## TABLE OF CONTENTS

1	Introduction.....	1
1.1	Motivation.....	2
1.2	Nanoplasmonic Waveguide .....	6
1.2.1	Metal Optics with Drude Model .....	7
1.2.2	Bulk Plasma and Surface Plasma.....	10
1.2.3	Metal-insulator-metal (MIM) Waveguides.....	15
1.2.4	Subwavelength Waveguiding by Periodic Structures.....	24
1.3	Plasmonic Materials and Fabrication Techniques .....	27
1.3.1	Metals.....	28
1.3.2	Compounds .....	29
1.3.3	Graphene and Others.....	30
1.4	Modeling Technique .....	31
1.4.1	Finite-Difference Time-Domain (FDTD) Method.....	32
1.4.2	Modeling Setup.....	35
1.5	Dissertation Overview .....	37
2	Integrated Plasmonic Coupling.....	40
2.1	Introduction.....	40
2.2	Design and Modeling.....	42
2.2.1	Mode resemblance: a mode-coupling consideration.....	42
2.2.2	Simulation results of a modified slot-to-slot coupling.....	46
2.3	Demonstration and Characterization.....	48
2.3.1	Sample preparation overview .....	48
2.3.2	Fabrication flow .....	49
2.3.3	Testing and measurement .....	51

2.4	Discussion .....	54
2.5	Conclusions .....	54
3	Nanoplasmonic Focusing in Three Dimensions .....	56
3.1	Introduction .....	56
3.2	Modeling Setup and Design .....	59
3.2.1	Motivation .....	59
3.2.2	Modeling setup for transmission calculation .....	59
3.2.3	Direct coupling in the vertical direction .....	60
3.2.4	Adiabatic tapering in the horizontal direction .....	62
3.3	Results and Discussion .....	64
3.3.1	Field confinement and enhancement .....	64
3.3.2	Mode conversion and Fabry-Perot effect .....	67
3.3.3	Discussion of potential applications .....	69
3.4	Conclusions .....	71
4	Integrated 3-Dimensional Plasmonic Mode Transformation .....	73
4.1	Introduction .....	73
4.2	Design and Modeling .....	75
4.2.1	Direct coupling for MIM waveguide .....	75
4.2.2	Practical interface for direct coupling .....	77
4.3	Fabrication Details .....	79
4.3.1	Sample preparation overview .....	79
4.3.2	Fabrication flow .....	80
4.3.3	Sample screening .....	83
4.4	Characterization and Discussion .....	85
4.5	Conclusions .....	86

5	Sp spoof Plasmonics in Coated Metallic Gratings .....	87
5.1	Introduction.....	87
5.2	Dispersion Calculation.....	89
5.2.1	Structure definition .....	89
5.2.2	Calculation detail .....	91
5.3	Mode Profile and Propagation Loss.....	93
5.4	Proposed fabrication steps .....	96
5.5	Conclusions.....	97
6	Multilayered Metal-Insulator Stacks Guiding Super Plasmon Waves.....	98
6.1	Introduction.....	98
6.2	Theoretical Analysis .....	100
6.2.1	Bounded surface waves for multilayer .....	100
6.2.2	Effective index method and effective surface plasmon frequency .....	101
6.2.3	Interpretation and numerical verification.....	105
6.3	Transfer-Matrix Method (TMM) .....	108
6.3.1	TMM review .....	108
6.3.2	An ESPF case study with TMM .....	110
6.4	Experimental Demonstration and Discussion.....	111
6.4.1	Experiment design .....	111
6.4.2	Preliminary experimental result.....	114
6.4.3	Discussion and data fitting.....	115
6.5	Further Numerical Modeling for ESPF Tuning.....	121
6.6	Conclusions.....	124
7	Active Plasmonics.....	125
7.1	Introduction.....	125

7.2	Approaches .....	126
7.3	Electric Field for Modulation.....	128
7.3.1	Background .....	128
7.3.2	Fabrication approach.....	130
7.4	Tunneling Diode for NIR Light Detector .....	132
7.4.1	Background .....	132
7.4.2	Theoretical evaluation.....	133
7.5	Plasmonic-enhanced Solar Cell Prototype.....	135
7.5.1	Background .....	135
7.5.2	Numerical analysis.....	137
7.5.3	Future Plan .....	143
7.6	Conclusions.....	145
8	Conclusions.....	147
8.1	Compact and efficient plasmonic coupling.....	147
8.2	Spoof plasmonics and indefinite metamaterials .....	149
8.3	Active plasmonics and future work .....	150
9	References.....	152
10	Appendices.....	170
10.A	Analytical solution of MIM waveguide.....	170
10.B	Matlab code to implement transfer matrix method, single layer case .....	170

## LIST OF FIGURES

Figure 1.1	The self-consistency condition for a dielectric waveguide. Original wave (red, solid) and its twice-reflected offspring (green, dashed) needs to be in phase to create an optical mode (adapted from Figure 8.1-2 of [20]).....	3
Figure 1.2	The growth of SP-related research in number of articles from 1980 to 2010, data acquired from Google Scholar ( <a href="http://scholar.google.com">http://scholar.google.com</a> , accessed on Feb 10, 2012). .....	6
Figure 1.3	Dielectric constants of (a) Aluminium, (b) Gold, (c) Copper and (d) Silver [34]. .....	9
Figure 1.4	Dispersion relation of free electron gas (solid) compared to that of lightline of dielectric material (dashed). .....	11
Figure 1.5	Definition of skin depths and their relation with propagation constant. The red curve sketches the magnetic field distribution. ....	13
Figure 1.6	Dispersion relation of SPP (solid) in metal-insulator configuration. The curve for the frequency between 0.707 and 1 denotes imaginary propagation constant. ....	13
Figure 1.7	Dispersion plot for MIM layered structure adapted from [16]. ....	16
Figure 1.8	Left: A typical MIM mode profile for 1550 nm light inside a 50nm-by-50nm air gap. The substrate and superstrate are silicon dioxide and air, respectively. Right: Propagation distance of the MIM mode for optical to NIR frequency [41]. .....	19

Figure 1.9	Transmission through sub-wavelength holes patterned in Ag as a function of wavelength (left) and illumination angle (right) [30].	22
Figure 1.10	Spoof plasmonics in PEC shown by dimension (left) and dispersion (right) [63].	25
Figure 1.11	The distribution of $E$ -field and $H$ -field components in a typical Cartesian Yee cell [84].	33
Figure 1.12	FDTD simulation setup for modeling a plasmonic cavity in Lumerical FDTD Solutions 7.5.	36
Figure 1.13	$H$ -Field intensity for the demo simulation shown in Figure 1.12.	37
Figure 2.1	(a) The power distribution in a dielectric slot waveguide. (b) The field distribution in a metal slot waveguide. Identical power flux is assumed for (a) and (b). The power density in MIM slot is obviously higher because of the presence of metal. (c) The field ( $ E_y $ ) comparison (line-scan from Figs. 1(a) and (b)) between dielectric and MIM slot. MIM slot exhibits better field confinement as expected.	42
Figure 2.2	An eigen-mode confined by (a) a 400nm by 300nm silicon core buried in the air or (b) 20nm by 20nm airgap between gold blocks for 1550 nm light.	44
Figure 2.3	Transverse $E$ -field profile of the quasi-TE mode in a SOI-based slot waveguide. (a) Contour of the $E$ -field amplitude and the $E$ -field lines. (b) 3-D surface plot of the $E$ -field amplitude. Adapted from [105].	45
Figure 2.4	(a) The layout of slot-to-slot coupler. (b) The power distribution from 2-D FDTD simulation for slot-to-slot coupler.	46

Figure 2.5	(a) The cross-section view of the quasi-MIM structure. (b) The cross-section view of the field distribution $ E_y $ for the quasi-MIM structure from 3-D FDTD simulation. ....	47
Figure 2.6	Fabrication steps flow chart. The left panel shows the side view and the right panel shows the cross-section view in the light propagating direction inside the slot waveguide. ....	48
Figure 2.7	(a) Device top-view with quasi-MIM region sketched (top inset) and shown by SEM picture (bottom inset). (b) Device top-view for scattering of near-infrared light from a silicon slot when power is coupled from an SM silicon waveguide on the right-hand side. (c) Light scattered from a dielectric slot with 500-nm quasi-MIM. The weakened scattering compared to (a) denotes the loss introduced by the quasi-MIM region. ....	52
Figure 2.8	The spectrum response between 1460 nm and 1620 nm of two quasi-MIM designs. The averaged power is approximately $1.7 \mu\text{W}$ for 500-nm case and $0.6 \mu\text{W}$ for 2- $\mu\text{m}$ case for this frequency range. ....	53
Figure 3.1	Illustration of the coupler and nanotaper. ....	58
Figure 3.2	The 3-monitors setup to calculate the transmission, reflection and loss of the system. ....	60
Figure 3.3	Simulation of light coupling from a dielectric waveguide into the MIM plasmonic taper: (a) the $S_x$ distribution in the horizontal plane; (b) the $S_x$ in the vertical plane. ....	63
Figure 3.4	The x-component of power flow ( $P_x$ ) along the x-axis. ....	63

Figure 3.5	The spot size at different locations along the x-axis. ....	64
Figure 3.6	(a) The distribution of electric field amplitude $ E(r) $ at the plane $z=0$ . (b) The electric field amplitude $ E(r) $ at the central axis ( $y=0; z=0$ ) along the propagation direction. ....	65
Figure 3.7	(a) The effective index and loss for the 20 nm thick MIM plasmonic waveguide with different widths. (b) The overall efficiency for tapers with different lengths. ....	67
Figure 3.8	(a) 3-D and (b) top view of the integrated plasmonic mode transformer with a nano-tip extended from the taper end. ....	69
Figure 3.9	Schematic view of (a) the 2-D side-view and (b) the 3-D-view of a nano-taper pair connected with silicon strip waveguides. ....	69
Figure 3.10	E-Field intensity at different locations along the propagation direction inside (top left) or out of the tip. The colorbar is normalized to the maximum E-field found in the 3-D simulation region. ....	70
Figure 3.11	Contour plot to show the FWHM profile ( $E$ -Intensity) at 10 nm away from the tip. ....	71
Figure 4.1	The sketch of an integrated mode transformer including paired tapers and a 3-D nanoplasmonic waveguide as “bridge”. ....	74
Figure 4.2	H-Intensity showing the coupling process between silicon waveguides to (a) a gold nanowire taper-pair and (b) MIM plasmonic waveguide taper-pair. Efficient direct coupling can be seen in (b). ....	76

Figure 4.3	FDTD simulation results ( $H$ -field) for light propagation in (a) taper-assisted mode transformer and (b) multimode MIM waveguides. Insets show the cross-section view of $H$ intensity. ....	77
Figure 4.4	E Intensity for the direct coupling interface consisting of (a) no air gap and (b) 50 nm air gap. ....	78
Figure 4.5	Fabrication steps combining two-stepped electron beam lithography and lift-off. ....	79
Figure 4.6	SEM and AFM images of (a) multimode plasmonic coupler and (b) taper-assisted mode transformer. (c) near-infrared light coupled in and out of the plasmonic mode transformer (rotated 90° clockwise along screen normal direction with respect to (b)). ....	83
Figure 4.7	(a) The measured transmission spectrum for a taper-assisted coupler (blue), the taperless/multimode coupler (red) and an air gap with no plasmonic component (green). (b) Theoretical (red) and experimental (blue) results of propagation loss for the single mode plasmonic waveguide in bridge area. ·	84
Figure 5.1	Schematic view of the spoof plasmonic waveguide for THz region. (a) 3-D scheme of the waveguide for THz region. (b) The physical dimension of each metal post for THz region. ....	89
Figure 5.2	Dispersion relation for the identical metal unit in air (red, dotted) and in silicon (green, square). ....	91
Figure 5.3	An illustration of the setup for the FDTD simulations used for $Q$ calculation. The arrows denote the sources and crosses denote the detectors. ....	92

Figure 5.4 Dispersion diagram of Designer Surface Plasmon waveguide in GHz spectrum. Adopted from [66].	93
Figure 5.5 Field or power of different views at 0.6 THz and 30 THz. Cross-section view of electric field intensity $ E ^2$ at (a) air space between two metal posts and (b) a metal post, both at 0.6 THz. (c) Side view of power density $\text{real}(P_x)$ in the symmetry plane and (d) top view of power density $\text{real}(P_x)$ at $0.01 \mu\text{m}$ above the top surface of metal posts, both at 30 THz.	94
Figure 5.6 Proposed fabrication steps. (a) Conventional metallization. (b) Sputtering onto sidewalls only.	96
Figure 6.1 E-field Intensity of a bounded super surface wave hosted by the multilayered metal-dielectric composite at a wavelength of 630 nm.	100
Figure 6.2 The Kretschman setup used for the excitation of super surface waves on the boundary between MMI and a top coat.	101
Figure 6.3 (a) The multilayer metal-insulator (MMI) scheme and definitions of parameters; (b) The $q$ vs. $p$ curve used to analyze different conditions for tuning effective surface plasmon frequency with a semi-space dielectrics $\epsilon_d$ .	102
Figure 6.4 (a) The analytical dispersion curves calculated by effective medium theory. The upper cut-off frequencies are treated as the effective surface plasmon frequencies (ESPFs) for two MMI cases. Near 633 nm, the shift of wave vectors are shown in the inset for uniform gold (blue), gold- $\text{Al}_2\text{O}_3$ MMI (green) and gold- $\text{SiO}_2$ MMI (red); (b) FDTD simulation for the shift of surface plasmon resonance (SPR) angles based on uniform gold (blue), gold-	

	Al <sub>2</sub> O <sub>3</sub> MMI (green) and gold-SiO <sub>2</sub> MMI (red). All three curves are on top of the same $\varepsilon = 2.5$ substrate. The small arrows mark the calculated angles based on mode matching. ....	107
Figure 6.5	Transfer matrix problem with an unmatched top coat (noted by the different values between $n_{out}$ and $n_2$ ). ....	109
Figure 6.6	Example for one pair of metal-dielectric unit in a cascaded transfer matrix system. Two boundaries and two “free propagations” are labeled for their respective transfer matrix. ....	109
Figure 6.7	TMM calculations for the structures calculated by FDTD shown in Figure 7.4. Note that the curve plotted by solid blue line is a multilayer case compared to the single layer case shown in Figure 7.4. ....	111
Figure 6.8	Experimental setup for studying multilayer metal-insulator stacks and the cross-sectional view of the fabricated multilayer sample (SEM). Each individual layer is 10 nm and there are 10 layers (5 pairs) in total. ....	112
Figure 6.9	Numerical and experimental results of reflection vs. effective index for (a) increased ESPF with SiO <sub>2</sub> substrate and (b) decreased ESPF with Si <sub>3</sub> N <sub>4</sub> substrate. Red and blue lines describe the simulation results for single-layer and multilayer respectively. Red crosses and blue triangles denote the measured results. ....	113
Figure 6.10	Substrate scan and curve change for 50nm gold only ....	116

Figure 6.11 Reflection curves changed with different SiO <sub>2</sub> substrate's refractive index. In general, a larger refractive index of substrate will shift the SPR angle to a larger value.....	117
Figure 6.12 Comparison of fitting different gap widths for (a) Si <sub>3</sub> N <sub>4</sub> and (b) gold and alumina multilayer on Si <sub>3</sub> N <sub>4</sub> .....	118
Figure 6.13 Comparison of fitting different gap widths for (a) gold on SiO <sub>2</sub> and (b) gold and alumina multilayer on SiO <sub>2</sub> . ....	119
Figure 6.14 Fitting curves for the two samples on SiO <sub>2</sub> substrate. Fitting parameter here is $n = 1.43$ for the substrate, gap width = 85 nm for gold only and gap width = 70 nm for gold-alumina multilayer.....	120
Figure 6.15 $H$ -field distribution for: (a) No bounded surface modes above surface plasmon frequency; (b) Bounded surface wave beyond conventional cutoff frequency defined in (a); (c) Bounded surface wave propagated on a single metal-insulator interface; (d) Bounded surface wave on a MMI-insulator boundary with shorter wavelength and manageable mode size compared to (c).....	123
Figure 7.1 Plasmonics for faster operation and smaller dimension. Adopted from [182].	125
Figure 7.2 Comparison of transverse E-field profiles with or without external voltage ( $\mu_c = 0$ ) for two graphene-based designs. Adopted from Figure 2 in [195]. ....	130
Figure 7.3 One possible design with doped polysilicon as the supporting layer. The substrate silicon is not shown in this figure. Silicon nitride layer is deposited	

between silicon dioxide and polysilicon to make the supporting layer more tensile. ....	130
Figure 7.4 SEM images of half through holes (with 200 $\mu\text{m}$ silicon left, left) and through holes into 500 $\mu\text{m}$ silicon substrate (right) after etched by Oerlikon. ....	131
Figure 7.5 Equivalent circuit to evaluate the cutoff frequency of an MIM tunneling diode. Adopted from [198]. ....	133
Figure 7.6 Top-view of possible diode formation in (a) side coupled and (b) point fed.	134
Figure 7.7 Physical structure of typical plasmonic scattering sources. (a) Plain silver, (b) bar element extended normal to electric field, (c) bar element parallel to electric field, (d) cross element and (e) ring element. The golden arrows show the polarization of electric field, while the blue body presents silicon. The structure is upside-down to show the shapes clearly. The silver substrate is therefore omitted in these sketches. A sketch with metal included is shown in Figure 8.13. ....	137
Figure 7.8 Absorption profiles of topview (1/4 of the total area) at 50 nm above the boundary between silicon and silver for (a) plain silver, (b) bar element extended normal to the electric field, (c) bar element parallel to the electric field, (d) cross element and (e) ring element. ....	139
Figure 7.9 Absorption profiles of side view at $y=0$ (half of the total area) for (a) plain silver, (b) bar element extended normal to the electric field, (c) bar element parallel to the electric field, (d) cross element and (e) ring element. ....	140

Figure 7.10 Absorption profiles of side view at  $x=0$  for (a) plain silver, (b) bar element extended normal to the electric field, (c) bar element parallel to the electric field, (d) cross element and (e) ring element. .... 141

Figure 7.11 Normalized enhancement ratio of 4 different scattering methods. Note that the ‘Bar1’ curve is related to the structure of Figure 8.7 (b), while the ‘Bar2’ curve to Figure 8.7 (c). .... 142

Figure 7.12 Two schemes to lay out the scattering sources. (a) “Cross” elements in a crystal-like array; (b) “Cross” elements in random. .... 143

Figure 7.13 (a) Amorphous silicon deposition on glass, (b) Silicon patterning, (c) Metal evaporation on top of silicon. Sunlight input from glass (front) side. The upside-down looking is for illustration purpose only. .... 144

## LIST OF TABLES

Table 1.1	Plasmonic frequency and damping factor of Al, Au, Cu and Ag for NIR spectrum [33].	9
Table 1.2	The lengths of evanescent tails at different wavelengths.	15
Table 1.3	TM-mode size comparison for dielectric and plasmonic waveguides with $\lambda = 1550$ nm light. Data acquired from FDTD Solutions's integrated mode solver ( <a href="http://www.lumerical.com">www.lumerical.com</a> ).	20

## LIST OF ACRONYMS

AFM.....	Atomic Force Microscopy
ALD .....	Atomic Layer Deposition
ATIR .....	Attenuated Total Internal Reflection
CVD .....	Chemical Vapor Deposition
DLSPP.....	Dielectric-Loaded Surface Plasmon Polariton
DUV .....	Deep Ultraviolet
EBL.....	Electron Beam Lithography
EMT .....	Effective Medium Theory
ESPF .....	Effective Surface Plasmon Frequency
FDTD .....	Finite-Difference Time-Domain
FEM .....	Finite Element Method
FTTH.....	Fiber-To-The-Home
HAMR.....	Heat-Assisted Magnetic Recording
ICP .....	Inductively Coupled Plasma
IMI .....	Insulator-Metal-Insulator
IPE.....	Internal Photoemission
MI.....	Metal-Insulator
MIM.....	Metal-Insulator-Metal
MoM .....	Method of Moment
NIR.....	Near-Infrared

NSOM.....	Near-Field Optical Microscopy
PEC .....	Perfect Electric Conductor
PECVD .....	Plasma-Enhanced Chemical Vapor Deposition
PV .....	Photovoltaics
SPP.....	Surface Plasmon Polariton
SP .....	Surface Plasmon
SPF.....	Surface Plasmon Frequency
SPR .....	Surface Plasmon Resonance
TMM.....	Transfer-Matrix Method
UV.....	Ultraviolet
VLSI.....	Very Large Scale Integration

---

# 1 INTRODUCTION

---

On-chip optical interconnect has long been recognized by International Technology Roadmap for Semiconductors (ITRS) as one of the most promising solutions as transistor densities continue to grow exponentially and copper interconnects fail to keep up [1]-[4]. Integrated silicon photonics has been explored intensively in the past few years, and flourishing results and numerous breakthroughs are generated as a result [5]-[15]. Surface plasmon-based photonics (or plasmonics) merge electronics and photonics at the nanoscale, creating the ability to combine the superior technical advantages of photonics and electronics on the same chip. Plasmonics focuses on the innovation of photonic devices by exploiting the optical property of metals. In particular, the oscillation of free electrons, when properly driven by electromagnetic waves, would form plasmon-polaritons in the vicinity of a metal surface and potentially result in extreme light confinement, which may beat the diffraction limit faced by conventional photonic devices and enable greatly enhanced light-matter interactions at the deep subwavelength length scale.

The history of surface plasmon research could date back to the investigation of surface plasmon resonance (SPR) on metallic thin films [16], and light scattering from nanoscale metallic particles as early as late 1969s [17]. Since the 1990s, plasmonics has enjoyed exponential progress of development. Recent research focus has shifted to the integration of plasmonic components into photonic sub-systems for optical communications and information exchange, and many novel plasmonic devices have been developed for communications in recent years [18]. As the key components of a

communication system, the plasmonic counterparts of lasers [19], waveguides [20], couplers [21], detectors [22], and modulators [23], have become the core topics of the new plasmonics era. Recent years have seen significant progress on the development of these components and rapid transition and combination of plasmonic and photonic techniques [18] [24]. Two factors have contributed and catalyzed the transition. Firstly, the advanced numerical tools backed by powerful computers have become more affordable and accessible. Secondly, with the fast development of nano- and micro-fabrication technology, researchers have been empowered to fabricate complex structures and manipulate a wide selection of materials. With both numerical and experimental approaches in mind, this dissertation will focus on the design and demonstration of plasmonic components in optical integrated circuits (OICs), as well as establishment of versatile platforms for subwavelength surface plasmons.

## **1.1 Motivation**

Light has emerged as one of the most important carriers for large volumes of data, as well as a reliable and powerful aide for the perception and manipulation of small particles. Compared to its classical form featuring diffraction-limited beams in bulky dielectric devices, in recent years the science of optics has utilized much finer elements where the light-matter interactions are strengthened inside a much smaller length scale compared to the lightwave's wavelength. Micro-optics and nanophotonics, despite the miniature size of their elements of interest, have shown a remarkable impact on all kinds of applications in communications, storage, sensing, and imaging, etc [5]-[15]. However, the mode size of a dielectric waveguide is still restricted by the diffraction-limit in the order of  $\lambda_0/2n$ , with  $n$  being the guiding area's refractive index and  $\lambda_0$  being the vacuum

wavelength of the incident wave. As a result, further shrinking the dimension of dielectric waveguides will inevitably lead to “cutoff” exemplified by poorly confined optical power.

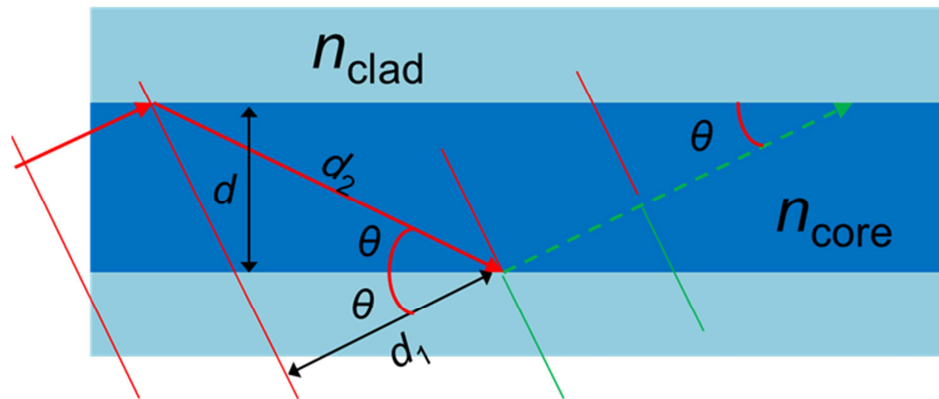


**Figure 1.1** The self-consistency condition for a dielectric waveguide. Original wave (red, solid) and its twice-reflected offspring (green, dashed) needs to be in phase to create an optical mode (adapted from Figure 8.1-2 of [20])

In a dielectric waveguide, the “cutoff” can be understood intuitively by thinking of confined modes as the interference between an “original” plane wave and another plane wave formed consequently by this incident wave reflected twice from the core-cladding interface [25] (Figure 1.1). For simplicity, we consider here a 2-D dielectric guiding core sandwiched by dielectric cladding layers. A conventional dielectric waveguides have a high-index core and low-index claddings to guarantee the total internal reflection when the “original” wave impinges into the core-cladding interface (shown by the arrows in Figure 1.1). Since an optical mode requires the same power distribution along the propagation direction, the “original” wave must oscillate in phase with the twice-reflected wave and form an interference pattern. Because of the different

traveling length ( $d_1$  and  $d_2$ ) due to the reflection (twice) of the second wave, there is a phase difference between these two:

$$\Delta\phi = \frac{d_2 - d_1}{\lambda} \cdot 2\pi = \frac{d / \sin\theta - d / \sin\theta \cdot \cos 2\theta}{\lambda} \cdot 2\pi = \frac{4\pi d \sin\theta}{\lambda}, \quad (1.1)$$

when  $d$  is the core thickness,  $\theta$  is the angle between the original wave and the boundary (incident angle), and  $\lambda$  is the wavelength of the original (as well as the reflected) wave. This phase shift must be an integer multiple of  $2\pi$  for a constructive interference, which leads to a relation between incident angle  $\theta$  and the thickness  $d$  as

$$\sin\theta_m = m \frac{\lambda}{2d}, m = 1, 2, \dots \quad (1.2)$$

Apparently, there is a minimum for the incident angle  $\theta$  at  $m=1$ . Note that when  $d$  keeps shrinking, the right side of Eq. (1.2) will be getting bigger. At a point of  $d = \lambda/2$ , the right side will grow to be larger than 1 and there will not be any valid  $\theta$  at all. Strictly speaking, the left side of Eq. (1.2) is also limited by the total internal reflection condition and hence needs to be smaller than the value of  $\sqrt{1 - (n_{\text{clad}} / n_{\text{core}})^2}$ . If we try to relate the wavelength  $\lambda$  to the vacuum wavelength  $\lambda_0$  by assuming an effective index  $n_{\text{eff}}$  which satisfies the condition  $n_{\text{clad}} < n_{\text{eff}} < n_{\text{core}}$ , we could obtain an estimation of the value  $d$  based on Eq. (1.2) as

$$d > \frac{1}{\sqrt{1 - (n_{\text{clad}} / n_{\text{core}})^2}} \cdot \frac{\lambda}{2} = \frac{n_{\text{core}}}{\sqrt{n_{\text{core}}^2 - n_{\text{clad}}^2}} \cdot \frac{\lambda_0}{2n_{\text{eff}}} > \frac{n_{\text{core}}}{n_{\text{core}}} \cdot \frac{\lambda_0}{2n_{\text{core}}} = \frac{\lambda_0}{2n_{\text{core}}}. \quad (1.3)$$

Herein it is clear that there is a ‘‘cutoff’’ condition for a conventional dielectric waveguide to ensure the guiding region is dimensionally wide enough compared to the operation wavelength. This relation is similar to the Abbe diffraction limit [26] in diffraction-

limited imaging system, and will make it difficult to build deep-subwavelength scale optical waveguides. To overcome this limitation, there have been significant efforts focusing on the exploration of novel guiding mechanisms and materials [27]-[29]. Waveguides based on surface plasmons by *metals*, as will be discussed later, can support propagation mode tightly bounded to the metallic surfaces and possibly confine the guided wave in the deep subwavelength scale. Accordingly, plasmonics has received tremendous attention for its potential to overcome the diffraction-limit of conventional dielectric optical components.

The current trend of technology evolution is marked by the demand of ultra-small devices and high-volume integration of multiple modules on the same chip. As Moore's law in Microelectronics enforces more computational power in unit area, the telecommunication has harbored the fiber-to-the-home (FTTH) conception [30] which put high emphasis on reducing the size and cost of individual optical modules. This poses significant challenges for installation of next-generation optical interconnects featured both compact integration and faster operation, which can be addressed possibly by resorting to plasmonics.

Moreover, light has been anticipated as an indispensable tool to print or define ultra-fine patterns and to manipulate and observe miniscule items. For instance, optical lithography has been pivotal for the prosperity of semiconductor technology [31], but its ability to follow the roadmap of very-large-scale-integration (VLSI) technology has been slowed down because of the diffraction-limit of most optical imaging systems. As another example, with complex systems such as DNA sequencing facility [32] designed and developed to incorporate ultra-fine optical sub-systems, the cost and quality of

optical consumables interfacing with small amount of biological or chemical substances have proved to be decisive. It has also been predicted that plasmonic nanofocusing can revolutionize the traditional magnetic recording by optically heat the media stack in a highly confined fashion, according to the technology named Heat Assisted Magnetic Recording (HAMR) or Thermal Assisted Magnetic Recording (TAMR) [33]. Plasmonics, in this sense, shall play a much larger role for optical subsystem development.

## 1.2 Nanoplasmonic Waveguide

Research in plasmonics or other surface plasmon related topics has progressed greatly, spurred by significant breakthroughs reported at the end of last century (Figure 1.2) [34]. The study of localized surface plasmon remains active, which still finds applications ranging from sensing, detecting, lithography, imaging, to data storage [18] [24]. Since 1990, the study of plasmonic waveguides and plasmon-enhanced (extraordinary) transmission [35] has greatly boosted the exposure of the subject. In this section, the fundamentals of plasmonics and the theory of plasmonic waveguides will be reviewed in detail.

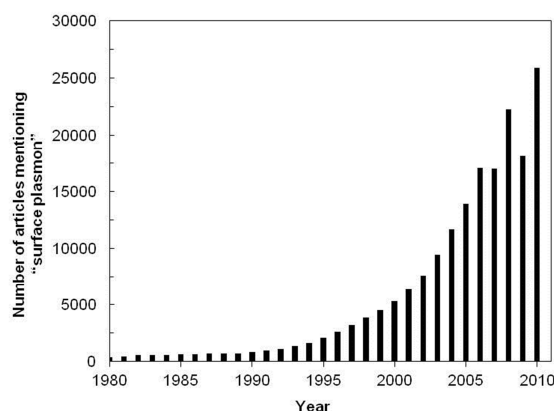


**Figure 1.2** The growth of SP-related research in number of articles from 1980 to 2010, data acquired from Google Scholar (<http://scholar.google.com>, accessed on Feb 10, 2012).

### 1.2.1 Metal Optics with Drude Model

Metallic films are typically regarded as reflectors or cladding layers in guided-wave micro-optics for the visible and near-infrared (NIR) electromagnetic spectrum regimes. While metals' role in optics seems limited, the history of plasma optics is surprisingly long, although it in general lacks detailed descriptions from a guided-wave perspective. Plasma optics assumes the rationality of effective dielectric constant of conduction electrons or electron gas, which determines the behavior of plasma oscillations in response to external optical driving field [36]. A plasmon is a quantized plasma oscillation, and the motion of the collective oscillation can rightly support electromagnetic (EM) waves at optical frequencies. For bounded charges in dielectric medium, a classical harmonic oscillator equation can be used to describe its motion as

$$\frac{d^2x}{dt^2} + \sigma \frac{dx}{dt} + \omega_0^2 x = \frac{F}{m}. \quad (1.4)$$

The Lorentz equation of motion can be used to derive the effective susceptibility [37]. In this equation,  $F$  is the applied force,  $x$  is the displacement,  $m$  is the mass of the charge,  $\omega_0 = \sqrt{\kappa/m}$  is the resonance angular frequency for which  $\kappa$  is the elastic constant of the restoring force, and  $\sigma$  is the damping coefficient. Note that for electron gas, the restoring force and the damping factor in the Lorentz equation (1.4) is omitted, which leads to  $\kappa = \omega_0 = 0$  and  $\sigma = 0$ . Equation (1.4) can be therefore simplified to

$$m \frac{d^2x}{dt^2} = -eE, \quad (1.5)$$

where  $e$  is the unit electric charge and  $E$  is the electric field. The permittivity  $\varepsilon$  and susceptibility  $\chi$  can be linked with the motion equation based on the dipole momentum  $p$  defined as

$$p = -ex. \quad (1.6)$$

Combining Eqs. (1.5) and (1.6) and recall the definition of permittivity and susceptibility, we have

$$\varepsilon = 1 + \chi = \frac{Np}{\varepsilon_0 E} = 1 - \frac{Ne^2 / \varepsilon_0 m}{\omega^2} = 1 - \frac{\omega_p^2}{\omega^2}. \quad (1.7)$$

This will provide the frequency independent plasma frequency  $\omega_p = \sqrt{\frac{Ne^2}{\varepsilon_0 m}}$ , while  $N$  describes the electron concentration,  $e$  the unit electric charge,  $\varepsilon_0$  the free space permittivity, and  $m$  the electron mass.

On the other hand, the Drude model assumes a frequency dependent conductivity  $\sigma = \sigma_0 / (1 + j\omega\tau)$ , where  $\sigma_0$  is the low frequency conductivity and  $\tau$  is the relaxation time. If volume plasma can be described by a characteristic plasma frequency  $\omega_p = \sqrt{\sigma_0 / \varepsilon_0 \tau}$ , Drude model can be used to determine the dielectric constant of metals ( $\varepsilon_0$  being the free space permittivity) and this well matches with the conclusion of Eq. (1.7):

$$\varepsilon_e(\omega) = \varepsilon + \frac{\sigma}{j\omega} = \varepsilon_0 + \frac{\sigma_0}{j\omega(1 + j\omega\tau)} \approx \varepsilon_0 - \frac{\sigma_0}{\omega^2 \tau} = \varepsilon_0 \left(1 - \frac{\omega_p^2}{\omega^2}\right). \quad (1.8)$$

In this dissertation, we mostly consider gold and silver for applications in the NIR and visible light spectra. The plasma frequencies for these materials are well above 1000 THz, and are in general higher than the frequency of the incident beam. The plasma

frequencies given by  $f_p = \omega_p / 2\pi$ , and the damping factors by  $\gamma_\tau = 1 / \tau$ , for the NIR spectrum of aluminium, gold, copper, and silver are shown in Table 1.1, adapted from [38]. The dielectric constants of these four metals are plotted in Figure 1.3 [39].

Material	$f_p$ (THz)	$\gamma_\tau$ (rad/s)
Aluminium	3570	124.34
Gold	2183	40.59
Copper	1914	52.40
Silver	2180	27.35

**Table 1.1 Plasmonic frequency and damping factor of Al, Au, Cu and Ag for NIR spectrum [38].**

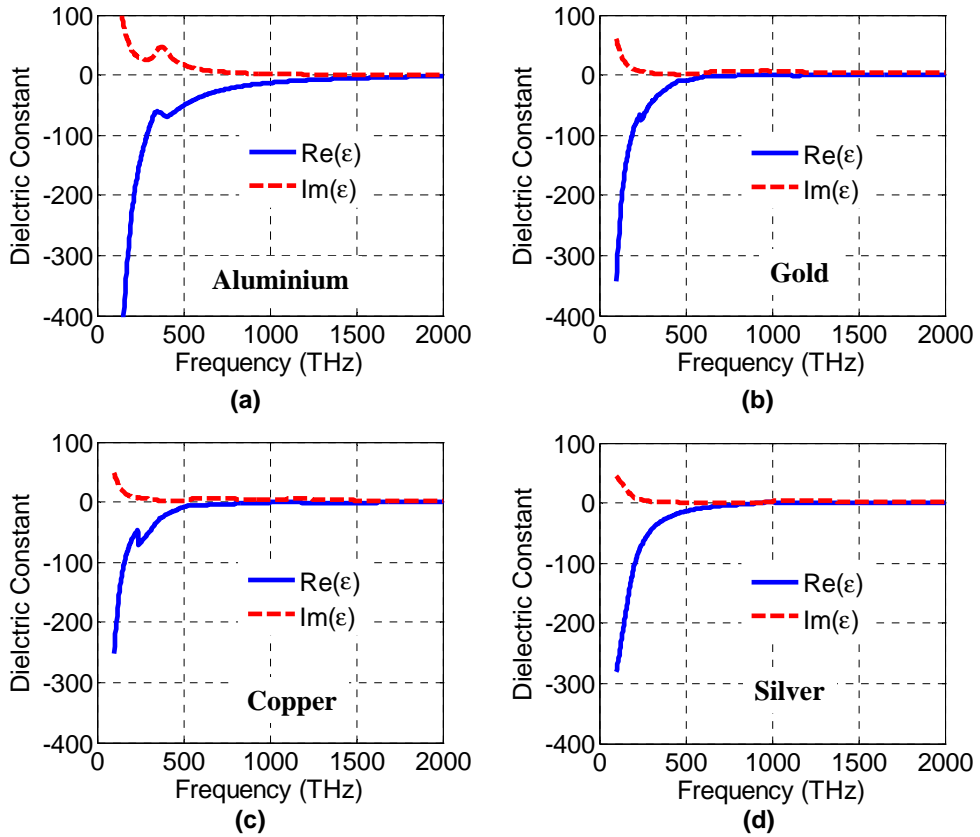


**Figure 1.3 Dielectric constants of (a) Aluminium, (b) Gold, (c) Copper and (d) Silver [39].**

By comparing the plasma frequency with the damping factor and considering the optical application regime, we conclude external driven field from light will in general meet the prerequisite of  $\omega \gg 1/\tau$  for the Drude model and the effective permittivity formalism cited above to hold. Therefore, EM waves inside a metal using the effective permittivity formalism (no additional free current or conductivity term) can be characterized by the classical Helmholtz equation derived from Maxwell's equation

$$(\nabla^2 + \epsilon_e k_0^2) \vec{E} = 0. \quad (1.9)$$

Note that in the Ampere's law used to derive this equation, there is no free current term. The factor of conductivity can be absorbed into the effective permittivity as below, although the following analysis will generally omit the damping factor  $\gamma_\tau$ , assuming the form defined in Equation (1.8). Therefore

$$\nabla \times \vec{H} = j\omega \epsilon_e \vec{E} \approx j\omega \text{Re}[\epsilon_e] \vec{E}. \quad (1.10)$$

### 1.2.2 Bulk Plasma and Surface Plasma

Considering a plane wave solution in the form of  $A \exp(-j\vec{k} \cdot \vec{r})$  for Equation (1.9), a dispersion relation can be obtained as

$$|k|^2 = k_0^2 \epsilon_e(\omega) = (\omega/c_0)^2 \epsilon_e(\omega). \quad (1.11)$$

Equation (1.11) clearly shows that a metal with positive permittivity will support plane waves in the bulk medium. In other words, if the working frequency goes above the bulk plasma frequency, the plasma (or metal) becomes transparent to this external EM wave as

$$\beta \equiv \text{Re}(k) = \sqrt{\epsilon_e} k_0 = k_0 \sqrt{1 - \frac{\omega_p^2}{\omega^2}}. \quad (1.12)$$

This dispersion relation of a free electron gas is shown as the solid blue curve in Figure 1.4.

On the other hand, a negative dielectric constant is obtained when the working frequency of the incident optical beam falls below the plasma frequency, which leads to an evanescent wave with an imaginary wave vector, as given by

$$k_{eva} = \sqrt{\epsilon_e} k_0 = \pm j k_0 \sqrt{\frac{\omega_p^2}{\omega^2} - 1}. \quad (1.13)$$

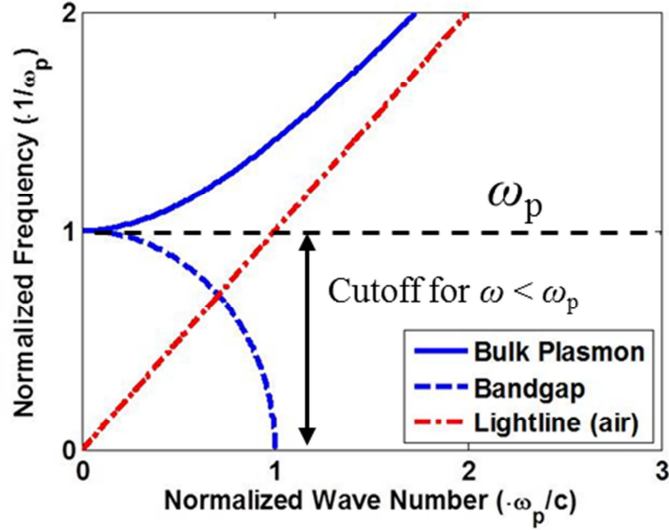


**Figure 1.4** Dispersion relation of free electron gas (solid) compared to that of lightline of dielectric material (dashed).

This relation is shown as a lower frequency cutoff related to plasma frequency  $\omega_p$  in Figure 1.4. Physically, whatever direction the incident field comes from, the field will impinge into a small thickness known as skin depth, and then be fully shielded by the free electrons. The concept and the term of ‘skin-depth’ conveys an implication that only a small fraction of bulk metal could take part in the photon-material interaction, and very

limited field-penetration or power-propagation could ever happen. External optical fields can only penetrate into metals for a range of a couple of nanometers among this spectrum, and are therefore trivial compared to the reflecting power radiated away from the metal surfaces.

Negative permittivity does not usually lead to ‘cutoff’ of optical interactions. It actually has great potentials to be utilized in multiple applications, as researchers have already done to artificially shaped structures such as photonic crystals [40] or metamaterials [41]. When a metal-insulator boundary is considered, the negative permittivity of the metal is pivotal for the propagation of surface plasmons.

For surface plasmons, the dispersion is more complicated. Surface plasmon waves, which reveal the macroscopic motion of surface plasmon-polaritons (SPPs), are a coherent combination of electron gas oscillation (plasmons) and photons. For a simple case of a single metal-insulator interface in 2-dimensional (2-D) view, a transverse-magnetic (TM) solution for Equation (1.9) is available [16], [42]. As shown in Figure 1.5 by the red solid lines, the surface plasmon wave propagates in the form of  $H_{z,d,m} = H_0 \exp(-j\beta x) \exp(-\gamma_{d,m} y)$ . A matched real propagation constant ( $\beta$ ) is required for a maintained wave-motion in both materials ( $\epsilon_m$  for metal and  $\epsilon_d$  for insulator). Applying the boundary conditions for  $H_z$  and  $E_x$ , a relation of  $\gamma_d / \epsilon_d = \gamma_m / \epsilon_m$  can be obtained. Based on this relation as well as the definition of  $\gamma_{d,m}$  shown in Figure 1.5, the dispersion relation for SPPs at a single interface can be simplified as

$$\beta = \omega / c_0 \sqrt{\frac{\epsilon_m \epsilon_d}{\epsilon_m + \epsilon_d}} \quad (1.14)$$

Examining the propagation constant ( $\beta$ ), it is feasible to define the skin depths  $\delta$  as  $\delta = 1/2\gamma$  (Figure 1.5).

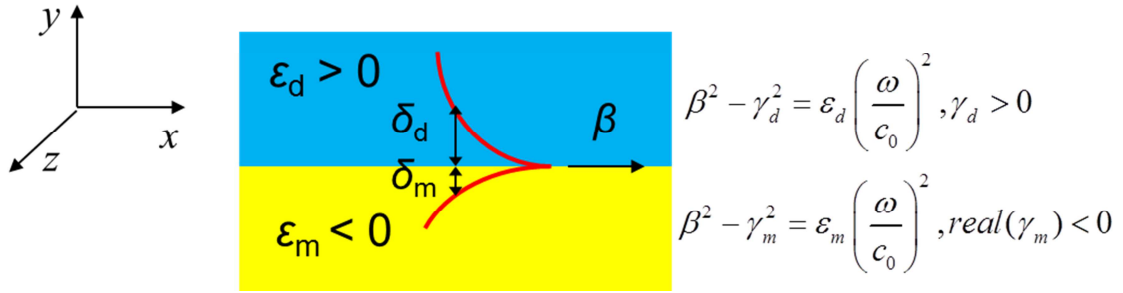


**Figure 1.5** Definition of skin depths and their relation with propagation constant. The red curve sketches the magnetic field distribution.

With a new term of surface plasmon frequency ( $\omega_{sp} = \omega_p / \sqrt{1 + \epsilon_d}$ ) being defined,

Eq. (1.14) leads to a dispersion plot for SPPs.

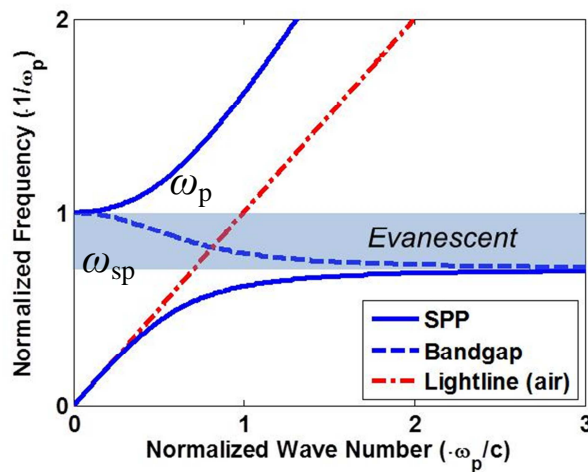


**Figure 1.6** Dispersion relation of SPP (solid) in metal-insulator configuration. The curve for the frequency between 0.707 and 1 denotes imaginary propagation constant.

In Figure 1.6, there is a gap between  $\omega_{sp}$  and  $\omega_p$ , where the curve only gives imaginary propagation constant (evanescent waves). When  $\omega < \omega_{sp}$ , SPP modes in TM

polarization exist. A very large  $\beta$  value can be obtained at  $\omega_{sp}$ , which denotes a point of resonance at that frequency point, namely the SP resonant oscillation. When  $\omega > \omega_p$ ,  $\epsilon_m > 0$ ; so metal will exhibit dielectric behaviors with radiation unbounded to insulator since the mode lies above the lightline. The dispersion relation plotted above does not take damping factor into account, which will instead force a finite wave vector  $\text{Re}[\beta]$  at  $\omega_{sp}$  due to the damping of free electron oscillations. In this case, the right-hand side of Eq. (1.14) becomes a complex value and the dispersion will also slightly differ from the case of ideal conductors [42].

The single interface case introduced above suggests several important characteristics related to SPPs. Firstly, a sustained surface wave can be excited along metal surfaces accompanied by ohmic loss, although at the same frequency bulk metal remains “opaque” for EM waves. Secondly, a bounded solution exists even with a half-space metal-cladded insulator, which means the SPP mode is confined to a single interface of metal-insulator with small out-of-plane radiation. Thirdly, the propagation constant of a SPP mode is larger than that of the lightline at the same frequency point when the driving field has less-than- $\omega_{sp}$  frequency, which indicates a smaller effective wavelength for SPP mode compared to optical mode at same frequency. These three features are the sources of most applications reviewed in this dissertation, and are the fundamentals of many prior efforts. The subwavelength-bounded propagation of EM waves, which are characteristic in most SPP or SPP-like environments, are the foundations of all efforts made thus far.

### 1.2.3 Metal-insulator-metal (MIM) Waveguides

Although surface plasmons can be confined to the metal-insulator boundary, the mode spread of the SP waves depends on the configuration of the waveguides and also the frequency. The length of the evanescent tail in a waveguide medium can be approximated by  $\delta = 1/2\gamma$ , when  $\gamma$  is defined from the conservation of momentum:

$$\beta^2 - \gamma_d^2 = \epsilon_d \left( \frac{\omega}{c_0} \right)^2 \quad (1.15)$$

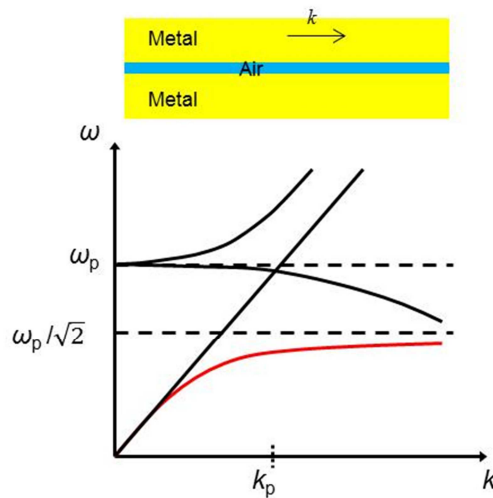
$$\beta^2 - \gamma_m^2 = \epsilon_m \left( \frac{\omega}{c_0} \right)^2. \quad (1.16)$$

Table 1.2 shows that for the metal-insulator (MI) waveguide, the evanescent tails  $1/2\gamma$  can be very long compared to wavelength. For subwavelength and deep subwavelength mode confinement, it is necessary to explore different waveguide forms. The following section will start from an important plasmonic waveguide, namely metal-insulator-metal (MIM) waveguide.

Wavelength ( $\lambda$ )	0.5 $\mu\text{m}$	1.55 $\mu\text{m}$	10.5 $\mu\text{m}$	300 $\mu\text{m}$
Frequency ( $c_0 / \lambda$ )	600 THz	193 THz	28 THz	1 THz
$\epsilon_{\text{Al}}$	-36.5 + j9.4	-252 + j46	-8e3 + j5.2e3	-6e4 + j9e4
$\epsilon_{\text{Air}}$	1.0	1.0	1.0	1.0
Decay Factor ( $\gamma / k_0$ )	0.1678	0.0631	0.0112	0.0041
Tail Length ( $\delta$ )	0.23 $\mu\text{m}$	1.95 $\mu\text{m}$	74.7 $\mu\text{m}$	5800 $\mu\text{m}$
Relative Tail Length ( $\delta / \lambda$ )	0.47	1.26	7.12	19.49

**Table 1.2** The lengths of evanescent tails at different wavelengths.

The idea to incorporate surface plasmons to guided EM waves can be traced back to Economou's paper [16] on theoretical study of EM field inside thin-film configurations. Note that it was about 30 years later, with the progress of advanced simulation tools and micro-scale fabrication technology, that people could characterize plasmonic waveguides at optical frequencies.



**Figure 1.7** Dispersion plot for MIM layered structure adapted from [16].

A simple yet important form of a plasmonic waveguide is based on a metal-insulator-metal (MIM) configuration (Figure 1.7). This waveguide, as its name indicates, consists of three layers with a dielectric core of either air or other insulator (usually with low optical loss and moderately small refractive index), sandwiched by two metal claddings. In Economou's work [16], the dispersion relation for MIM configuration is analytically expressed, and one of the calculation approaches for the transcendental equation is given in Appendix A. In recent years, detailed analytical [43], [44] and experimental studies [45] of MIM are still performed and reported.

In a 2-D case, both MIM waveguides and conventional dielectric waveguides have analytical solutions. For a TM mode in a 2-D dielectric waveguide, the fields to our interest are  $H_z$ ,  $E_y$  and  $E_x$ , when  $x$  is the propagation direction and  $y$  points across the boundary. From the coupled Maxwell equation, and assuming the real wave vector  $\beta$  is positive in  $x$  direction, we have  $E_x(y) = \frac{-j}{\omega\epsilon} \frac{\partial}{\partial y} H_z(y)$  and  $E_y(y) = \frac{\beta}{\omega\epsilon} H_z(y)$ . Solve the decoupled Maxwell equation for  $H_z$  with a positive and real  $\beta$  and apply the continuity of  $E_x$  and  $H_z$  for bounded mode, we have

$$\begin{cases} H_z(y) = H_0 \cos(\sqrt{\epsilon_1 k_0^2 - \beta^2} y), |y| < d/2 \\ H_z(y) = H_0 \cos(\sqrt{\epsilon_1 k_0^2 - \beta^2} \frac{d}{2}) * \exp(\mp \sqrt{\beta^2 - \epsilon_2 k_0^2} (y \mp \frac{d}{2})), |y| > d/2 \end{cases} \quad (1.17)$$

Here  $k_0 \equiv \omega/c$ ,  $\epsilon_1$  and  $\epsilon_2$  are the core and cladding's dielectric constants respectively,  $d$  is the core region's thickness. The power denoted by Poynting vector carried by this mode is

$$P(x) = \text{Re} \int_{-\infty}^{+\infty} \frac{1}{2} \overline{E} \times \overline{H}^* \cdot \hat{x} dy = \text{Re} \left[ \frac{1}{2} \int_{-\infty}^{+\infty} E_y(y) [H_z(y)]^* dy \right] = \frac{\beta}{2\omega} \int_{-\infty}^{+\infty} \frac{|H_z(y)|^2}{\epsilon(y)} dy \quad (1.18)$$

The common wave vector  $\beta$  can be solved from the dispersion relation and expressed as

$$\frac{\epsilon_1 \sqrt{\beta^2 - \epsilon_1 k_0^2}}{\epsilon_2 \sqrt{\epsilon_1 k_0^2 - \beta^2}} = \tan(\sqrt{\epsilon_1 k_0^2 - \beta^2} \frac{d}{2}) \quad (1.19)$$

For the lossy but bounded mode of an MIM plasmonic waveguide, a positive, real  $\beta$  is not sufficient to describe the behavior in propagating direction. The metal cladding and dielectric core will share a complex propagation constant  $k = \beta + j\alpha$ . This notation

incorporates the conduction loss and enables the complex dielectric constant for a conductor:

$$\tilde{\epsilon} = \epsilon_0 \left( \epsilon_r - j \frac{\sigma}{\omega \epsilon_0} \right) = \epsilon_0 \tilde{\epsilon}_r \quad (1.20)$$

The updated parameters mentioned above will give  $E_x(y) = \frac{-j}{\omega \tilde{\epsilon}} \frac{\partial}{\partial y} H_z(y)$  and

$E_y(y) = \frac{-jk}{\omega \tilde{\epsilon}} H_z(y)$ . The Helmholtz function for magnetic field with complex dielectric

and propagation constants will thereby have a solution in the form of

$$\overline{H} = H_z(x, y) \hat{z} = H_z(y) \exp(-kx) \hat{z} \quad (1.21)$$

in which case the real part and the imaginary part of  $k$  are both positive so as to describe the propagation with damping in positive  $x$ -axis. The simplified Helmholtz function is therefore

$$\frac{\partial^2}{\partial y^2} H_z(y) + (k^2 + \tilde{\epsilon}_r k_0^2) H_z(y) = 0 \quad (1.22)$$

If we denote  $k_{i,m}^2 \equiv -k^2 - \tilde{\epsilon}_{i,m} k_0^2$  and apply the boundary conditions for the continuity of  $E_x$  and  $H_z$ , the magnetic field for the fundamental symmetrical bounded mode can be expressed as

$$\begin{cases} H_z(y) = H_0 \cosh(k_i y), |y| < d/2 \\ H_z(y) = H_0 \cosh(k_i \frac{d}{2}) * \exp(\mp k_m (y \mp \frac{d}{2})), |y| > d/2 \end{cases} \quad (1.23)$$

where  $d$  is the thickness of the dielectric core. The power carried by MIM fundamental mode is therefore

$$P(x) = \text{Re} \int_{-\infty}^{+\infty} \frac{1}{2} \overline{E} \times \overline{H}^* \cdot \hat{x} dy = \frac{1}{2} \text{Re} \left[ \int_{-\infty}^{+\infty} \frac{-jk}{\omega \tilde{\epsilon}(y)} H_z(y) [H_z(y)]^* dy \right] \quad (1.24)$$

The dispersion equation for MIM bounded mode is therefore

$$-\frac{\tilde{\epsilon}_i \tilde{k}_m}{\tilde{\epsilon}_m \tilde{k}_i} = \tanh\left(\tilde{k}_i \frac{d}{2}\right) \quad (1.25)$$

where a complex  $k$  is the only variable of this equation considering the relation of

$$k_{i,m}^2 \equiv -k^2 - \tilde{\epsilon}_{i,m} k_0^2.$$

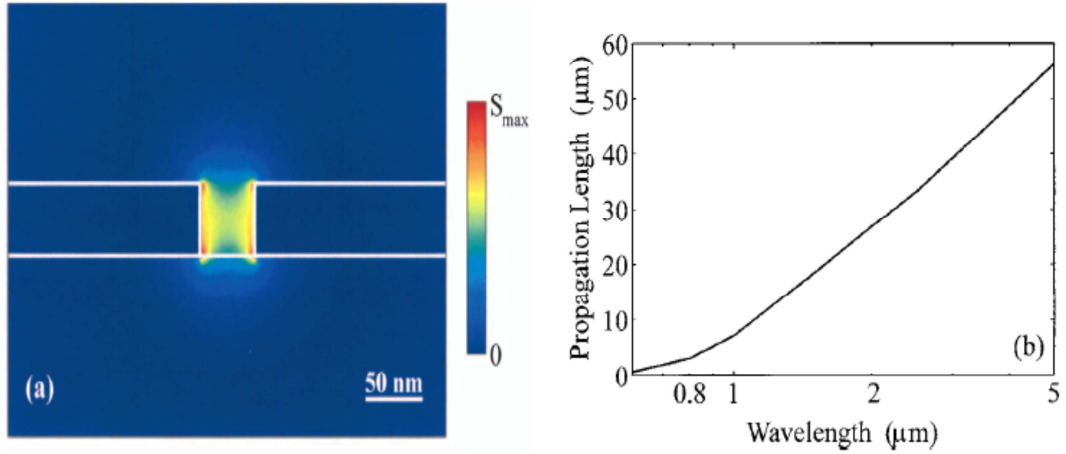


**Figure 1.8** Left: A typical MIM mode profile for 1550 nm light inside a 50nm-by-50nm air gap. The substrate and superstrate are silicon dioxide and air, respectively. Right: Propagation distance of the MIM mode for optical to NIR frequency [46].

As verified by extensive numerical analysis, MIM waveguides possess notable tradeoff between acceptable propagation loss and subwavelength mode size. Veronis, et al. [46], along with Feigenbaum, et al. [47], have performed 3-dimensional (3-D) simulations and mode analysis for MIM (sometimes called MDM for metal-dielectric-metal) structures. They have successfully shown that while the mode size of MIM can be decreased to very close to the physical dimension of the guiding core in deep

subwavelength regime, the acceptable propagation length keeps MIM waveguides competitive for on-chip signal transmission (Figure 1.8). The 2-D to 3-D transition is verified by shrinking a 2-D nano-slit [1] to a 3-D nano-spot [46]. This feature brings in the possibility of using MIM structure as a device to guide propagating waves in ultra-small dimensions (Figure 1.8), and therefore provides a feasible platform for applications that require extreme field confinement or intensified light-matter interactions. The metal sandwich could possibly contain and redirect scattering from rough surfaces, which is another advantage of the MIM configuration over the conventional MI structure.

Waveguide Type	Dielectric	MIM	IMI	MI
Materials	Silicon	Silver, air	Silver, air	Silver, air
Core Thickness	300 nm	30 nm	30 nm	-
Total Cladding Thickness	-	300 nm	300 nm	-
$n_{\text{eff}}$	2.5060	1.5788	2.7104	1.0039
Loss (dB/cm)	-	2180.5	846.5	44.0
FWHM ( $H$ intensity)	208 nm	46 nm	148 nm	983 nm

**Table 1.3** TM-mode size comparison for dielectric and plasmonic waveguides with  $\lambda = 1550$  nm light. Data acquired from FDTD Solutions's integrated mode solver ([www.lumerical.com](http://www.lumerical.com)).

From a transfer matrix perspective, it has been shown that if the fundamental TM mode is excited inside an MIM gap, the waveguide works well as a transmission line (TL) system, and shows reduced scattering loss from sharp bend [48], unlike traditional optical waveguides. The transmission line (TL) theory, adopted from the microwave realm, has then been applied to cascaded MIM systems [49] to study the reflection and transmission coefficient for complex or multi-level compositions of MIM waveguides.

The formalism of TL theory based on eigenmode expansion, is found to be successful especially in calculating the coupling efficiency between SP waves propagated through several MIMs.

Along with the MIM waveguide, the insulator-metal-insulator (IMI) configuration has also found many applications. The IMI structure is formed by burying a thin metal core in a dielectric background, and if the symmetry condition is strictly met, a TM mode close to the Gaussian profile of a dielectric waveguide mode can be supported. The dispersion relation of IMI waveguide can be derived in the same manner shown in (1.21)-(1.25), by simply switching the cladding and core materials. The magnetic field in IMI can therefore be expressed in a similar form compared to (1.23)

$$\begin{cases} H_z(y) = H_0 \cosh(k_m y), |y| < d/2 \\ H_z(y) = H_0 \cosh(k_m \frac{d}{2}) * \exp(\mp k_i (y \mp \frac{d}{2})), |y| > d/2 \end{cases} \quad (1.26)$$

The transcendental dispersion relation is defined as

$$-\frac{\tilde{\epsilon}_m \tilde{k}_i}{\epsilon_i \tilde{k}_m} = \tanh(\tilde{k}_m \frac{d}{2}). \quad (1.27)$$

Devices incorporating IMI have been demonstrated for both passive [50] and active [51] cases, and because the propagation loss in an IMI is considerably smaller than in an MIM, it is frequently used for transmitting NIR optical power in distances larger than 10  $\mu\text{m}$ . The lack of mode confinement, however, hampers its usage in the deep-subwavelength scale, as it does with MI waveguides (Table 1.3).

Several discoveries are noteworthy based on the MIM platform with emphasis on extreme power confinement. Atwater and his coworkers have contributed significantly to

this topic with their characterization of MIM plasmonic waveguides [52]. Chen [53] from Cornell University evaporated gold onto silicon ribs to form MIM waveguide, which also developed a novel way to effectively excite SP modes from photons. In the field of active plasmonics, nano-cavities formed in MIM waveguide are proposed for fast modulation [54] [55], and have exhibited great potential for development of future small-print modulators.

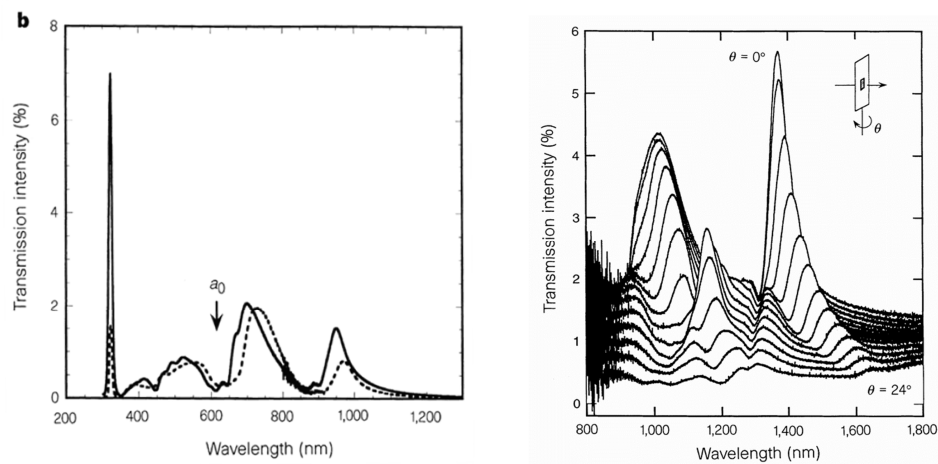


**Figure 1.9** Transmission through sub-wavelength holes patterned in Ag as a function of wavelength (left) and illumination angle (right) [35].

It is also interesting to look at the MIM waveguide from a different perspective. If an MIM waveguide is chopped for a very small propagation (less than one hundred nanometers, for example), and at the same time a light beam illuminates right into the waveguide from free space, the situation will be very close to transmission through an optical head for light-matter interactions in a highly confined scale [56], which can be used to count the power getting through a subwavelength slit or a hole inscribed on a thin film. One important literature published on extra transmission related to SP waves is from Ebbesen, et al. [35]. In this paper, the observance of at least 10 folds of transmission

enhancement is reported (Figure 1.9), after facilitated features of surface corrugations are applied. Ironically, such an important literature later was cited by the authors themselves that the reported enhancement is greatly exaggerated because of a problematic measurement. The role of plasmonics in extra transmission was therefore under debate, as Ref. [57] and especially Ref. [58] have reviewed. One of the authors from the original Nature paper [35], Tineke Thio, converted to be one of the most radical opponents to the role of surface plasmons in enhanced transmission. Diffraction theory [57], from her point of view, is powerful enough to explain most phenomena observed in extra-transmission.

Despite the debates, the eagerness of researchers to utilize SP waves to accomplish higher transmission through subwavelength holes or slits continues. For example, Pacifici, *et al.* [59] have used a near-field detector to characterize the field profile when corrugated surfaces are illuminated by plane waves. They managed to observe subwavelength focusing of light and have given their own physical model to explain it. A carefully designed mask [60] is found to be able to achieve a subwavelength transmission *beyond* near-field with radiationless interference. This discovery might be of more interest than the previous one for far-field applications such as imaging and nanolithography. More and more theoretical calculations on EM waves among periodic surface features or slit diffraction such as [61], [62] or [63] are still being elaborated and published, providing fresh approaches or understandings into this topic.

The extra transmission experiments introduced above are mostly based on incident plane waves from free space or uniform dielectric half space. In 2007, Fan and Veronis published simulation results [64] studying the propagation of NIR light butt-

connected from a dielectric waveguide to an MIM waveguide. They found that although the mode profiles between dielectric and MIM waveguides differ greatly, a transmission of ~70% can be achieved. There are quite a few previous unknowns mentioned by this theoretical analysis. Firstly, the mode overlap is not found as a key issue for coupling, as the ‘funneling’ effect has been verified by numerical simulation performed recently [65]. Secondly, the direct coupling only works for TM polarization, which is different compared to the classical case of an aperture antenna loaded on an infinite ground plane [66]. Therefore, a different physics unlike the aperture antenna theory must exist. Thirdly, the way that optical modes couple to SP modes are different from transmission line (TL) formalism. A matched propagation constant here does not necessarily guarantee an optimal coupling efficiency, as the eigenmodes in plasmonic waveguides are different in nature regarding the orthonormality compared to conventional rectangular waveguides. Further study of direct coupling is still necessary to dispel these concerns.

#### **1.2.4 Subwavelength Waveguiding by Periodic Structures**

Surface plasmons are grouped oscillations of free electrons near the surface. The coupling of plasmons and photons could happen on the boundary between a metal and an insulator. As the ‘donor’ of plasmons, metals are usually designed to share a flat boundary with insulators to avoid unwanted out-of-plane scattering. Rough boundaries or surface corrugations, on the other hand, are occasionally introduced [42] for excitations or observations of SPPs. Theoretically, surface plasmons exist for middle infrared (MIR) or even far infrared (FIR) regime. However, a flat surface fails to achieve tightly bounded surface wave beyond the NIR regime. We can recall the lengths of evanescent tails in the dielectric side are given by  $1/2\gamma_d$ , while the term  $\gamma_d$  is given by

$$\gamma_d = \sqrt{\beta^2 - \epsilon_d \left(\frac{\omega}{c}\right)^2} \quad (1.28)$$

For EM waves with frequencies much smaller than optical spectrum,  $\epsilon_m$  is a negative term with large absolute value, thus the value of  $\gamma_d$  can be very small. For a metal-insulator case with  $|\epsilon_m| \gg |\epsilon_d|$ , from the dispersion relation in Eq. (1.14), we can see  $\beta^2$  will approach  $\epsilon_d(\omega/c)^2$ , which is the right side of Eq. (1.8). Therefore,  $\gamma_d$  will likely be very small and leads to an evanescent tail up to hundreds or even thousands of wavelengths as shown in Table 1.3. This type of surface wave is more widely known as Zenneck or Sommerfeld wave [67].

On the other hand, the lower frequency (or longer wavelength) makes it possible to make comparatively small corrugation on metallic surfaces. For example, one only needs a machine shop for the fabrication of “small” structures for GHz regime, while it is extremely difficult to make 3-D metamaterials for visible light. Moreover, if the considered corrugation is small enough compared to wavelength, it can be legitimately characterized by using the effective medium formalism. This approach is called “spoof plasmonics” by Pendry, *et al.* [68], in their attempt to achieve arbitrary “spoof” plasma frequencies via drilling holes in the perfect electric conductor (PEC).

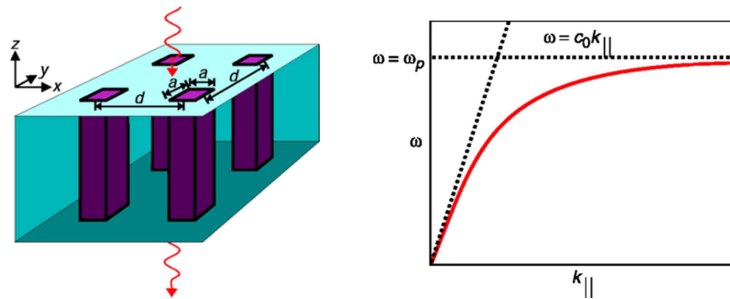


**Figure 1.10** Spoof plasmonics in PEC shown by dimension (left) and dispersion (right) [68].

When the corrugation is uniformly distributed in  $xy$  direction (Figure 1.10, left), the bulk PEC can be regarded as a uniaxial crystal, a typical anisotropic metamaterial. The dispersion calculation yields an upper cut-off frequency and extremely slow light towards this cut-off, same as the typical SPP behaves. More importantly, when an effective medium is used for analysis, the theory of conventional plasmonics can be applied to the structured surface. Therefore, the concept of surface plasmon frequency can also be extended to for this type of metamaterial. Instead of the canonical value, the new (or effective) surface plasmon frequency is determined by the dimension of surface corrugations. Therefore, the optical property of this metamaterial can be well controlled by tweaking the physical perturbations applied to the bulk material.

The spoof plasmon approach has inspired many discoveries based on surface corrugations especially in THz region as metals are almost lossless and compact THz waveguides are in high demand. Maier, *et al.* [69] have designed a THz waveguide for subwavelength confinement in 2-D working at 1 THz. Martin-Cano, *et al.* have designed metal gratings as THz waveguide platform, which can integrate multiple passive devices at the same time [70]. In GHz region, Zhao, *et al.* [71] has used designer surface plasmon approach to demonstrate the same concept.

Another platform for spoof plasmons is based on stratified medium, which finds vast applications in the optical regime. Multilayered composites with periodic layer-unit have been widely employed as negative index materials (NIMs) for super-lensing. Treated as an effective medium, its anisotropy is well approximated by straightforward mixing rules [72] if each repeated layer is thin enough compared to the working wavelength. Along with the super-lensing effect [73], multilayered composites have also

been designed to support surface-plasmon-like waves and used for nanolithography. More details of this subject can be found in Chapters 5 and 6.

### **1.3 Plasmonic Materials and Fabrication Techniques**

The progress of experimental plasmonics is closely related to the advancement of material research and fabrication technology. Plasmonic phenomena have been observed and investigated for more than 40 years, originally on light scattering from metal particles in early years, gradually including light guided by particle arrays and layered structures. Without the advanced fabrication methods to process plasmonic materials and integrate plasmonic structures into optical circuitry, it is impossible to expect the vast applications of plasmonic components in sensing, imaging, and communications to succeed in the future. In this section, the most important plasmonic materials and their processing methods will be reviewed.

In solid-state physics, surface plasmons are treated as grouped oscillation of electron gas. The electron gas model fits materials with a high-volume of free electrons, which is inherently more accurate for simple metals (alkali metals). Metals found in semiconductor technology at room temperature have an electron concentration close to the order of  $10^{22}$  per  $\text{cm}^3$ , while semiconductors or doped materials widely used in the industry have a carrier concentration of less than  $10^{17}$  per  $\text{cm}^3$ . As a result, most plasmonic structures, especially those for optical spectrum, involve metals at some level. The most-used materials in plasmonics are those that are stable at room temperature, especially aluminum (Al) and noble metals such as gold (Au), silver (Ag) and copper (Cu) (Table 1.1). Alternative plasmonic materials known to contain abundant free carriers include metallic alloys, metallic compounds, and graphene.

### 1.3.1 Metals

Metals have been studied and understood through the free electron model, in which the electrons inside metals are regarded as moving almost free from striking with each other. In the Drude formalism for 3-D electron gas, the mean relaxation time is described by the damping frequency term  $1/\gamma_\tau$  (Table 1.1). For the noble metals frequently used in plasmonics, the total damping comes from not only the interactions between conduction electrons, but also from interband transitions [36] [42]. Wherever the damping of free electron oscillation actually comes from, the propagation loss in classical electromagnetic problems for plasmonic metals can be evaluated from the imaginary parts of their dielectric constants and the electric field intensity. In any electromagnetic simulations, the loss from materials with complex dielectric constants can be treated as dissipated or lost in the form of ohmic heat. Therefore, a straightforward figure of merit for choosing plasmonic material is its resistivity. By reading the optical resistivity data or the dielectric constants of various metals [74], it is possible to spot candidates of suitable materials for different frequency ranges. In NIR spectrum, silver has the smallest imaginary part of permittivity and the best conductivity, making it a highly favored material. The easy oxidation somehow limits its applications, and makes gold a popular candidate in this frequency range. For the applications of ultraviolet (UV) or deep ultraviolet (DUV) light such as the 193 nm light for DUV optical lithography, however, aluminum is proved to be the most attractive candidate [38] (Table 1.1).

Processing metals (especially noble metals) is in general complex, especially compared with semiconductors used in micro-fabrication. The deposition of plasmonic metals can be achieved in vacuum by sputtering or evaporation. To avoid percolation,

obtain acceptable uniformity and quality, the deposition rate is usually limited to less than 1 nm per second. The small deposition rate is normally not a big issue as in most cases the required thickness for plasmonics is small. Electroplating gives faster metal growth rate but the quality of the surface might not be considered fine enough for plasmon waves.

The pattern transfer from resist to metals is extremely challenging for noble metals, as there are not many effective methods to etch copper, silver or gold. Plasmonic metals such as aluminum can be etched by a  $\text{Cl}_2$  based plasma. Other than this, there are generally two approaches to pattern metals. The first one is through image reversal and lift-off process, which requires resist overhang after development. There have been photo-resists specifically used for lift-off process such as nLOR from MicroChem® [75], while researchers also use bi-layer or multi-layer compositions to achieve the crucial overhang [76]. When using bi-layer resists for lift-off, it is conventionally required to coat a bottom resist layer for at least twice as thick as the lift-off thickness. Therefore, it is not easy to have high aspect ratio, stand-alone metal features fabricated. A second approach to pattern metal is through ion milling. A focused ion beam can be used to directly mill patterns into gold or silver films, but it usually introduces redepositions from the beam source. Argon ion beam is another option that can work with noble metals, but requires hard masks such as carbon and might greatly increase the number of steps and also the complexity of processing.

### **1.3.2 Compounds**

Metal silicides are often used to decrease the contact resistivity in VLSI circuits and especially MOSFET technology. As they have an intermediate conductivity and

carrier concentration between metal and semiconductor, silicide compounds have also been investigated for plasmonic applications especially at THz frequencies [77]. In the form of compounds consisting of silicon and metals (Ti, Co, W, Ni, Pd, etc.), silicides have a smaller plasmonic frequency compared to noble metals used in the near-infrared regime and in general higher loss. However, as its fabrication and electric property have been extensively studied for large-scale integrated circuit technology, the deposition of very thin layers and accurate patterning is highly reliable.

Transparent conducting oxide (TCO) materials are optically transparent and electrically conductive. As one of the most widely used TCO, indium-tin-oxide (ITO) has been widely studied and used in display industry and optoelectronics as an optical coating. The frequency range for ITO to exhibit negative permittivity is also in NIR, in which ITO is reported to have competitively low loss even compared to silver. The deposition of ITO films can be achieved through sputter deposition [78]. The major concern about using ITO is its price, and the instability of its optical property for different growth conditions. Similar materials include aluminum-zinc-oxide (AZO), gallium-zinc-oxide (GZO), etc [79].

### **1.3.3 Graphene and Others**

A few rarely-used yet interesting materials exist as potential candidates for plasmonic applications. Among them, graphene and polymer based plasmonics have attracted more and more attention, because of the distinguished electronic and optical properties. Graphene's plasmonic property has been predicted in [80]-[82], showing promising tunable optical conductivity. Standard approaches for graphene layer

deposition are limited at this time, although depositions based on transfer-printing method [83], CVD [84] and electrostatic method [85] have been reported.

#### **1.4 Modeling Technique**

Numerical modeling has become an essential part of nanophotonics research, by solving electromagnetic problems numerically – especially the Maxwell’s equations – on a computational electromagnetism basis. Previously, complex structures such as 3-D objects were investigated approximately from a semi-analytical approach. For instance, light scattering (including the famous Mie Scattering [86] [87]) from metallic spheres has been studied based on the series expansion of wave functions. This type of approximation usually suffers from several drawbacks. For one thing, the shape of scattering source could be too complex and unorthodox, when the integration with function series becomes analytically impossible. Even if the integration can be performed numerically, the series expansion does not necessarily converge in the same manner for different feature sizes, especially when the length scale of the problem drops to the deep subwavelength realm. Plus, broad-band and time-domain simulations are usually preferred for modeling optical communication devices. While analytical or semi-analytical analysis remains indispensable for solving electromagnetic problems, numerical solutions based on discretized spatial elements will greatly improve the efficiency and accuracy of nanophotonic design.

Many numerical methods have been developed and commercialized for end users. To name a few, Finite-Difference Time-Domain (FDTD) [88] [89], Method of Moment (MoM) [86], and Finite Element Method (FEM) [90], etc., have been widely used for solving EM problems of complex structures. Depending on the nature of the EM

problem, especially the finest feature size and the resonant frequency, it is important to choose the appropriate numerical method. For nanophotonics and plasmonics, the physical dimensions of scattering sources range from as small as  $0.001 \lambda_0$  to more than  $10 \lambda_0$ . For example, a plasmonic waveguide for 1550 nm light could possibly have a guiding core of as thin as a few nanometers, as well as a propagation length of 10 micrometers. In transmission line system, on the other hand, the working frequency is at a comparatively low end relative to the line dimension. In general, FDTD approach is better than MoM or FEM for broad-band, transient response problems, when the physical dimension is close to or larger than the working wavelength. For transmission line system, conventional antennas and other low-frequency problems out of the optical spectrum, MoM and FEM are usually superior choices. Specifically, FEM has better stability and can be very useful if EM field inevitably diverges in FDTD, which normally happens when metal penetrates through the absorption boundary.

In this dissertation, numerical modeling is primarily based on the FDTD method. The following sections will describe the principles and the typical modeling environment of FDTD simulations.

#### **1.4.1 Finite-Difference Time-Domain (FDTD) Method**

The finite difference used in FDTD methods can be explained based on the Yee cell [89] shown in Figure 1.11. The whole space of interest for modeling can be divided into multiple Yee cells, in the shape of the cubic cell in the Cartesian system. In this way, each cell has 6 faces and is neighbored to 6 other similar cells. The dimension of each cubic  $\Delta x \times \Delta y \times \Delta z$ , will determine the discretization of space derivative.

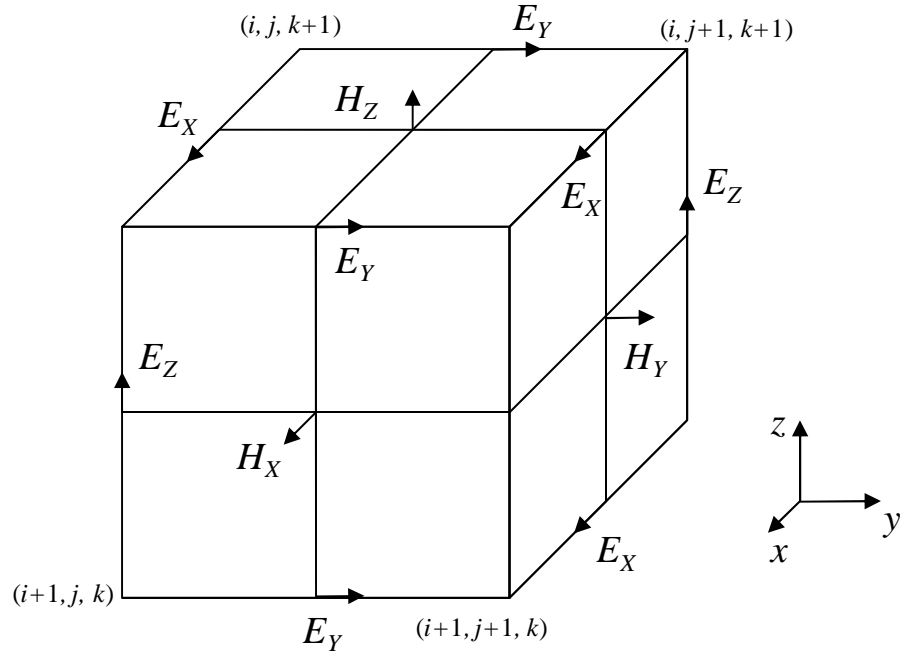


**Figure 1.11** The distribution of  $E$ -field and  $H$ -field components in a typical Cartesian Yee cell [89].

The field vector components discretized in each cubic, as shown in Figure 1.11, include the full vectors of both electric and magnetic field. Starting with Ampere's law and Faraday's law, the two curl equations including both time derivative and space derivative can be rewritten following the central difference approximation. In Figure 1.11, three  $H$  components are assumed to point outward normal to the 6 faces, while all three  $E$  components lie on the edge of the cell. As the spatial derivative can be rewritten with  $\Delta x$ ,  $\Delta y$  or  $\Delta z$ , the time derivative can be obtained from the difference of field values on different time-steps at the same location. As an example, if the curl equations are written in the form of

$$\nabla \times \bar{E} = -\mu \frac{\partial \bar{H}}{\partial t}, \quad (1.29)$$

$$\nabla \times \bar{H} = \varepsilon \frac{\partial \bar{E}}{\partial t} + \sigma \bar{E}, \quad (1.30)$$

the scalar form of a TE solution can be expanded to

$$\frac{\partial E_x}{\partial t} = \frac{1}{\varepsilon} \left( \frac{\partial H_z}{\partial y} - \frac{\partial H_y}{\partial z} - \sigma E_x \right), \quad (1.31)$$

$$\frac{\partial E_y}{\partial t} = \frac{1}{\varepsilon} \left( \frac{\partial H_x}{\partial z} - \frac{\partial H_z}{\partial x} - \sigma E_y \right), \quad (1.32)$$

$$\frac{\partial H_z}{\partial t} = \frac{1}{\mu} \left( \frac{\partial E_x}{\partial y} - \frac{\partial E_y}{\partial x} \right). \quad (1.33)$$

The central difference approximation will rewrite (1.31) - (1.33) as

$$\begin{aligned} & \frac{E_x^{n+1}(i, j, k) - E_x^n(i, j, k)}{\Delta t} \\ &= \frac{1}{\varepsilon(i, j, k)} \left\{ \frac{H_z^{n+1/2}(i, j+1/2, k) - H_z^{n+1/2}(i, j-1/2, k)}{\Delta y} \right. \\ & \quad \left. - \frac{H_y^{n+1/2}(i, j, k+1/2) - H_y^{n+1/2}(i, j, k-1/2)}{\Delta z} \right. \\ & \quad \left. - \frac{\sigma_x}{2} [E_x^{n+1}(i, j, k) + E_x^n(i, j, k)] \right\} \end{aligned} \quad (1.34)$$

$$\begin{aligned} & \frac{E_y^{n+1}(i, j, k) - E_y^n(i, j, k)}{\Delta t} \\ &= \frac{1}{\varepsilon(i, j, k)} \left\{ \frac{H_x^{n+1/2}(i+1/2, j, k) - H_x^{n+1/2}(i-1/2, j, k)}{\Delta z} \right. \\ & \quad \left. - \frac{H_z^{n+1/2}(i, j, k+1/2) - H_z^{n+1/2}(i, j, k-1/2)}{\Delta x} \right. \\ & \quad \left. - \frac{\sigma_y}{2} [E_y^{n+1}(i, j, k) + E_y^n(i, j, k)] \right\} \end{aligned} \quad (1.35)$$

$$\begin{aligned} & \frac{H_z^{n+1/2}(i, j+1/2, k) - H_z^{n-1/2}(i, j+1/2, k)}{\Delta t} \\ &= \frac{1}{\mu} \left[ \frac{E_x^n(i, j+1, k) - E_x^n(i, j, k)}{\Delta y} - \frac{E_y^n(i+1, j, k) - E_y^n(i, j, k)}{\Delta x} \right]. \end{aligned} \quad (1.36)$$

Eqs. (1.34) - (1.36) show the discretized Maxwell equation with time step  $\Delta t$  and grid size  $\Delta x$ ,  $\Delta y$  or  $\Delta z$ . To ensure the stability of computing, the courant condition [88] is required:

$$\Delta t \leq \frac{1}{v \sqrt{\frac{1}{(\Delta x)^2} + \frac{1}{(\Delta y)^2} + \frac{1}{(\Delta z)^2}}}. \quad (1.37)$$

Finally, to model EM problems when there is power scattered away from physical objects in a finite and closed region, it is essential to setup the outer radiation boundary condition. In FDTD, it is usually realized by wrapping the simulation region with perfectly matched layer (PML) [91].

#### 1.4.2 Modeling Setup

The setup of FDTD simulations starts with the definition of physical properties, and ends with the specification of monitors. For software with a graphical user interface (GUI) such as Lumerical's FDTD Solutions [92], this is achieved by firstly drawing objects in a computer-aided design (CAD) window. Optical properties such as dielectric constants can be assigned to the objects, followed by wrapping the objects in PMLs and initializing the meshing. Many commercialized FDTD software products have the capability to define ununiform meshgrids for ultra-fine features in order to obtain better accuracy without applying excessive finesse in the whole simulation region. At this point,

it is possible to choose the proper source type and put monitors inside the simulation area to record field values.

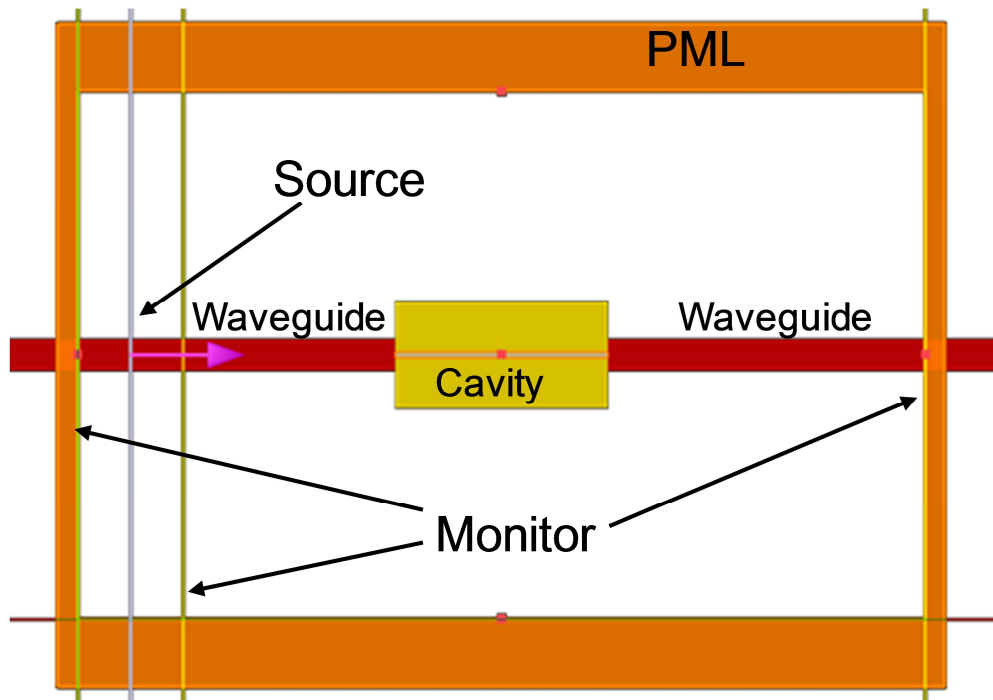


**Figure 1.12 FDTD simulation setup for modeling a plasmonic cavity in Lumerical FDTD Solutions 7.5.**

In Lumerical FDTD Solutions, as well as many other commercialized software packages, sometimes it is convenient to choose the “mode” type source. In this way, the source can be specified as an eigenstate accurately from the integrated mode solver. This can greatly shrink the total simulation volume and save the simulation time. Figure 1.12 shows all the primary components for a typical FDTD simulation, in which a plasmonic Fabry-Perot cavity is formed between silicon bus waveguides being 300 nm in width. This simulation is configured for 1550 nm light of TM polarization, for which the PML wraps  $8\ \mu\text{m}$  by  $5\ \mu\text{m}$  area. The cavity is  $2\ \mu\text{m}$  long, formed by a MIM waveguide with 30 nm wide airgap inside a gold block. The source is chosen as a fundamental TM mode for

1550 nm. The total simulation time is long enough for the power inside the cavity to dissipate and decay to less than  $1e-5$ .

Figure 1.13 plots static  $H$ -field of the demo simulation. The pattern shown in the input waveguide (left) side comes from the interference of the incident beam and the reflection from the cavity. Inside the cavity (between  $X = -1 \mu\text{m}$  and  $X = 1 \mu\text{m}$ ), the interference can also be seen clearly. By putting additional time monitors inside the cavity, it is also possible to calculate the  $Q$ -factor of the cavity.

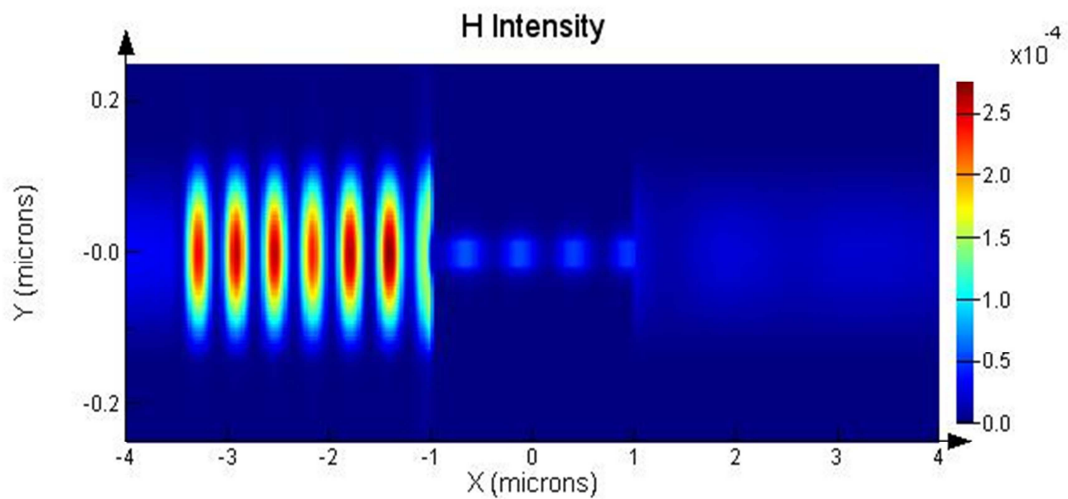


**Figure 1.13**  $H$ -Field intensity for the demo simulation shown in Figure 1.12.

## 1.5 Dissertation Overview

This dissertation presents numerical and experimental results of novel plasmonic devices and platforms featuring subwavelength confinement of electromagnetic waves, and they are structured as follows.

Chapter 2 presents the motivation, numerical modeling and the experimental verification of a 2-D plasmonic coupler integrated on-chip with silicon waveguides for 1550-nm light.

Chapter 3 introduces a 3-D design of a plasmonic taper directly coupled with silicon waveguides. The 3-D nano-plasmonic taper features a direct coupling mechanism to convert photons to SPPs, and an adiabatic approach to shrink the mode size of SPPs to 20 nm by 24 nm for near-infrared light.

Chapter 4 presents the experimental demonstrations of an integrated plasmonic junction with silicon waveguides on silicon-on-insulator substrate, based on the 3-D design in Chapter 3. The taper-pair plasmonic junction achieves high efficiency in photon-plasmon conversion for near-infrared light, and proves to be versatile in further decreasing the guiding mode area.

In Chapter 5, surface waves in the form of spoof plasmons are studied numerically based on metallic gratings coated by semiconductors in terahertz region. Various coating materials on the miniaturized surface corrugations are shown to be instrumental in determination of the guided modes' dispersion relation.

Chapter 6 investigates the periodic metal-insulator stacks as a host of super surface modes. The analytical solutions of the fundamental super mode are explicitly solved and then compared to full-vectorial simulation results. The tunable dispersion relation is then verified by experiments following the Kretschmann setup.

Chapter 7 will explore the possibility of active plasmonics based on the structures covered in previous chapters. Plasmonic modulation, NIR detection, and plasmonic photovoltaics are discussed based on preliminary results.

The work presented in this dissertation will finally be summarized in Chapter 8.

---

## 2 INTEGRATED PLASMONIC COUPLING

---

An efficient coupler between a dielectric waveguide and a plasmonic metal-insulator-metal (MIM) waveguide is proposed, modeled, fabricated, and characterized. Based on the platform of a silicon slot waveguide, a quasi-MIM plasmonic junction is formed via e-beam lithography and lift-off process. Coupling efficiency between the silicon slot waveguide and plasmonic waveguide up to 43% is obtained after normalizing to reference waveguides at 1550 nm. This coupling scheme can be potentially used for fast optical switching and small-footprint optical modulation [93].

### 2.1 Introduction

Plasmonics is revolutionizing the development of nanophotonics in every aspect at an extraordinarily fast pace. Recent breakthroughs have produced a wide range of nanoplasmonic devices that generate, guide, and detect light [94]-[96]. However, very few have been implemented. Currently, the challenge to integrate plasmonic devices with conventional dielectric waveguides on the same chip limits the wide applications of plasmonic devices. To this end, efficient coupling between dielectric waveguides and plasmonic waveguides is of great significance. Initially, a plasmonic waveguide was proposed with a single metal-dielectric boundary, which is still widely used [97]. However, direct excitation of surface plasmon waves on such a boundary from a dielectric waveguide or external source is inefficient due to the mismatch of k-vectors and field profiles of the two modes. Therefore, prism couplers [98] or grating couplers [99] are used to improve the efficiency. Due to their large size, prism couplers are not

suitable for photonic integrated circuits. On the other hand, the main drawbacks of grating couplers are (i) the separation of the source and plasmonic devices on different chips, (ii) the requirement of good alignment between the source and the grating, and (iii) their narrow bandwidth.

More recently, metal-insulator-metal (MIM) or metal-dielectric-metal waveguides have been investigated and experimentally demonstrated [100]-[105], where light propagation is confined between two metal slabs. These plasmonic slot waveguides have the advantages of small mode size and acceptable propagation loss. Recent numerical simulation [64] demonstrated that up to 70% efficiency can be achieved when light is coupled from a dielectric waveguide into a plasmonic waveguide. Direct fabrication of the dielectric-to-plasmonic waveguide coupler is challenging, especially considering the remaining metal on different waveguides' interface will block the wave propagation. A plasmonic junction that directly converts farfield radiation to surface waves has also been demonstrated recently [106]. The fabrication in Ref. [106] engages the use of focused ion beam twice, which requires additional curing process. The coupler involved in [53] is formed by enclosing a dielectric waveguide into metal claddings, which is hard to be used for optical sensors and modulators. Herein, we propose a practical configuration for integrated modulator and sensor applications, which can be used to achieve high coupling efficiency between dielectric waveguides and MIM plasmonic slot waveguides.

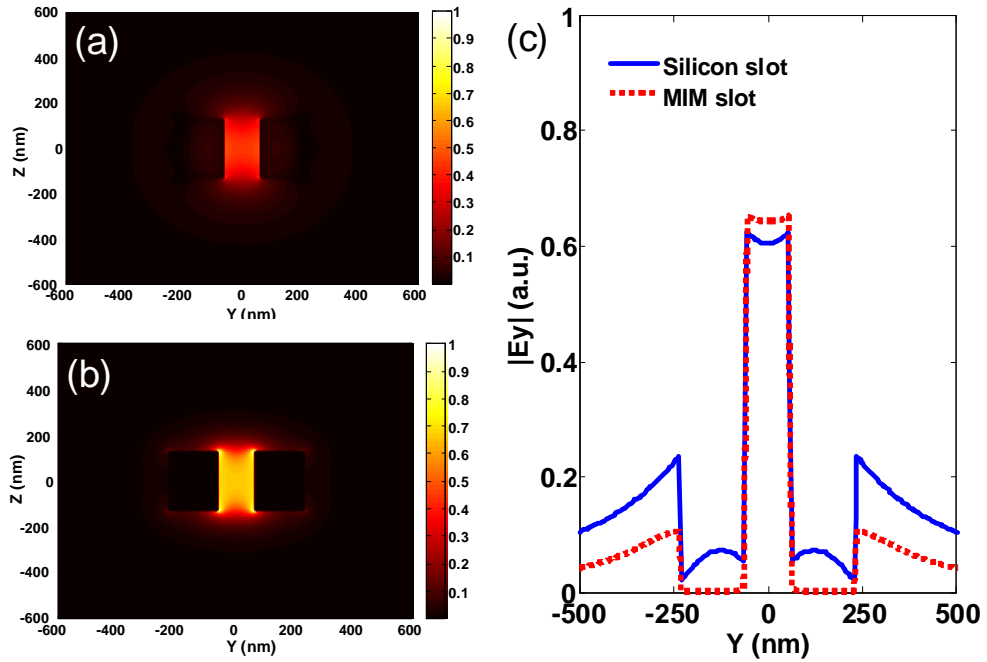


**Figure 2.1** (a) The power distribution in a dielectric slot waveguide. (b) The field distribution in a metal slot waveguide. Identical power flux is assumed for (a) and (b). The power density in MIM slot is obviously higher because of the presence of metal. (c) The field ( $|E_y|$ ) comparison (line-scan from Figs. 1(a) and (b)) between dielectric and MIM slot. MIM slot exhibits better field confinement as expected.

## 2.2 Design and Modeling

### 2.2.1 Mode resemblance: a mode-coupling consideration

Compact coupling from dielectric mode to plasmonic mode can be made more efficient in at least two ways. The first is to find a robust and monolithic momentum matching channel, which has been well addressed by using direct coupling scheme [64]. The second is to further engineer the mode profile to increase the mode profile matching (0) for better mode “overlapping”. This can be explained by coupled mode theory, in which the mode resemblance is deemed as an important factor to increase the coupling efficiency between two butt-connected waveguides [107] [108].

The concept of coupled mode theory can be traced back to the perturbation theory in quantum mechanics. The process of mode coupling can be perceived as happening between two different quantum systems, with different sets of eigenmodes. When the first system on a certain quantum state is operated to interfere the second one, there is only limited probability that a certain quantum state can be realized in the second system. This probability can be interpreted in a sense as related to the coupling efficiency, if the two systems are represented by two butt-connected waveguides. If the mode profile of the input waveguide can be expressed by an amplitude distribution as  $A(x)$ , while  $B_m(x)$  denotes the  $m$ th of the output waveguide, an overlap integral can be performed to evaluate this probability as [109]

$$\eta_m = \frac{\left[ \int A(x)B_m^*(x)dx \right]^2}{\int A(x)A^*(x)dx \int B_m(x)B_m^*(x)dx}. \quad (2.1)$$

Based on the overlap integral of Eq. (2.1) and especially the nominator of its right side, it is obvious that a better resemblance of  $A(x)$  and  $B_m(x)$  will yield a larger efficiency. Note that when the two eigenmodes equal with each other, which exactly describes the case of a continuous waveguide, the ‘‘coupling efficiency’’ is 100%.

Surface waves are usually bounded and displaying exponential decay from metal-insulator interface especially for subwavelength waveguides. However, the optical modes in conventional waveguides usually have a Gaussian-like distribution in guiding region as shown in Figure 2.2(a), and could hardly be made alike to their plasmonic counterparts (Figure 2.2(b)). In most high-index guiding waveguides, such as a silicon waveguide on an oxide substrate or an optical fiber, the field maximum is inside the core area instead of

on the core-cladding boundary. The details of the fundamental modes found in 2-D dielectric waveguides can be referred to Section 1.2.3.

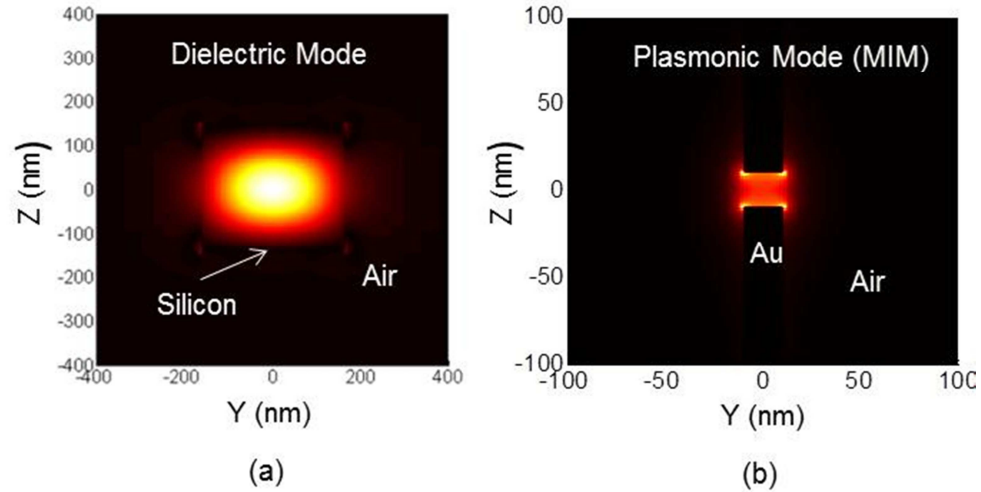


**Figure 2.2** An eigen-mode confined by (a) a 400nm by 300nm silicon core buried in the air or (b) 20nm by 20nm airgap between gold blocks for 1550 nm light.

To overcome this obstacle and increase the mode resemblance, we notice that light propagation can also be confined in low-index region when a slot is introduced inside a single mode dielectric waveguide [110], also known as the dielectric slot waveguide (Figure 2.3). Unlike the high-index guiding waveguide such as optical fibers, the dielectric slot waveguide uses a low-index core to concentrate the optical power. Interestingly, the low-index guiding core can be built even finer than what the diffraction limit predicts [110] [111], which is crucial to many applications such as compact optical circuitry [112] and the development of biomedical devices based on optical manipulation [113]. An analytical solution of the 2-D dielectric slot is also given as [110], in which  $k_H$  is the transverse wavenumber in the high-index slabs,  $\gamma_C$  is the field decay coefficient in the cladding,  $\gamma_S$  is the field decay coefficient in the slot.

$$E_x(x) = A \begin{cases} \frac{1}{n_s^2} \cosh(\gamma_s x), & |x| < a \\ \frac{1}{n_s^2} \cosh(\gamma_s a) \cos[\kappa_H(|x| - a)] + \frac{\gamma_s}{n_s^2 \kappa_H} \sinh(\gamma_s a) \sin[\kappa_H(|x| - a)], & a < |x| < b \\ \frac{1}{n_c^2} \left\{ \cosh(\gamma_s a) \cos[\kappa_H(b - a)] + \frac{n_H^2 \gamma_s}{n_s^2 \kappa_H} \sinh(\gamma_s a) \sin[\kappa_H(b - a)] \right\} \exp[-\gamma_c(|x| - b)], & |x| > b \end{cases} \quad (2.2)$$

Comparison of dielectric and metal slot waveguides shows that they work for the same polarization and share a similar hyperbolic cosine mode profile as shown in 0. Inspired by this similarity, we propose to couple light from dielectric slot waveguides into metal slot waveguides, namely the “slot-to-slot” coupler, as shown in Figure 2.4(a). Our 2-D numerical study has predicted a 61% transmittance for a 500-nm-long slot-to-slot coupling in Figure 2.4(b). By sweeping the slot length  $L$ , spectrum response representing Fabry-Perot effect (similar to that reported in [64]) is observed.

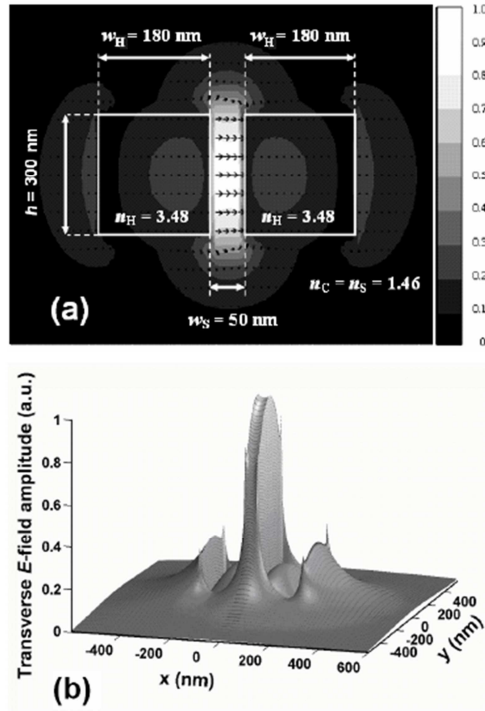


**Figure 2.3** Transverse E-field profile of the quasi-TE mode in a SOI-based slot waveguide. (a) Contour of the E-field amplitude and the E-field lines. (b) 3-D surface plot of the E-field amplitude. Adapted from [110].

### 2.2.2 Simulation results of a modified slot-to-slot coupling

From a practical view, however, the plain slot-to-slot scheme is still very hard to demonstrate on the silicon-on-insulator (SOI) platform because of the requirement for very critical alignment and the deep trenches milled into a bulk metal. To overcome these difficulties, we notice that the power skin depth of metal at  $\lambda = 1550$  nm is only a few nanometers. Therefore, a metal film embedded in a dielectric slot can be a good quasi-MIM waveguide as shown in Figure 2.5.

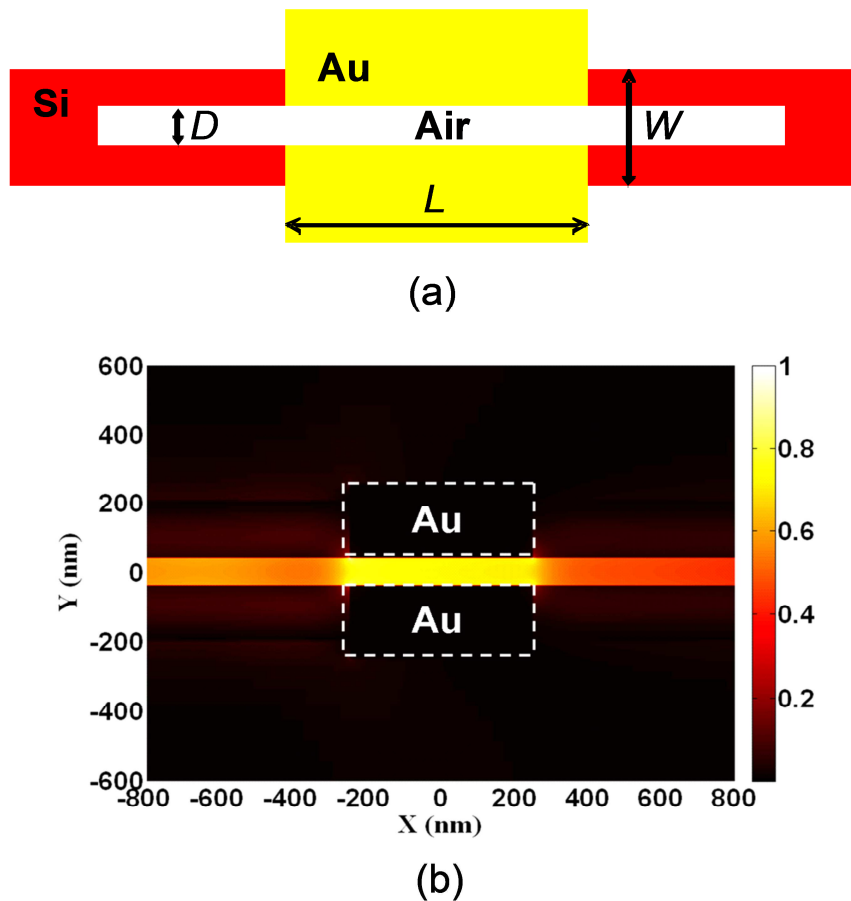


**Figure 2.4** (a) The layout of slot-to-slot coupler. (b) The power distribution from 2-D FDTD simulation for slot-to-slot coupler.

The three-dimensional structure is designed and modeled by FDTD simulation packages that support non-uniform meshing and eigenmode calculation. A cross-section of 260 nm by 460 nm ( $W = 460$  nm) is assumed for a single mode (SM) silicon strip waveguide that supports a fundamental TE-like mode (E-vector is in the slab) for near infrared light at 1550 nm. A slot is embedded in the strip waveguide with a slot width  $D = 120$  nm as shown in Figure 2.5(a). A plasmonic region with a total length of  $L = 500$  nm is then formed by isotropically adding a thin layer ( $\sim 20$  nm) of gold ( $\epsilon_r = -96 - j11$ ) [39] over the silicon slot, which produces an 80-nm wide airgap as shown in Figure 2.5(a). A quasi-TE-like polarization is used to retrieve an eigenmode of the silicon slot as the simulation source. Figure 2.5(b) illustrates transverse electric field  $E_y$  inside the quasi-MIM slot. For  $L = 500$  nm, the normalized transmission is close to 50%. From our simulation, when  $L$  keeps increasing to exceed  $1.5 \mu\text{m}$ , the propagation loss dominates and transmission decreases very fast.

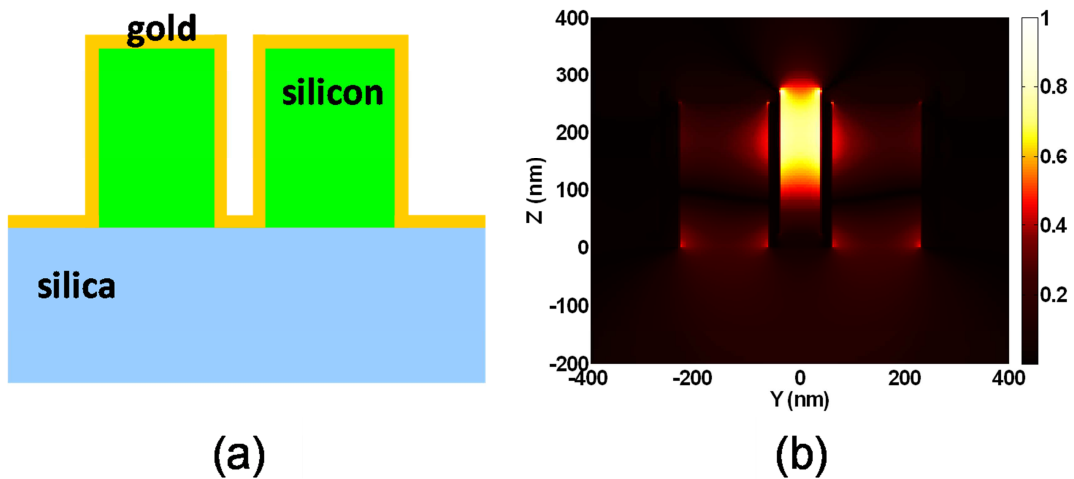


**Figure 2.5** (a) The cross-section view of the quasi-MIM structure. (b) The cross-section view of the field distribution  $|E_y|$  for the quasi-MIM structure from 3-D FDTD simulation.

## 2.3 Demonstration and Characterization

### 2.3.1 Sample preparation overview

In addition to equally high-level coupling efficiency as direct coupling, a remarkable advantage of our coupler is that it can be fabricated without using the focused ion beam (Figure 2.6). First, electron-beam lithography (EBL) and inductively coupled plasma (ICP) etch were used to pattern a 50- $\mu\text{m}$  long and 120-nm wide slot inside an SM silicon waveguide with cross-section around 260-nm-by-460-nm. The piece was then exposed by EBL again with bi-layer PMMA for lift-off. After development a 20- $\mu\text{m}$ -by-500-nm (or 20  $\mu\text{m}$  by 2  $\mu\text{m}$  for a second design) window was opened right at the center of the 50- $\mu\text{m}$ -long silicon slot, where obliquely evaporated gold was then deposited, followed by metal lift-off. The alignment tolerance of the two-step processing is up to tens of micrometers and therefore very easy to achieve via most EBL systems.

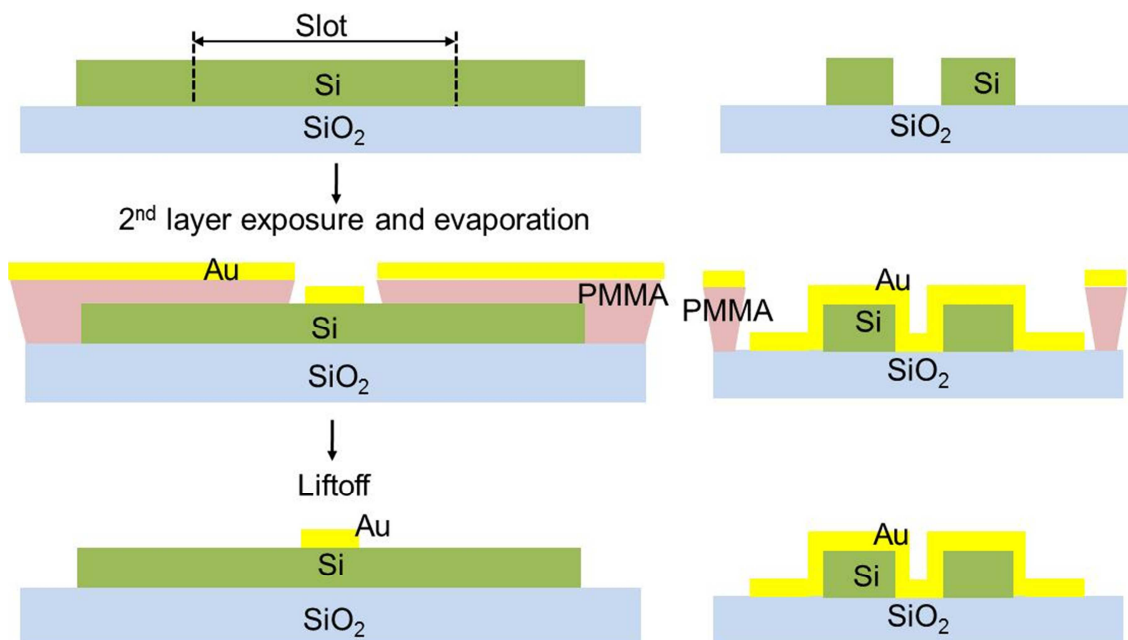


**Figure 2.6** Fabrication steps flow chart. The left panel shows the side view and the right panel shows the cross-section view in the light propagating direction inside the slot waveguide.

### 2.3.2 Fabrication flow

(1) Prepare a 6-inch silicon-on-insulator wafer. The device layer (silicon) used in the experiment is 300-nm thick. Use the standard RCA clean process to clean the wafer surface.

(2) To obtain the designed device thickness of 250nm, furnace treatment (dry oxidation) is required to thin the device layer. We have calculated the required thickness and the time needed based on the oxidation curve. An online calculation can be done at <http://www.cleanroom.byu.edu/OxideThickCalc.phtml>.

(3) Dip the wafer into a diluted HF tank such as Buffered Oxide Etch (BOE) to etch the top oxide cladding grown inside furnace. A 5-pt measurement is recommended afterwards to make sure the conformity of the silicon layer and the thickness of the device meet the requirement.

(4) Cleave the 6-inch wafer into 1 inch square small piece (approximately). The size of the piece should be chosen according to the dimension of the piece holder of the EBL system.

(5) Sit the small SOI piece on 120C hotplate for 3 min to dehydrate the surface.

(6) Spin-coat two layer PMMA 495 on top of the piece at 1200 rpm for a targeted 1500 nm each. Bake at 170C for at least 15 minutes for each layer.

(7) Pattern the alignment marks (JEOL 9300) at an averaged dose of 1800 mJ/cm<sup>2</sup>. The alignment marks consist of two global marks and several chip marks for multi-layer alignment. The alignment mark is a 'cross' shape covering approximately

2mm by 2mm. The chip mark is a smaller 'cross' shape. The line width of the alignment mark is 3  $\mu\text{m}$ .

(8) Develop in MIBK and IPA mixture (1:3) for about 90 sec. Rinse with IPA and blow dry with nitrogen.

(9) Etch the alignment mark through in  $\text{CHF}_3/\text{O}_2$  with Oxford 100 for 10-15 min. Etch rate is about 150 nm/min.

(10) Dip the sample into 1:1 mixture of Methylene Chloride and Acetone for at least 2 hours to strip the bi-layer PMMA. Rinse in IPA and use nitrogen to blow the piece dry.

(11) Spin-coat HSQ negative resist (XR-1541, 2%) at 3000 rpm for 60 sec for a targeted thickness of 100 nm. Bake the sample at 170C hotplate for 120 seconds.

(12) Pattern the silicon waveguides (JEOL 9300) at an averaged dose of 1200  $\text{mJ}/\text{cm}^2$ .

(13) Develop in MIF 300 for 3 min.

(14) Use PT770 left chamber (Silicon ICP etch) to etch the silicon with slight over-etch.

(15) Dip in diluted HF to remove the HSQ.

(16) Spin-coat PMMA 495 (8%) at 2000 rpm for a targeted thickness of 700 nm. This is followed by coating PMMA 950 (2%) at 2000 rpm for 100 nm. Bake for at least 15 min for each layer.

(15) Pattern the metal area (JEOL 9300) at an averaged dose of 1200  $\text{mJ}/\text{cm}^2$ .

(16) Develop in MIF 300 for 3 min.

(17) Descum in Oxford 81 with Argon etch for 3-5 seconds to clean the resist residue for better lift-off quality.

(18) Use e-beam evaporation to deposit 20 nm gold.

(16) Lift-off in 1:1 mixture of Methylene Chloride and Acetone for at least 2 hours to strip the bi-layer PMMA. Rinse in IPA and blow dry with nitrogen. Apply moderate ultrasonic if necessary.

(17) Spin-coat Shipley 1813 and bake at 90C to protect the device.

(18) Dice the piece with a dicing saw, polish the waveguides' input facet and strip the photoresist on top.

### **2.3.3 Testing and measurement**

The top-view under SEM shown in Figure 2.7(a) gives the overview of the fabricated device with very good alignment. The blurred image of the gold film shown in the zoom-out image comes from the limited depth of focus of the SEM. The dimension of the gap region covered by a gold film is marked in the bottom inset, in which the focus is set up for viewing the gold region. The fabricated slot has a width of about 124 nm, and the reduced gap (about 95 nm) has the gold film wrapping.

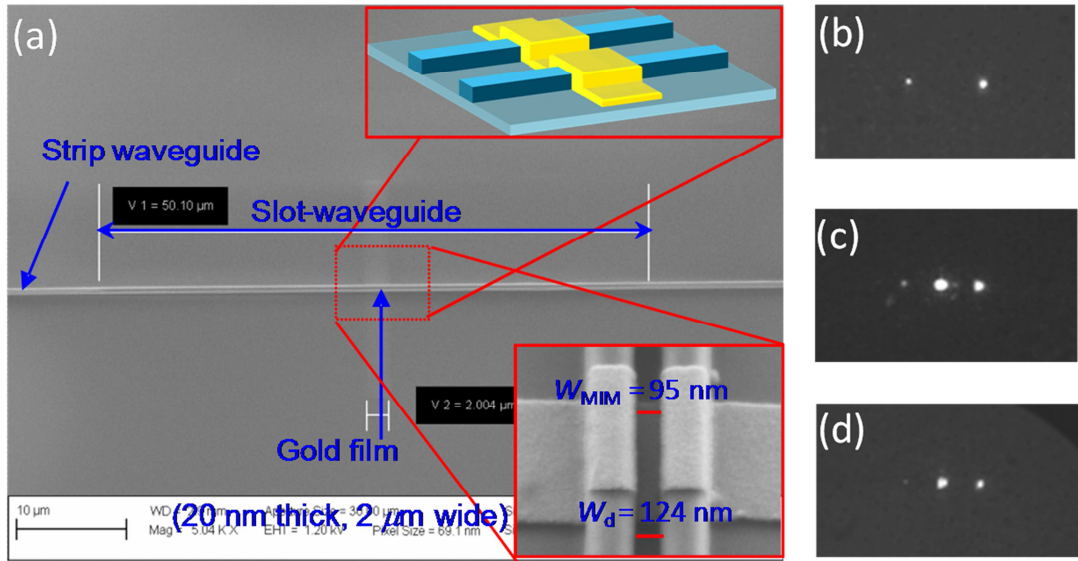


**Figure 2.7** (a) Device top-view with quasi-MIM region sketched (top inset) and shown by SEM picture (bottom inset). (b) Device top-view for scattering of near-infrared light from a silicon slot when power is coupled from an SM silicon waveguide on the right-hand side. (c) Light scattered from a dielectric slot with 500-nm quasi-MIM. The weakened scattering compared to (a) denotes the loss introduced by the quasi-MIM region.

To characterize the structure, we fabricated three structures altogether on an SOI wafer. The first one is an SM waveguide (with 50- $\mu\text{m}$ -long slot waveguide included) without any plasmonic region, and is therefore regarded as a reference structure. Two designs with different  $L$  values (500 nm and 2  $\mu\text{m}$ ) are fabricated to characterize the quasi-MIM region. A tunable laser with the maximum output power of 20 mW is used as the probing source. The devices are then viewed by an infrared camera working with a microscope as given in Figure 2.7(b)-(d). There is considerable scattering when light is coupled between the dielectric strip and the dielectric slot waveguide, which accounts for a large part of insertion loss. This issue can be addressed by strip-to-slot waveguide transformers [114], [115], where nearly perfect coupling can be achieved. Compared to the reference structure where no metal segment exists (Figure 2.7(b)), the scattering on

the output port (the bright points on the left) seen in Figure 2.7(c) and (d) are weaker but still obvious. The plasmonic device is characterized by normalizing its output to that of the dielectric slot waveguide, which avoids the consideration of strip-to-slot insertion loss.

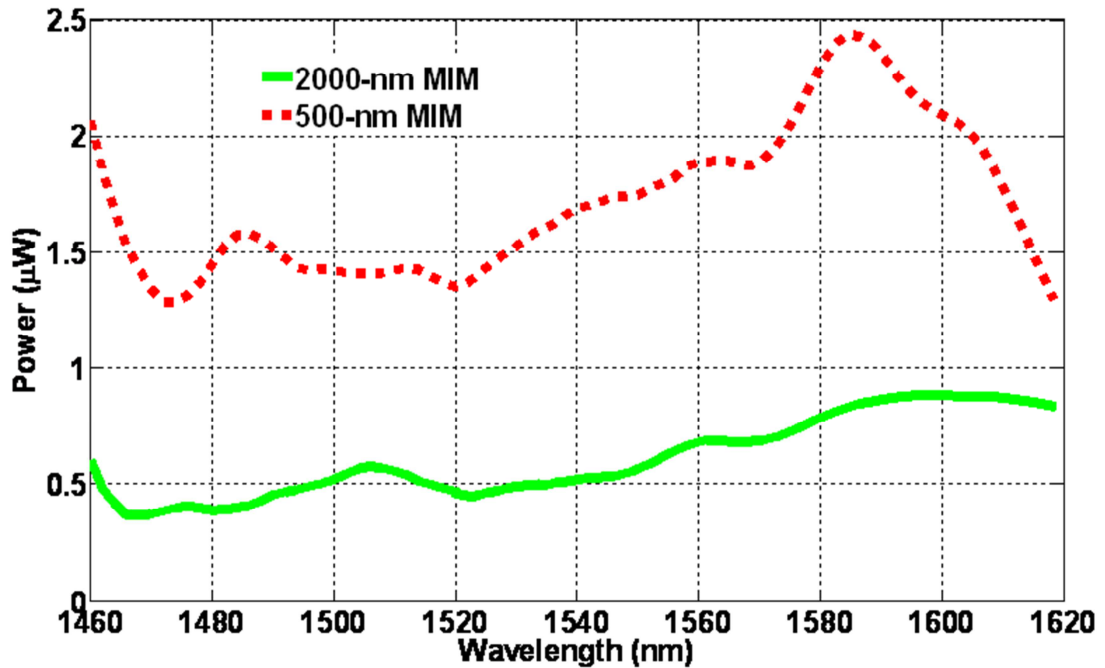


**Figure 2.8** The spectrum response between 1460 nm and 1620 nm of two quasi-MIM designs. The averaged power is approximately  $1.7 \mu\text{W}$  for 500-nm case and  $0.6 \mu\text{W}$  for 2- $\mu\text{m}$  case for this frequency range.

To verify the larger bandwidth of direct coupling compared to grating coupling, we scanned the wavelength of a tunable laser and measured the transmission accordingly. Here the input laser's power level is locked at 10 mW. The result of the reference structure (without MIM region) indicates that the platform supports efficient propagation of light with wavelength between 1460 nm and 1620 nm. For the band between 1460 nm and 1620 nm, the averaged output of dielectric slot waveguide is  $4 \mu\text{W}$ . Spectrum sweep

is then performed for the two MIM cases. After averaging the results and looking at the power around 1550 nm, we obtain  $\sim 1.7 \mu\text{W}$  output (or 43% transmission, normalized to the  $4\text{-}\mu\text{W}$  output from reference) for  $L = 500 \text{ nm}$  case and  $\sim 0.6 \mu\text{W}$  output (15% transmission) for  $L = 2 \mu\text{m}$  case (Figure 2.8).

## 2.4 Discussion

The transmission difference between the two designs corresponds to a propagation loss of  $\sim 2 \text{ dB}/\mu\text{m}$  for the fabricated quasi-MIM structure. However, previous analytical study of propagation SP modes in MIM structure has highlighted the role of multimode interference (MMI) [116], which indicates a critical relevance between the length of waveguide and the field distribution at output. To thoroughly characterize the quasi-MIM configuration proposed, including measuring the propagation loss of unit length, a different approach considering the role of MMI is necessary. The broadband performance is facilitated by “funneling” of power into MIM slot [117], besides impedance match and mode overlap. The mechanism of the nano-funneling effect can be numerically studied by transmission line theory [49] or antenna theory that has been carried out for microwave region. We believe the scheme proposed here can be further optimized if the mechanism of direct-coupling can be understood more thoroughly.

## 2.5 Conclusions

In this project, I introduced the design and demonstration of an integrated coupler that combines plasmonic devices with dielectric waveguides for near infrared light. The performance of this coupler is in agreement with 3-D FDTD simulation, shows efficient coupling, acceptable bandwidth and straightforward fabrication. Based on the platform described in this chapter, plasmonic switches or modulators with an active length of only

a few micrometers are expected if the propagation of SPP can be modulated in previous approaches [118]. Structures based on this platform is discussed and further explored for active plasmonics (Chapter 8).

---

## 3 NANOPLASMONIC FOCUSING IN THREE DIMENSIONS

---

Recent work has demonstrated transmission of light through deep subwavelength slits or light coupling into waveguides with deep subwavelength dimension only in one direction. In this chapter, we propose an approach to squeeze light ( $\lambda = 1550$  nm) from a dielectric waveguide into a deep subwavelength spot. Vertical confinement is achieved by efficiently coupling light from a dielectric waveguide into a 20-nm metal-dielectric-metal plasmonic waveguide in two dimensions. The horizontal dimension of the plasmonic waveguide is then tapered into 20 nm. Numerical simulation shows that light fed from a dielectric waveguide can be squeezed into a 21nm-by-24nm spot with efficiency 62% [119].

### 3.1 Introduction

To couple light into a waveguide supporting nanoscale mode size and hence to squeeze light into an ultrasmall spot are critical to imaging quality, data storage, manipulation of nanostructures, and optical lithography in semiconductor industry. The extremely high light intensity resulted from the ultrasmall spot will greatly increase the nonlinear effect and can be used to make ultrasmall and ultrafast electric-optic or all-optic modulators. Recent progress in plasmonics provides new insight into this topic [120] [121]. One approach is based on the small mode size supported by plasmon-based media and light can be squeezed into a subwavelength aperture or propagates in a subwavelength waveguide. Directly coupling light into a deep subwavelength circular or

square aperture was shown with very low efficiency. Therefore, recent work is focused on transmitting light through deep subwavelength slits or coupling light into waveguides with deep subwavelength dimension only in one direction [122].

Extraordinary optical transmission was first observed through arrays of subwavelength holes. Each hole has a diameter (150 nm) slightly smaller than diffraction limit of light ( $\lambda=326$  nm) [35]. The transmission through the aperture can be enhanced by fabricating periodic grooves surrounding the apertures [123]. Following the same principle, beaming light from a single subwavelength aperture was reported [124]. Two types of apertures were used in this work: a circular aperture with diameter 250 nm, which is slightly smaller than diffraction limit for visible light, and a slit aperture with deep subwavelength dimension in one direction, 40 nm, but in another dimension, 4400 nm. If another deep subwavelength confinement by metal is applied, a cutoff frequency will be imposed and the transmission is extremely small. Resonant optical antennas considerably shorter than one-half the wavelength were shown to enhance field in the antenna feed gap and lead to white-light supercontinuum generation [125]. However, the low coupling efficiency and side lobes constitute significant drawbacks for practical applications. Light propagation along a chain of gold particles with dimensions  $100 \times 100 \times 40$  nm<sup>3</sup> deposited on an ITO substrate was observed in the visible light regime ( $\lambda=633$  nm) [126]. Yin, et al. [127], demonstrated light ( $\lambda=532$  nm) guiding along a silver strip with cross section  $250 \times 50$  nm<sup>2</sup>. Numerical simulation of a nanowire taper [128] and experimental demonstration of a planar taper [97] were recently reported, where photons are converted into surface plasmon polaritons (SPPs) and propagate along the surface of a tapered nanowire or waveguide. These research results are exciting and

indeed constitute breakthroughs towards deep subwavelength photonics. However, they either provide deep subwavelength dimension only in one direction, or require very complicated coupling configurations, or are not easy to integrate into a nanophotonic chip. For the tapered nanowire presented in [128], it is very difficult to address several challenges for practical applications: (1) how to couple light onto such a tapered nanowire; (2) how to integrate it into a photonic chip; (3) how to decrease surface scattering; (4) how to avoid unacceptably large loss at the tip. Herein, we propose a straightforward yet effective approach, as shown in Figure 3.1, to *three-dimensionally* squeeze near infrared light through a *single* aperture and focus it into a spot with dimensions only 20~30 nm. To this end, we have combined two recent findings: (1) high efficiency can be achieved for directly coupling light from a dielectric waveguide into a metal-insulator-metal plasmonic waveguide; (2) a 3-D nanoscale metal-insulator-metal (MIM) plasmonic waveguide with large dielectric constant contrast supports a small size mode with acceptably low loss (effective index is very small). In this device, the squeezing process is accomplished in two steps: in a coupling process, the vertical dimension is shrunk; in a tapering process, the horizontal dimension is squeezed.

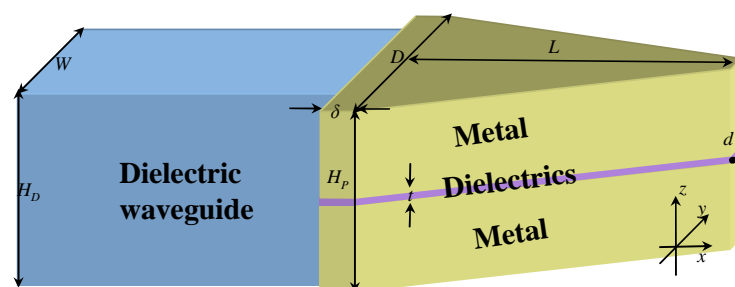


**Figure 3.1** Illustration of the coupler and nanotaper.

## **3.2 Modeling Setup and Design**

### **3.2.1 Motivation**

To decrease the surface scattering, an MIM plasmonic waveguide is used in our device. Efficient light coupling from dielectric waveguides into MIM plasmonic waveguides was numerically investigated in recent work [64], [129]. It has been shown that the effective transmission cross section of an MIM waveguide is surprisingly much larger than the geometrical dimension of the dielectrics between the metal slabs. This helps the transmission cross section match between a dielectric waveguide and an MIM plasmonic waveguide. A detailed theoretical explanation based on impedance matching viewpoint is recently presented [129], which successfully interpret the surprisingly high coupling efficiency and sheds light on further optimization method of direct-coupling scheme. Although a detailed microscopic explanation for this has not been seen yet, the light transmission enhancement on nanoscale antennas [125] or by periodic textures may partially account for the high transmission [130]. In particular, the surface plasmon polaritons at the coupling boundary play a key role in improving the efficiency. The light wave from the dielectric waveguide excites SPPs along the dielectric-plasmonic boundaries and the SPPs will be “funneled” into the MIM plasmonic waveguide. Note that SPPs can propagate along sharp bends with low loss [48].

### **3.2.2 Modeling setup for transmission calculation**

In 3-D finite-difference time-domain (FDTD) simulations performed below, we define three monitors to capture the source power (S), transmitted power (T) and reflected power (R). The definition of device transmission is given by  $T/(S+|R|)$ . Here the monitor S is placed right after the source, and monitors R and T are put close to the PMLs (Figure 3.2). The device (not shown) is usually put between the monitors S and T.

As a result, all the power on the left side of S comes from reflection. Therefore, the absorption including scattering loss can be estimated by  $1-T/(S+|R|)-|R|/(S+|R|)$ .

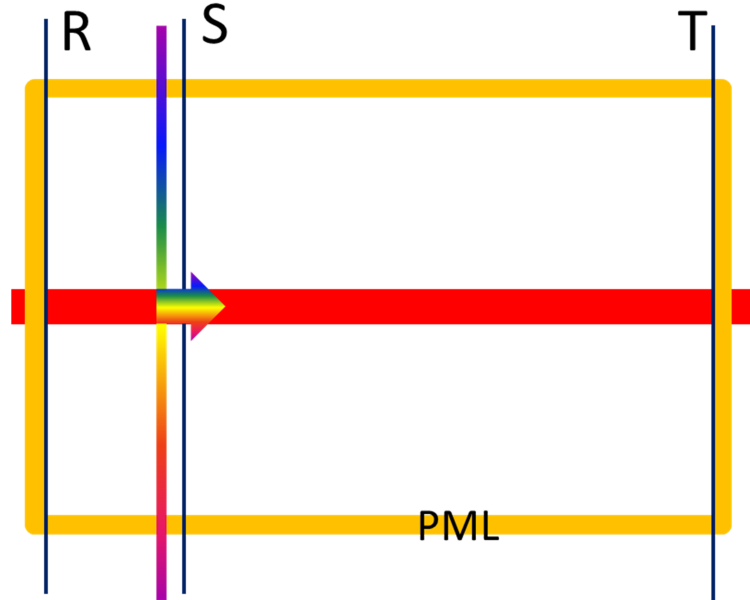


**Figure 3.2** The 3-monitors setup to calculate the transmission, reflection and loss of the system.

### 3.2.3 Direct coupling in the vertical direction

The theory of operation and efficiency optimization of the coupler are not the center of our attention in this work. Instead, we use the reported finding to realize light-squeezing in one direction. Two-dimensional finite-difference frequency-domain simulations were performed in [64] for light direct coupling from a dielectric waveguide into an MIM plasmonic waveguide with high efficiency. The 2-D simulations promise to be valid for plasmonic waveguides with large dimensions in the third direction. To verify this, we performed a 3-D FDTD simulation of light ( $\lambda=1550$  nm) coupling from a dielectric waveguide (Si,  $\epsilon_r=12.25$ ) with width  $W=320$  nm and height  $H_D=300$  nm into a plasmonic waveguide with dielectrics ( $\text{SiO}_2$ ,  $\epsilon_r=2.25$ ) thickness  $t=20$  nm sandwiched

between two silver slabs. The dielectric and MIM plasmonic waveguides are aligned at the center. The overall dimensions of the MIM waveguide,  $D=400$  nm and  $H_p=400$  nm, are designed to be larger than the dielectric waveguide to eliminate the transmission through edges. In the simulation, the  $E_{11}^z$  mode (the main component of electric field is along the  $z$ -axis; the main component of magnetic field is along the  $y$ -axis) of the dielectric waveguide is chosen to effectively excite surface plasmon polaritons. This is essentially the configuration of light coupling from a dielectric waveguide into a nanoscale slit if the length of the plasmonic waveguide is very small. A plasmon dispersion model is applied in the simulation with dielectric constant of silver based on [131],  $\epsilon_r = -129+3.2j$ , and set in a commercialized software package [92]. In particular, we use a nonuniform orthogonal grid with mesh size 1 nm in the plasmonic waveguide to satisfy accuracy in allowed computation capability. The coupling efficiency is found to be 81% excluding the propagation loss in the plasmonic waveguide. It has been shown that the coupling efficiency can be improved to over 90% if suitable multisection tapers are designed [64], [129]. On the other hand, the coupling efficiency will be very poor if the dimension in the horizontal direction is deep subwavelength simultaneously because this will decrease the effective transmission cross section of the MIM plasmonic waveguides.

Once light is coupled into the nanoscale MIM plasmonic waveguide, very good confinement can be achieved in the vertical direction. The size of the mode in the vertical direction, determined by the geometric thickness of the dielectrics and the evanescent tails ( $<1$  nm in this case) in the surrounding metal slabs, is calculated to be 21 nm.

### 3.2.4 Adiabatic tapering in the horizontal direction

To also achieve nanosqueezing in the horizontal direction, we introduce an integrated taper in the horizontal direction into our structure, as shown in Figure 3.1. Various plasmonic taper designs have been studied theoretically or experimentally for multiple applications. The first group of tapers adiabatically decrease the distance between metal cladding. Pile, et al. [132] and Ginzburg, et al. [122] numerically investigated, and Chen, et al. [53] experimentally demonstrated light coupling from a dielectric waveguide into plasmonic tapers. However, their tapers provide deep subwavelength confinement only in one direction. In addition, their structures are formed by tapering the gap between the metal slabs. In contrast, our sandwiched taper is surrounded by air and nanoscale guided modes can be supported between the metal layers (i.e. smaller spot size can be obtained). Our approach is also different from the work presented in [97], where light is originally with a large evanescent tail into substrate and finally get “stuck” on metal surface like a conical waveguide described in [128]. As shown in Figure 3.1, the input port width of our taper is  $D=400$  nm, the width of the taper tip is  $d=20$  nm, and the taper length is  $L=550$  nm. Between the silicon waveguide and the plasmonic taper there is a section of uniform transient plasmonic waveguide ( $\delta=50$  nm). By combining the input silicon waveguide, we repeat the FDTD simulation of the 3-D structure at 1550 nm. In this case, the 20nm-by-20nm nanotip is inserted into a PML to avoid back-reflection from the air. We approximate here a situation that no output waveguide is attached so as to focus on the photonic-plasmonic conversion of the taper and temporarily neglect the transition loss from taper-tip to additional devices. Our simulation shows that this is a reasonable approximation which does not hide any features of our coupler.

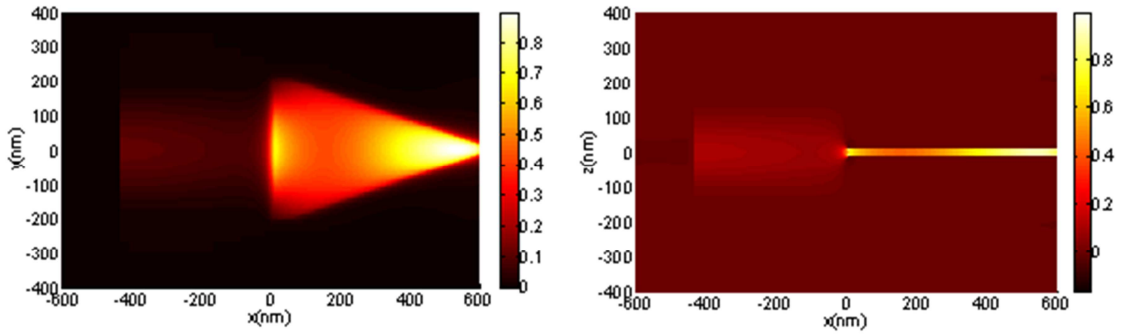


**Figure 3.3** Simulation of light coupling from a dielectric waveguide into the MIM plasmonic taper: (a) the  $S_x$  distribution in the horizontal plane; (b) the  $S_x$  in the vertical plane.

Figure 3.3 (a) and (b) show  $S_x$ , power flow distribution along the propagation direction, in the horizontal ( $z=0$ ) and vertical ( $y=0$ ) planes, respectively. The MIM plasmonic taper gathers a large amount of power from the dielectric waveguide and the power density becomes progressively stronger when light propagates toward the taper tip.

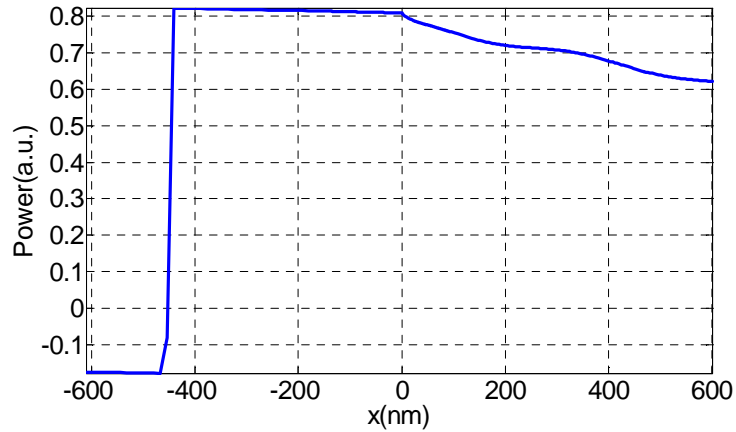


**Figure 3.4** The x-component of power flow ( $P_x$ ) along the x-axis.

As shown in Figure 3.4, by integrating  $S_x$  in the dielectric waveguide and the plasmonic waveguide taper and considering the back-reflection (negative value, 18%) from their interface, the overall efficiency (including propagation loss) is 62%. About

20% of power accounts for the transverse scattering at the interface and propagation loss in the MIM plasmonic taper.

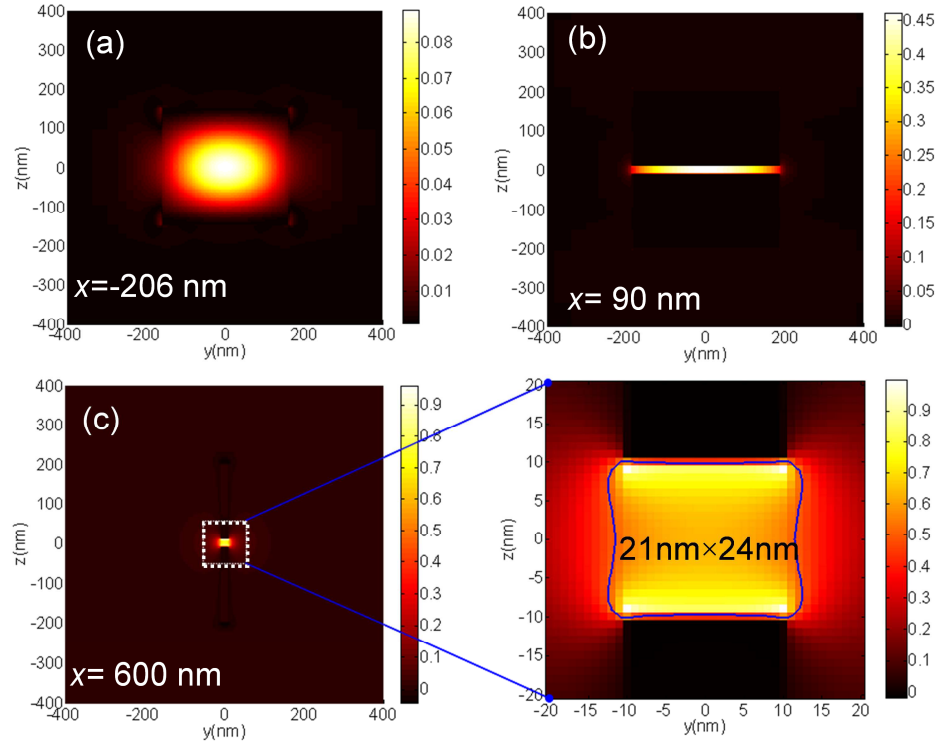


**Figure 3.5** The spot size at different locations along the x-axis.

### 3.3 Results and Discussion

#### 3.3.1 Field confinement and enhancement

Figure 3.5 (a)-(c) show  $S_x$  in the dielectric waveguide, in the transient plasmonic waveguide, and at output ports, respectively. As can be seen, the light power from the silicon waveguide is focused into a nanospot in both horizontal and vertical directions after the two-step squeezing process. In the coupling process, the vertical dimension is shrunk; in the tapering process, the horizontal dimension is squeezed. The dimensions of the spot at the output port are measured by full width at half maximum to be 21 nm in the vertical direction and 24 nm in the horizontal direction, which are close to the mode

dimensions of a 20nm-by-20nm silver-SiO<sub>2</sub>-silver plasmonic waveguide. Compared to the mode size of 232nm-by-156nm in the dielectric waveguide, the mode area has been shrunk to even smaller than 1/50.

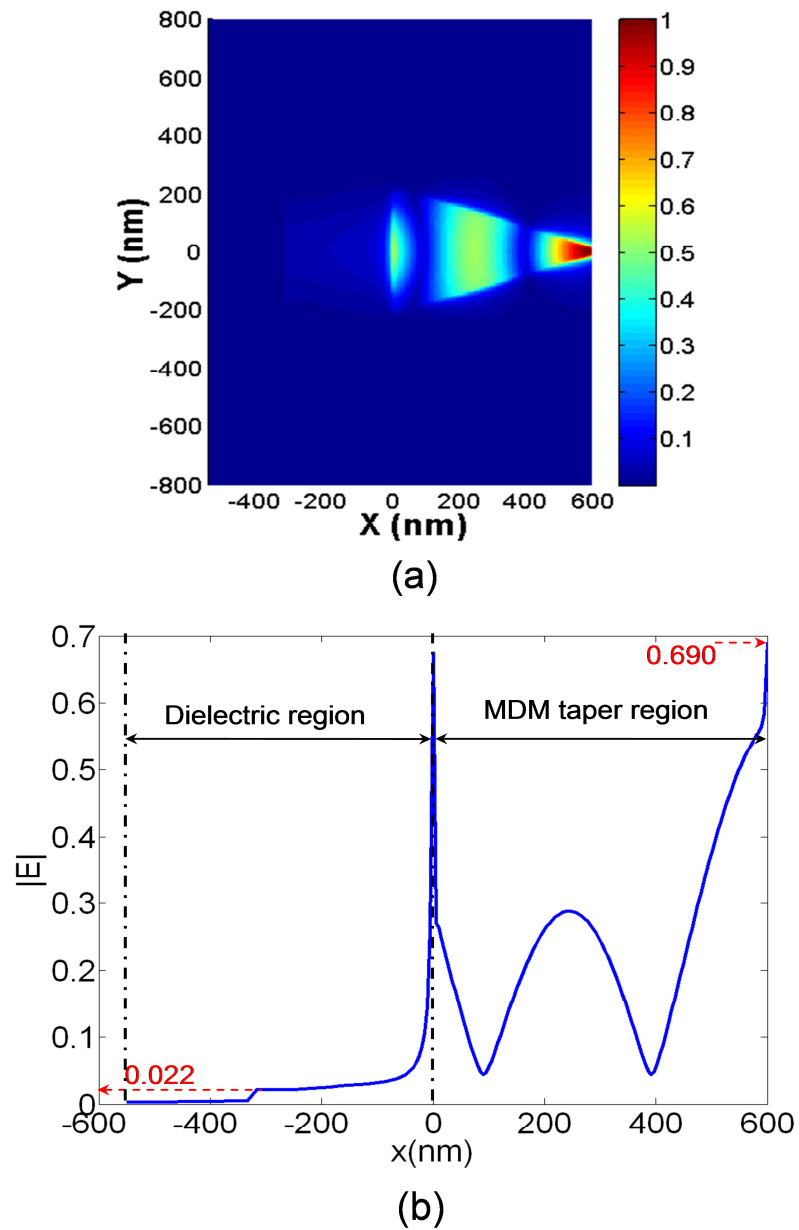


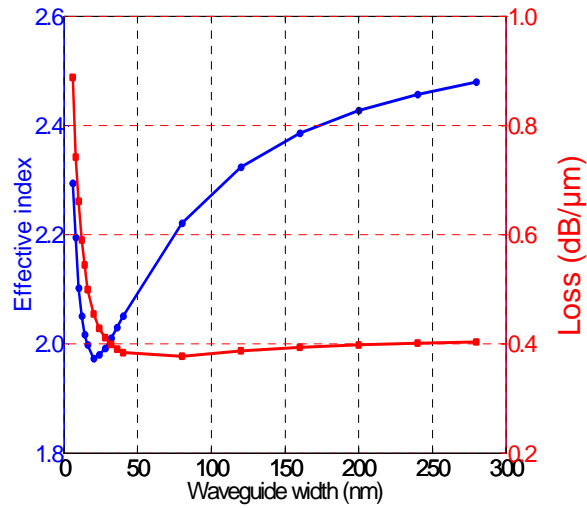
**Figure 3.6** (a) The distribution of electric field amplitude  $|E(r)|$  at the plane  $z=0$ . (b) The electric field amplitude  $|E(r)|$  at the central axis ( $y=0; z=0$ ) along the propagation direction.

With propagating light confined to such small dimensions, remarkable field enhancement is also observed. To illustrate the enhancement, Figure 3.6(a) shows the electric field amplitude  $|E(\mathbf{r})|$  distribution at the plane  $z=0$  and Figure 3.6(b) plots the electric field amplitude along the propagation direction at the central symmetry axis ( $y=0$ ;  $z=0$ ). In both case, the maximum amplitude at the plane  $z=0$  is normalized to 1. As can be seen, an electric field enhancement of 31 times, or 961 times of light intensity (by  $|E(\mathbf{r})|^2$ ) can be obtained at the very end of the output port. At the dielectric-metal boundaries, the enhancement is even stronger (over 3 orders of magnitude of intensity). The variation of the amplitude along x-axis is mainly due to the Fabry-Perot effect, and its impact will be analyzed in the following paragraph.

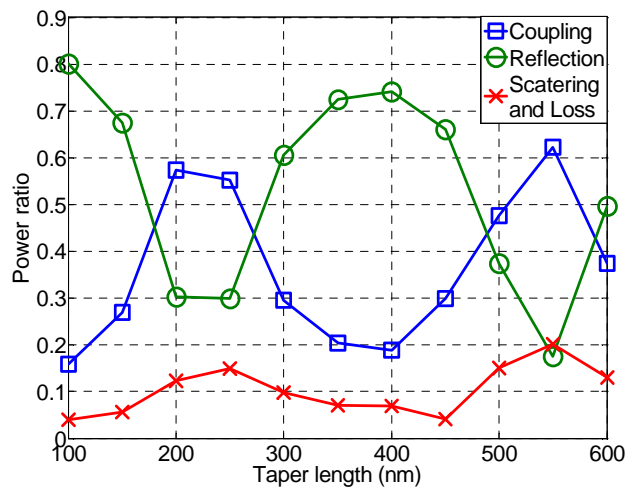
In our case, the taper functions as a mode converter from a mode with a large dimension ( $\sim 200$  nm) into a mode with a small dimension (24 nm) in the horizontal direction. The MIM plasmonic waveguide, even with dimensions of 20nm-by-20nm, supports a fundamental bounded mode with its size almost linear to the physical dimension of the dielectric core, exhibiting no cutoff in deep subwavelength regime [46], [133]. Due to large magnitude difference between the dielectric constant of the dielectrics ( $\epsilon_r=2.25$ ) and that of silver ( $\epsilon_r=-129+3.2j$ ) at  $\lambda = 1550$  nm, the effective index of the plasmonic waveguide is very small [133]. As a result, the propagation loss in the taper can be controlled in an acceptable range as shown in Figure 3.7(a). Note the propagation distance in the MIM plasmonic waveguide, even with dimensions 20nm-by-20nm (with propagation loss  $0.45$  dB/ $\mu\text{m}$ ), can run up to several micrometers, matching the predictions given in [133]. Although shorter tapers may help decrease the total propagation loss, we find shorter tapers will result in larger back reflection. In other

word, the taper angle is not the decisive factor for optimal transmission. Figure 3.7(b) shows the relation between the taper length and the efficiency.

### 3.3.2 Mode conversion and Fabry-Perot effect



(a)



(b)

**Figure 3.7** (a) The effective index and loss for the 20 nm thick MIM plasmonic waveguide with different widths. (b) The overall efficiency for tapers with different lengths.

The Fabry-Perot effect comes from the interference of plasmon waves propagating in different directions, one in the transmission direction and the other in the reflection direction. The reflection is expected along the tapering and especially close to the tip region. The physical nature of MIM waveguides shown in Figure 3.7(a) determines the effective index range of the plasmon waves supported. For waveguide width spanning from 20 nm to 300 nm, the effective index is transitioning smoothly, and there is a notable dip in the effective index plot around 20 nm. This has also predicted the speed of the plasmon wave close to the tip of the taper, and verified that the wave is not drastically slowed down at the deep subwavelength regime. The peak-valley distance shown in Figure 3.7(b) resides in an estimation range given by  $\lambda/2n_{\text{eff}}$  when  $\lambda$  is 1550 nm and  $n_{\text{eff}}$  can be seen as an averaged value between 2 and 2.4.

According to the loss evaluation shown in Figure 3.7(a), it is not preferred to further increase the width of the input waveguide because of its higher loss. This can also be appreciated by the plot for transmission/loss versus taper lengths in Figure 3.7(b). Therefore, from a propagation wave's perspective, the tapering angle would not be the decisive factor as crucial as the taper length regarding the total transmission. The peak-valley distance will be determined by the effective index of the taper section, which changes moderately in a very small span. Based on Figure 3.7(a), a local transmission peak will be observed every 300-400 nm.

### 3.3.3 Discussion of potential applications

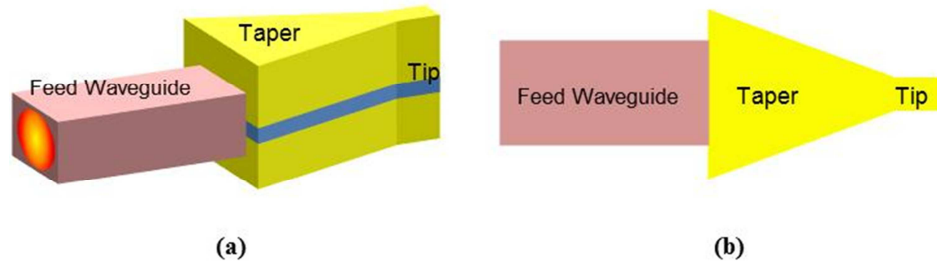


**Figure 3.8** (a) 3-D and (b) top view of the integrated plasmonic mode transformer with a nano-tip extended from the taper end.

Using the taper shape shown above, the tip of the taper could also be “extended” for different applications, in a fashion described by Figure 3.8, where the taper tip bears SPP wave propagation in a subwavelength MIM waveguide. At least two potential applications should be considered for this configuration. The first is to treat the extended tip as a subwavelength plasmonic waveguide as an integrated component in optical subsystems, which will be explained in the next chapter as a 3-D plasmonic junction bridging the optic communication channels (Figure 3.9).

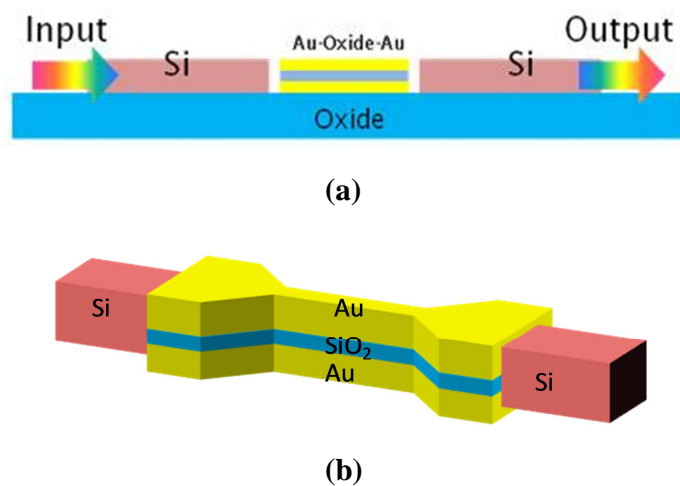


**Figure 3.9** Schematic view of (a) the 2-D side-view and (b) the 3-D-view of a nano-taper pair connected with silicon strip waveguides.

The second approach is to regard this tip as an optical focusing device with extremely focused power profile. Compared to the traditional near-field optical microscopy (NSOM) type configuration such as a coated optical fiber tip, the lateral taper structure has more efficient power delivery to the end, which is important for design of optical heads in storage. One advanced technique in hard-disk drive manufacturing, heat-assisted magnetic recording (HAMR, [134]), requires focused energy to heat the recording layer so that the raised temperature can modulate its magnetic property. The more confined the radiated energy can be, the higher aerial density of the stored data would be possible.

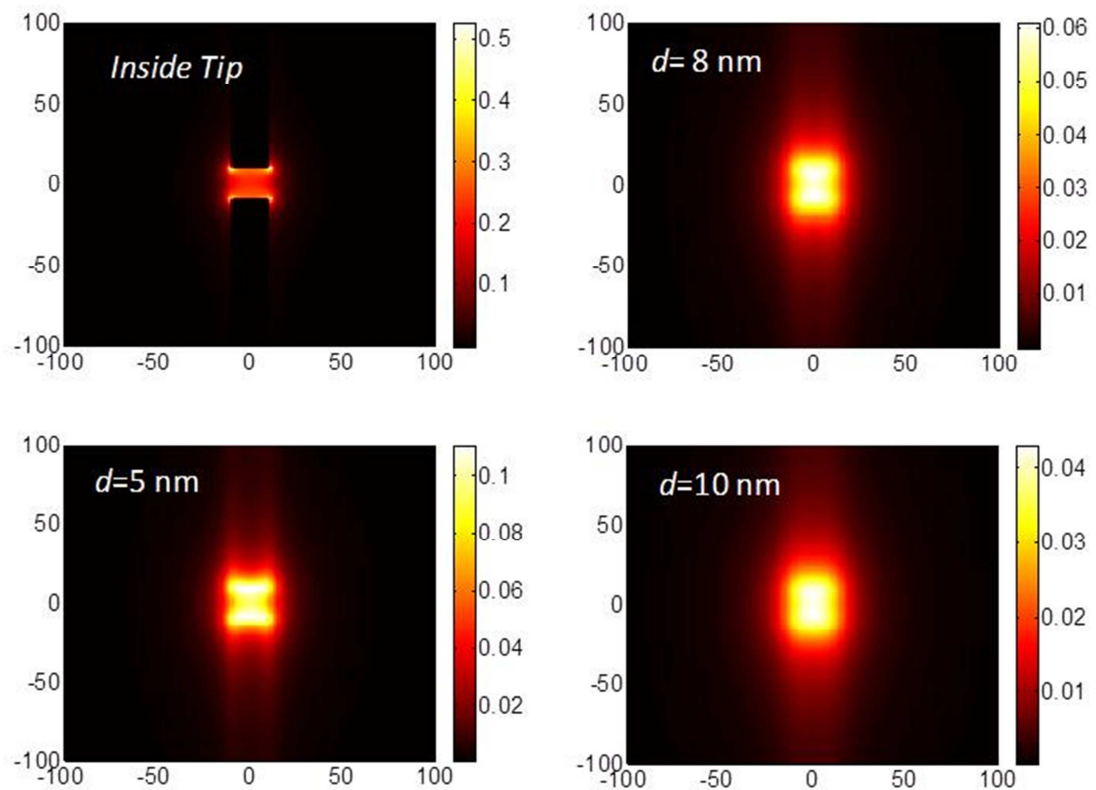


**Figure 3.10** E-Field intensity at different locations along the propagation direction inside (top left) or out of the tip. The colorbar is normalized to the maximum E-field found in the 3-D simulation region.

Figure 3.10 shows the near-field intensity profile at different locations along the propagation direction, showing the divergence of beam in the vicinity of the tip. Figure 3.11 shows that at 10 nm away from the tip (bottom right of Figure 3.10) using air as the free space medium, the near-field radiation is still confined in 50 nm by 50 nm spot, which might be further optimized by using different overcoating materials out of the tip [103].

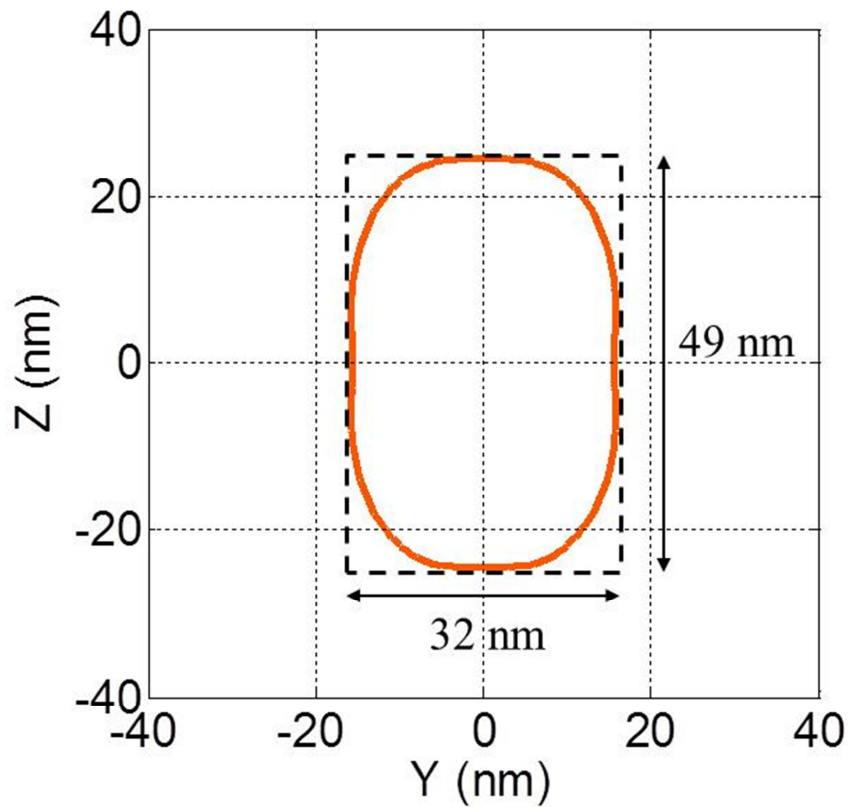


**Figure 3.11** Contour plot to show the FWHM profile (*E*-Intensity) at 10 nm away from the tip.

### 3.4 Conclusions

We have proposed a novel plasmonic device that can effectively convert photonic mode into plasmonic mode. Two-directionally modal size reduction from 232 nm by 156

nm to 24 nm by 21 nm is achieved with high efficiency. A key feature of our device is that it is a planar structure and can be fabricated with standard semiconductor techniques. The patterns of the dielectric waveguide and plasmonic taper can be defined by electron-beam lithography and dry etch. The three-layer MIM plasmonic taper can be formed following a layer-by-layer deposition. A bilayer resist process needs to be applied to easily lift off the deposited materials on photoresist. If similar approach can be applied to visible light regime, the design can be a first step to finally achieve a light spot of 10 nm by 10 nm. In the future, a nano-optic beam may take over part of the work currently done by expensive electron-beam lithography. This technique may also find a large variety of applications in ultrafast modulation, optical data storage, and nano-particle manipulation. The experimental demonstration of this design will be introduced in the next chapter.

---

## 4 INTEGRATED 3-DIMENSIONAL PLASMONIC MODE TRANSFORMATION

---

In this chapter, I will describe the experimental demonstration of a compact platform to convert near-infrared signals between nanoplasmonic and nanophotonic domains. In particular, we utilize a pair of adiabatic nanoplasmonic tapers to assist direct-coupling and shrink the plasmonic guiding area to deep-subwavelength scale as small as 50-nm-by-80-nm with a propagation loss of 2.28 dB/ $\mu$ m. The integrated plasmonic devices developed on a silicon-on-insulator (SOI) substrate could build up a solid platform for plasmonic gauges of ultra-fast communications and optical sensing [135].

### 4.1 Introduction

To exploit the attractive features of subwavelength plasmonics for fast communications, sensing and imaging [136], efficient coupling and excitation methods to convert optical power to plasmon waves have been extensively explored [46], [98]-[106]. Other than the conventional momentum matching technique such as prism coupling [98] or grating coupling [99], the direct coupling or butt-coupling scheme [137] has proved to be both compact and in general broadband. To take the advantage of seamless integration and broadband excitation, metal-insulator-metal (MIM) slot waveguides [53], [100], dielectric-loaded surface plasmon polariton (DLSPP) waveguides [138]-[140], or hybrid plasmonic waveguides [54], [141] have been utilized as the carrier of plasmonic waves. MIM waveguides have the virtue of ultra-small, strictly-confined mode size and acceptable propagation loss, plus the metal layers provide a feasible interface for

contacting formation and novel electrical pumping channels. More importantly, numerical simulations have predicted up to 70% coupling efficiency [64] when 1550-nm light is coupled from a 300-nm wide 2-D silicon waveguide into a 50-nm silver-air-silver MIM waveguide. Prior efforts have been reported to demonstrate the direct coupling scheme using slot plasmonic waveguides through either focused ion beam (FIB) [106], [142] or lift-off process [93], while conventionally the MIM slots are vertically orientated and therefore difficult to engineer their depths to achieve further plasmonic mode transformation [97] especially in the vertical direction. Moreover, the existence of multimode propagation [116] can significantly decrease the surface plasmon's propagation length and increase the complexity of mode analysis. Recently, a plasmonic taper-pair used as input/output ports have been demonstrated on glass [143] to achieve 3-dimensional (3-D) plasmonic confinement, but its glass substrate has critical limitations due to its incompatibility with the SOI technology widely used for on-chip optical communications.

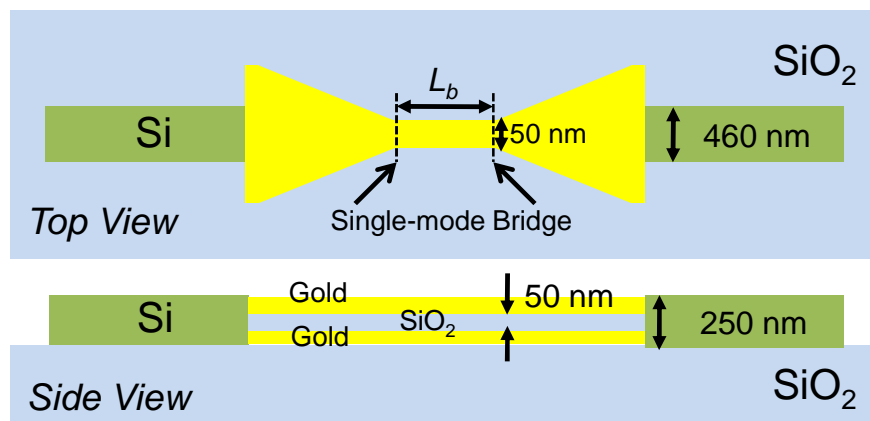


**Figure 4.1** The sketch of an integrated mode transformer including paired tapers and a 3-D nanoplasmonic waveguide as “bridge”.

## 4.2 Design and Modeling

### 4.2.1 Direct coupling for MIM waveguide

The finest guiding structure in our design is the MIM plasmonic waveguide. To fully exploit the efficient direct coupling scheme and take the advantage of the deep subwavelength mode confinement, we design a multilayered MIM plasmonic waveguide between silicon bus waveguides. Direct coupling has been shown to work tremendously well with MIM type waveguide. For comparison, we have modeled another direct coupling case when TM-like single mode impinges on a nanowire consisting of uniform gold with no dielectric layer in between as shown in Figure 4.2(a). Since the momentum matching condition for this type of waveguide is far more difficult to meet, the excitation of surface waves around the metallic nanowire is very inefficient. It is probable to achieve coupling by optimizing the dimension of the nanowire, which will lead to very challenging dimension control and perhaps much lower repeatability. This in turn greatly hampers the advantage of direct coupling, which is supposed to have good tolerance from fabrication disorder. On the other hand, a dielectric layer with deep subwavelength thickness (40 nm) can be buried to form a MIM waveguides as shown in Figure 4.2(b). It clearly shows that by forming a MIM waveguide, the direct coupling condition can be easily met.

In our design, the finest dimension in *both* transverse directions is below 100 nm. Therefore, we refer to our design as “3-D nanoplasmonic devices” opposed to conventional 2-dimensional (2-D) nanoplasmonic devices with confinement below 100 nm only in one direction. In Figure 4.1, the tri-layer thin films consist of a 50-nm silicon dioxide core squeezed between two 80-nm gold claddings. Silicon waveguides are bridged by a pair of taper-shaped plasmonic modules in end-fire fashion, which will

facilitate the direct coupling as well as plasmonic focusing. The theoretical optimization process for the nanoplasmonic taper has been introduced in [119].

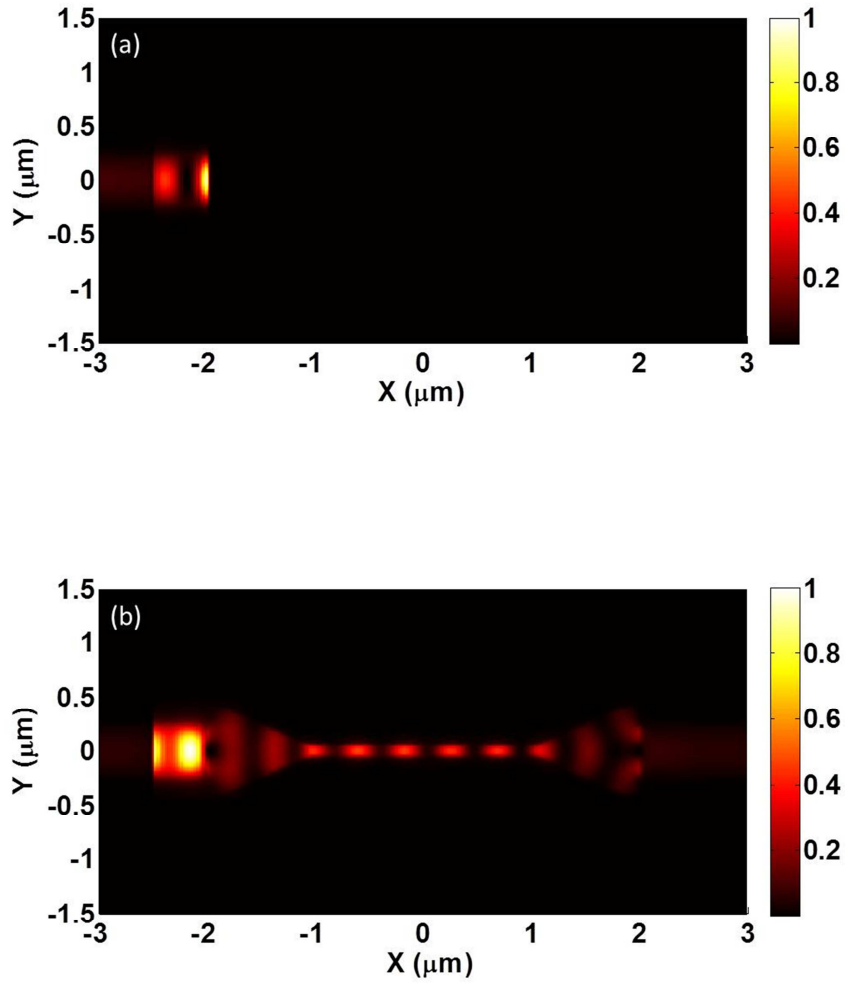


**Figure 4.2** H-Intensity showing the coupling process between silicon waveguides to (a) a gold nanowire taper-pair and (b) MIM plasmonic waveguide taper-pair. Efficient direct coupling can be seen in (b).

Figure 4.3 plots  $H$ -field for taper-assisted mode transformer (Figure 4.3(a)) and multimode coupler (Figure 4.3(b)) respectively. The width of the multimode MIM waveguide shown in Figure 4.3(b) is  $20\ \mu\text{m}$ . Cross-section views of field distribution are

included as insets, showing single-mode and multimode-propagation and the coupling process. In both structures, the total lengths of plasmonic portion are  $4\ \mu\text{m}$  long and butt-connected to silicon waveguides. In Figure 4.3(a), the adiabatic mode transformation eliminates multimode propagation, achieves obvious field enhancement in bridge area and features larger throughput compared to Figure 4.3(b).

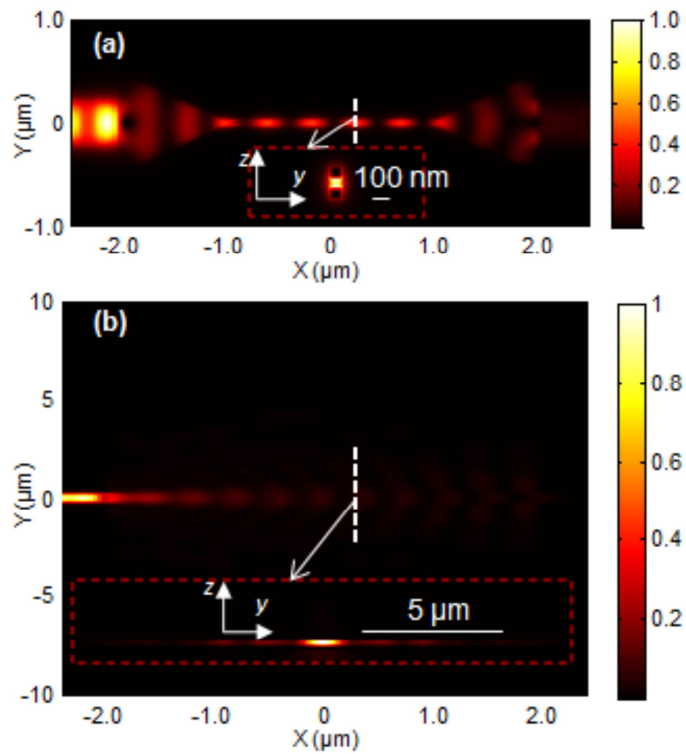


**Figure 4.3** FDTD simulation results ( $H$ -field) for light propagation in (a) taper-assisted mode transformer and (b) multimode MIM waveguides. Insets show the cross-section view of  $H$  intensity.

#### 4.2.2 Practical interface for direct coupling

It is not straightforward to expand the theoretical modeling to a manageable processing approach. The major challenge is to maintain a clear direct coupling interface between the silicon and plasmonic waveguides. In the ideal case, these two types of waveguides are butt-connected to each other, leaving no space in between. Realistically,

it is very difficult to achieve this feat because the risk from gold blocking the silicon output. One option is to leave a reasonable recession or a gap between the two, large enough to avoid the light blocking and at the same time small enough to retain the mechanism of direct coupling, as simulated in Figure 4.4.

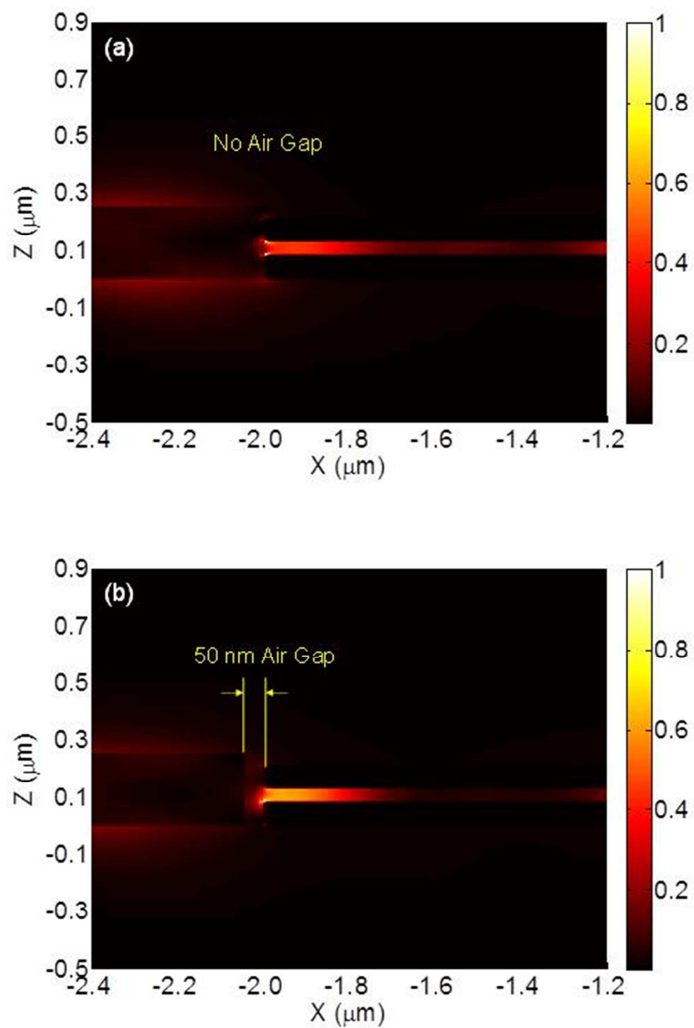


**Figure 4.4** E Intensity for the direct coupling interface consisting of (a) no air gap and (b) 50 nm air gap.

Figure 4.4 shows the 3-D FDTD modeling for the comparison described above, addressing the possibility of leaving a narrow recession between the two types of

waveguide. Comparing with the ideal case in Figure 4.4(a), the scattering from additional discontinuity is clearly visible in Figure 4.4(b). By measuring the averaged power propagated in plasmonic waveguide (output), we have predicted an additional (15%) loss from this modified direct coupling but also verified the legitimacy of this slight revision. The short gap can conserve the mode profile of the TM-like beam transmitting out of the silicon waveguide, and transmit a large proportion of power into the MIM slot waveguide. It is possible that by filling the gap with a matching material, the unwanted scattering can be further decreased.

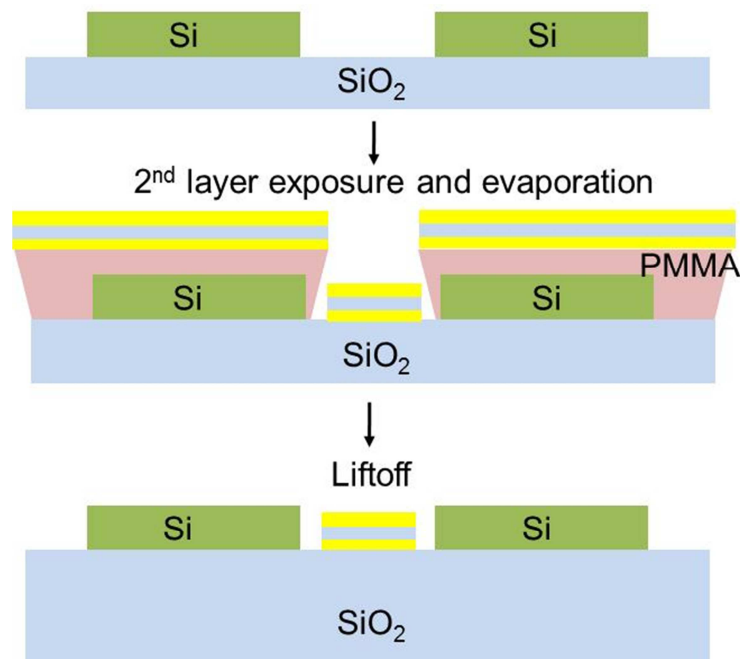


**Figure 4.5** Fabrication steps combining two-stepped electron beam lithography and lift-off.

### 4.3 Fabrication Details

#### 4.3.1 Sample preparation overview

To demonstrate the designed structure, we have designed a two-stepped process based on SOI platform (with 250-nm silicon) to integrate silicon waveguides with

plasmonic devices without using focused ion beam (Figure 4.5). First, electron-beam lithography (EBL) and inductively coupled plasma (ICP) etch are used to define a number of 460-nm-wide single mode silicon waveguides working for 1550-nm light. Several waveguides are designed to include a gap (from 5- $\mu\text{m}$  to 10- $\mu\text{m}$  long as they will contain plasmonic components with different total lengths) for the installation of plasmonic devices using bi-layer PMMA lift-off. After development in Methyl isobutyl ketone (MIBK) and 2-propanol (IPA), the well-defined “windows” on bi-layer PMMA are opened right on top of the air gaps, where evaporated multilayered metal-insulator-metal (gold for 80-nm each and silicon dioxide for 50-nm) are then deposited down to the gap on substrate (buried oxide) with sufficient titanium for better adhesion, followed by lift-off using a mixture of methylene chloride (DCM) and acetone. The alignment tolerance of the two-step processing is below 100 nm and has to be achieved via pre-etched alignment marks at least 1.5- $\mu\text{m}$  deep into the buried oxide layer made by EBL and ICP etch. As it is important to avoid light blocking from metal that might attach to the output interface of silicon waveguides, the designed plasmonic parts should have adequate recession from the waveguide edges.

#### **4.3.2 Fabrication flow**

(1) Prepare a 6-inch silicon-on-insulator wafer. The device layer (silicon) used in the experiment is 300-nm thick. Use the standard RCA clean process to clean the wafer surface.

(2) To obtain the designed device thickness of 250nm, furnace treatment (dry oxidation) is required to thin the device layer. We have calculated the required thickness

and the time needed based on the oxidation curve. An online calculation can be done at <http://www.cleanroom.byu.edu/OxideThickCalc.phtml>.

(3) Dip the wafer into a diluted HF tank such as Buffered Oxide Etch (BOE) to etch the top oxide cladding grown inside furnace. A 5-pt measurement is recommended afterwards to make sure the conformity of the silicon layer and the thickness of the device meet the requirement.

(4) Cleave the 6-inch wafer into 1 inch square small piece (approximately). The size of the piece should be chosen according to the dimension of the piece holder of the EBL system.

(5) Sit the small SOI piece on 120C hotplate for 3 min to dehydrate the surface.

(6) Spin-coat two layer PMMA 495 on top at 1200 rpm for a targeted 1500 nm each. Bake at 170C for at least 15 minutes for each layer.

(7) Pattern the alignment marks (JEOL 9300) at an averaged dose of 1800 mJ/cm<sup>2</sup>. The alignment marks consist of two global marks and several chip marks for multi-layer alignment. The alignment mark is a 'cross' shape covering approximately 2mm by 2mm. The chip mark is a smaller 'cross' shape. The line width of the alignment mark is 3 μm.

(8) Develop in MIBK and IPA mixture (1:3) for about 90 sec. Rinse with IPA and blow dry with nitrogen.

(9) Etch the alignment mark through in CHF<sub>3</sub>/O<sub>2</sub> with Oxford 100 for 10-15 min. Etch rate is about 150 nm/min.

(10) Dip the sample into 1:1 mixture of Methylene Chloride and Acetone for at least 2 hours to strip the bi-layer PMMA. Rinse in IPA and use nitrogen to blow the piece dry.

(11) Spin-coat HSQ negative resist (XR-1541, 2%) at 3000 rpm for 60 sec for a targeted thickness of 100 nm. Bake the sample at 170C hotplate for 120 seconds.

(12) Pattern the silicon waveguides (JEOL 9300) at an averaged dose of 1200 mJ/cm<sup>2</sup>.

(13) Develop in MIF 300 for 3 min.

(14) Use PT770 left chamber (Silicon ICP etch) to etch the silicon with slight over-etch.

(15) Dip in diluted HF to remove the HSQ.

(16) Spin-coat PMMA 495 (8%) at 2000 rpm for a targeted thickness of 700 nm. This is followed by coating PMMA 950 (2%) at 2000 rpm for 100 nm. Bake for at least 15 min for each layer.

(15) Pattern the metal area (JEOL 9300) at an averaged dose of 1200 mJ/cm<sup>2</sup>.

(16) Develop in MIF 300 for 3 min.

(17) Descum in Oxford 81 with Argon etch for 3-5 seconds.

(18) Use ebeam-evaporation to deposit 80 nm gold, 40 nm SiO<sub>2</sub> and 80 nm gold.

(16) Lift-off in 1:1 mixture of Methylene Chloride and Acetone for at least 2 hours to strip the bi-layer PMMA. Rinse in IPA and blow dry with nitrogen. Apply moderate ultrasonic if necessary.

(17) Spin-coat Shipley 1813 and bake at 90C to protect the device.

(18) Dice the piece with a dicing saw, polish the waveguides' input facet and strip the photoresist on top.

#### 4.3.3 Sample screening

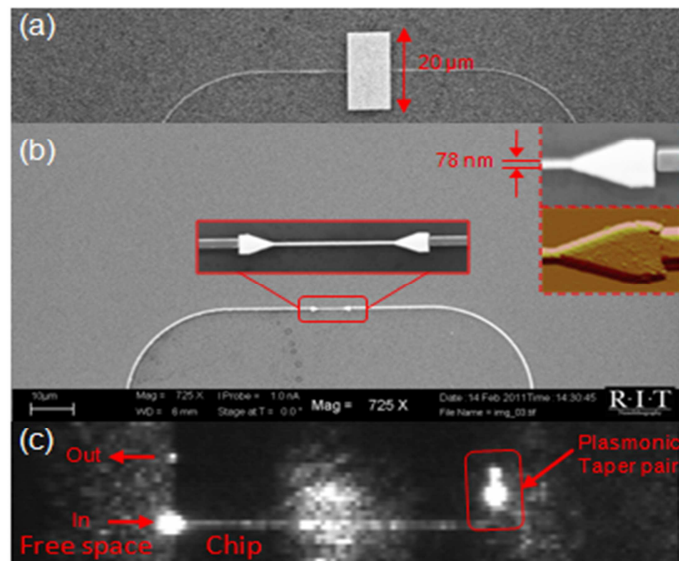


**Figure 4.6** SEM and AFM images of (a) multimode plasmonic coupler and (b) taper-assisted mode transformer. (c) near-infrared light coupled in and out of the plasmonic mode transformer (rotated 90° clockwise along screen normal direction with respect to (b)).

The fabricated multimode coupler (Figure 4.6(a)) and mode transformer (Figure 4.6(b)) are shown in Figure 4.6. The air gap to avoid light blocking is clearly visible (upper inset of Figure 4.6 (b)). The designed air gap is 50 nm and the measured value is between 40 nm and 60 nm, showing satisfactory alignment achieved. One possible approach to further improve the coupling efficiency is to fill the airgap with higher index material such as PMMA ( $n=1.49$ ) [142]. The AFM measurement (lower inset of Figure 4.6 (b)) estimates the bridge width to be 78 nm, larger than the designed value but still resides in the deep-subwavelength scale. Figure 4.6(c) shows the propagation of near-

infrared light through the integrated mode transformer (Figure 4.6(b)), verifying the fabricated platform as a reliable approach for integration of both 2-D and 3-D nanoplasmonic devices.

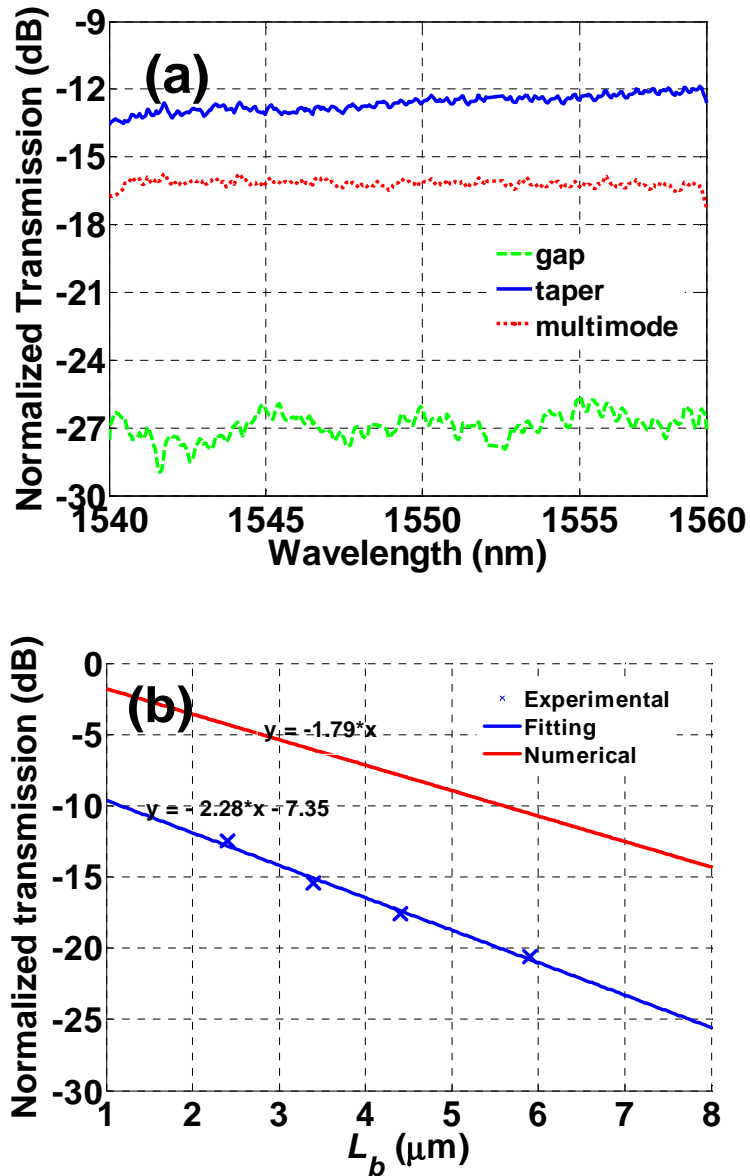


Figure 4.7 (a) The measured transmission spectrum for a taper-assisted coupler (blue), the taperless/multimode coupler (red) and an air gap with no plasmonic component (green). (b) Theoretical (red) and experimental (blue) results of propagation loss for the single mode plasmonic waveguide in bridge area.

#### 4.4 Characterization and Discussion

To characterize the coupling efficiency and spectrum response of the fabricated mode transformers, we use a tunable near-infrared laser to scan the wavelength from 1520 nm to 1620 nm, along with programmed Labview routines to record the corresponding output power. A linear polarizer is applied to ensure the propagation of a Transverse Magnetic (TM) mode ( $H$ -field in plane) for silicon waveguides. We have found that for our plasmonic structures, the throughput from Transverse Electric (TE) source is barely detectable. The samples to be measured can be divided into 3 groups. Firstly, there are silicon waveguides with no gap or plasmonic devices in between. The output power of these waveguides is taken as the reference value for all the normalization afterwards. The second group is the 20- $\mu\text{m}$  wide multimode couplers in the shape of Figure 4.6(a). We have fabricated several multimode couplers with the total length varied from 4.8  $\mu\text{m}$  to 9.6  $\mu\text{m}$ , and these lengths match pair to pair with mode transformers in the shape of Figure 4.6(b), which form the third group. We have also left several bare “broken” silicon waveguide (gap distance = 5  $\mu\text{m}$ ) as reference.

A detailed spectrum response from 1540 nm to 1560 nm for all groups of devices is shown in Figure 4.7(a). Compared with multimode MIM waveguides of uniform width, the taper-assisted mode transformer with exact total length gives significantly less loss in the whole band as much as 3 dB because of the beam shaping and the elimination of multimode propagation [116]. The propagation loss of the “bridge” waveguide (50-nm-wide single mode plasmonic waveguide) between the paired tapers have been estimated with a number of measurements with different bridge lengths (Figure 4.7(b)), and a fitted propagation loss of about 2.28 dB/ $\mu\text{m}$  (or a propagation length of 1.3  $\mu\text{m}$ ), which is

higher than the numerical results for  $1.79 \text{ dB}/\mu\text{m}$ . Fabrication disorders or external dust might have contributed to the higher loss reported here. The averaged loss from one taper-pair is calculated as  $7.35 \text{ dB}$  in total (Figure 4.7(b)). Note that this value also includes propagation loss of plasmon wave inside the taper-pair, and the actual coupling efficiency from a photon-plasmon facet shall be larger than  $-3.68 \text{ dB}$  (or  $42.9\%$ ) based on  $7.35 \text{ dB}$  total loss.

#### **4.5 Conclusions**

We design, fabricate and characterize integrated plasmonic devices for photon-plasmon conversion and plasmonic mode transformation. We manage to demonstrate a coupling device from photon to surface plasmon and then back to photon with  $7.35 \text{ dB}$  conversion loss. In addition, the fabricated coupler has successfully focused multimode plasmonic propagation to deep subwavelength ( $80 \text{ nm}$  by  $50 \text{ nm}$ ) single mode propagation with  $2.28 \text{ dB}/\mu\text{m}$  propagation loss. The demonstration leads to a versatile and robust platform for integration of 3-D nanoplasmonic devices onto SOI platforms, and is functional for further exploration of optical or electrical modulation, compact sensing and detecting solutions. Related future work will be discussed in Chapter 7.

---

## 5 SPOOF PLASMONICS IN COATED METALLIC GRATINGS

---

In this chapter, we design integrated waveguides for terahertz (THz) and mid-infrared (MIR) applications on wafer platform. Based on the prototype of spoof plasmonic waveguides consisting of textured metallic surface, we explore the possibility of coating periodic metallic pattern with silicon (at 0.6 THz) or germanium (at MIR region of 30 THz) to further shrink the relative mode size of propagation spoof plasmonic waves. Numerical modeling via 3-D finite-difference time-domain (FDTD) has shown deep sub-wavelength mode confinement in transverse directions to smaller than  $\lambda/50$  by  $\lambda/50$ , with an estimated propagation loss of less than 0.1 dB for each repetitive unit [144].

### 5.1 Introduction

With the development of terahertz (THz) technology, multiple applications in the THz regime such as detecting, imaging, communications and spectroscopy [145]-[147] have been explored. The fast progress of this field has highlighted the requirement of a reliable platform for compact and complete THz wave circuitry, which would preferably enable flexible design and robust fabrication and packaging. Along with the long-term challenge of integrating efficient THz sources into THz systems, there has also been a crucial demand of novel waveguiding scheme that guarantees low-loss and confined propagation, without sacrificing easy manufacturing and integration. Conventional dielectric waveguides working for the optical or microwave regime suffer from the diffraction limit and therefore fail to achieve deep-subwavelength mode profile when

their sizes are scaled into the THz regime. Therefore, optical fibers [148], planar dielectric or polymer strips [149], and metallic waveguides [150] are all excluded from building up the preferred guiding platform due to their diffraction limit. There has also been effort to construct THz waveguides with novel designs, such as metal wire waveguides [151], [152], photonic crystal fiber waveguides [153]-[155], silicide plasmonic waveguides [156], low-index discontinuity waveguide [157] and parallel plate waveguide [158], [159]. However, they either lack deep subwavelength confinement in both transverse directions, or need stand-alone platform that could hardly be monolithically integrated with other devices.

Recently, the concept of surface waves engaging grouped free electron oscillation is known through the study of plasmonics. Several plasmonic waveguides have been reported to achieve deep subwavelength mode profile in transverse cross-section in favor of integration [97]. In light of this approach, there have been endeavors to design metamaterials based on ideal or low-loss metal to mimic the behavior of surface plasmon polaritons (SPPs) [68], [69] in the THz regime, and sometimes bear the name of “spoof plasmonics”. This family of metamaterial generally consists of well-designed surface corrugations that engineer the dispersion of surface waves and confine the power close to the surface of waveguide. They extend previous study of 2-D case for periodic metal gratings that can guide electromagnetic waves on surfaces [160]. Many interesting discoveries have been made based on periodic and semi-periodic corrugations on metal surface, from theoretical analysis [161] to numerical study [162]. Previous study has revealed the possibility of designing and demonstrating a versatile THz waveguide platform with subwavelength confinement, on which various passive functional devices

such as splitters, directional couplers and ring resonators [70] can be integrated. In this chapter, we propose a practical design originating from metamaterials with metallic corrugation based on the silicon platform. The silicon background, as we will further emphasize, will not only facilitate the fabrication process, provide robust substrate, avoid the high absorption by moisture in the air, but also strengthen the ability of the metamaterial to achieve deep subwavelength mode size. The same approach is then applied specifically to the MIR region (wavelength from  $8 \mu\text{m}$  to  $15 \mu\text{m}$ ), with the background material changed from silicon to germanium.

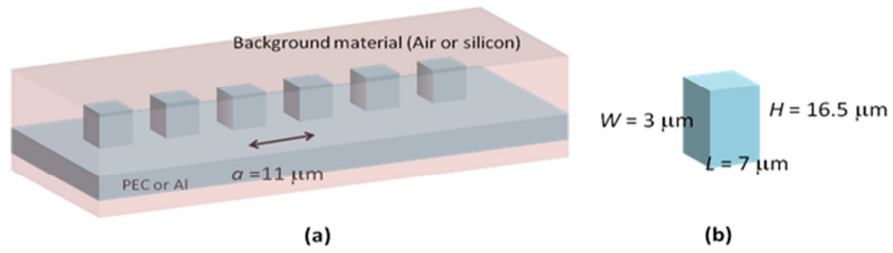


**Figure 5.1** Schematic view of the spoof plasmonic waveguide for THz region. (a) 3-D scheme of the waveguide for THz region. (b) The physical dimension of each metal post for THz region.

## 5.2 Dispersion Calculation

### 5.2.1 Structure definition

The structure we present consists of periodic surface corrugation of low-loss metal (Figure 5.1(a)). Note that in this section, the scheme, calculation and discussion are provided under the context of the THz regime, while the mode size result for MIR is given at the end of Section 5.3. The metal ‘posts’ (Figure 5.1 (b)) are  $7 \mu\text{m}$  long and  $4 \mu\text{m}$  apart from each other, making the lattice constant  $11 \mu\text{m}$ . Each post is  $3 \mu\text{m}$  wide and  $16.5 \mu\text{m}$  high. This prototype has been theoretically studied [161], [70] and the dispersion nature is well known, especially the first TM band, which is similar to that of SPPs. It has

also been suggested that the dispersion diagram does not change considerably when lossless metal (PEC) is replaced with low-loss metal [162], and our simulations have verified this conclusion. We have used a complex dielectric constant from [164] for aluminum in THz range for calculation.

In Figure 5.2, we plot the first bands of supported modes for silicon and air background respectively. The green solid circles denote the dispersion of the lattice when the background index is 1.0, while the red circles describe the dispersion when the background index is 3.4. Here, the cut-off frequency of the first band (TM) is lowered from 3.22 THz to 0.95 THz when the high-index background is used. A rigorous solution of the dispersion relation for PEC comes from Eq. (8) of [21], which leads to

$$\tan(k_b H) \sum_{n=-\infty}^{\infty} S_n^2 \frac{k_b}{\sqrt{\beta_n^2 - k_b^2}} = 1 \quad (5.1)$$

where  $\beta_n = \beta + \frac{2n\pi}{a}$ ,  $S_n = \sqrt{\frac{a-L}{a}} \beta_n (a-L) / 2$  and  $k_b = n_b k_0$ . This approach can be further approximated to a generalized version of Eq. (14) of [161] for deep subwavelength surface texture ( $\lambda \gg H$  and  $L$ ) as in Eq. (5.2), when the wave vector inside background material is  $k_b = n_b k_0$  instead of  $k_0$ . In Eq. (5.2), because of the existence of a larger  $k_b$  (compared to  $k_0$ ), the dispersion curve will behave progressively in a similar trend yet bend more radically away from lightline. In this sense, the working frequency can be modified by using different background material, even if surface corrugations of same physical dimension are applied. When a high-index background is in use, the surface corrugation can guide waves with larger wavelength, and therefore

achieve smaller relative mode size in terms of vacuum wavelength. This assumption needs further verifications through 3-D modeling, which can be found in the next section.

$$k = k_b \sqrt{1 + \left(\frac{a-L}{L}\right)^2 \tan^2(k_b H)} \quad (5.2)$$

### 5.2.2 Calculation detail

From the eigenmode calculation, the quality factor ( $Q$ -factor) of a lattice can be used to evaluate the propagation loss when a waveguide is formed from linking multiple lattices together. The loss per unit distance of a waveguide is proportional to the ratio of energy loss rate of the cavity and the group velocity of the wave, so it is expected that at the first band edge the tremendously slowed-down light will have too high loss for practical applications [162]. To achieve an acceptable propagation length for waveguide design, the working frequency should be chosen properly, avoiding the band edge.

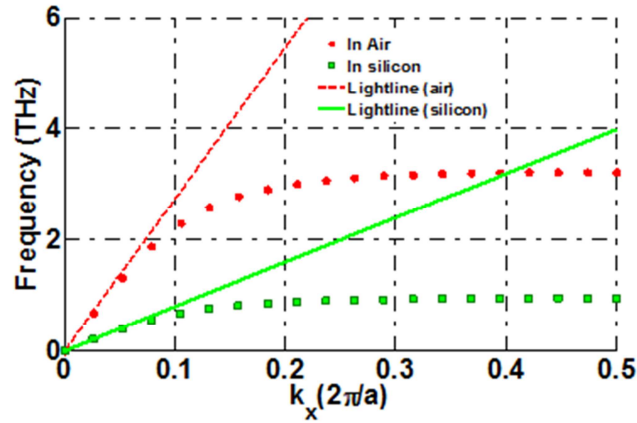


**Figure 5.2** Dispersion relation for the identical metal unit in air (red, dotted) and in silicon (green, square).

In order to get the  $Q$  factor of a coupled cavity in FDTD modeling, a special technique with broadband source, instead of a continuous wave source (CW), should be

used. All the simulation results in this part are produced by FDTD Solutions by Lumerical Inc. [92]. The technique involves the transient simulation of a short pulse covering a wide band and the response after the source field is turned off. If there is a resonance inside the cavity, the resonant frequency can be obtained by performing Fourier transform of the time-domain field value. This is illustrated in Figure 5.3, when the simulation region is bounded by perfect matching layers (PMLs) and periodic boundaries. The arrows denote the randomly placed sources and the crosses denote the detectors. The field values captured by these point detectors will be averaged and sliced to exclude the source radiation. A Fourier transform will give the resonant peak  $f_r$  with a bandwidth  $\Delta f$  in frequency-domain and the  $Q$  value can be calculated using the definition  $Q = f_r / \Delta f$ .

Specific directions regarding implementing this technique for cavity modeling in Lumerical's FDTD software can be found at [163].

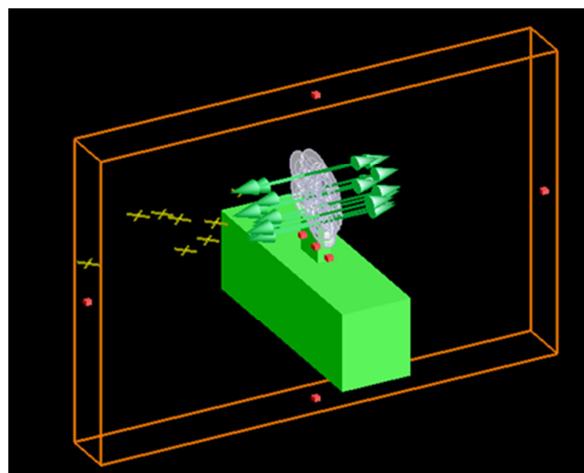


**Figure 5.3** An illustration of the setup for the FDTD simulations used for  $Q$  calculation. The arrows denote the sources and crosses denote the detectors.

Same type of calculation can also be applied to designer surface plasmons with even lower frequency to GHz range [71]. The band diagram has been proved to match with experimental results well (Figure 5.4) and very useful for predicting the working frequency for the experiment.

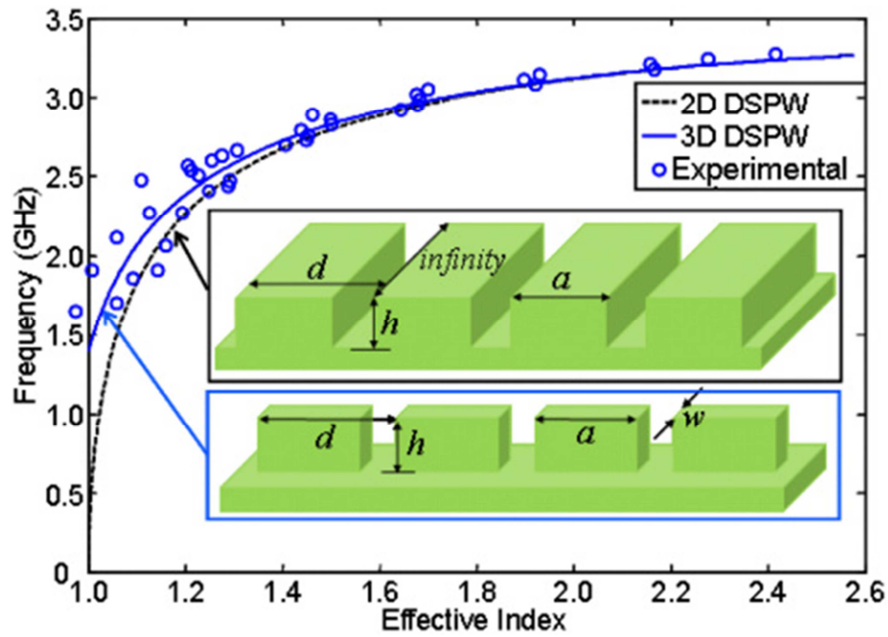


**Figure 5.4** Dispersion diagram of Designer Surface Plasmon waveguide in GHz spectrum. Adopted from [71].

### 5.3 Mode Profile and Propagation Loss

With the dispersion diagram calculated, we perform a 3-D modeling for a spoof plasmonic waveguide consisting of periodic unit cell described above. We study the propagation of waves at the frequency of 0.6 THz, which is significantly away from the band edge. From the plots of the cross section view at the center between two neighbored metal dents (Figure 5.5(a)) and at the center of a metal post (Figure 5.5(b)), we have verified that most power is confined to the top region of metal posts, while the lateral spread of electric field in transverse direction will remain deep subwavelength scale.

Figure 5.5(b) shows that the maximum field is found at the wedges, and the mode size (calculated by the half-maximum field contour) is confined in a  $1.8\mu\text{m}$ -by- $5\mu\text{m}$  rectangular area, which is on  $\lambda/277$  - by -  $\lambda/100$  level. Even inside the airgap, the half-maximum beam size (normalized to the maximum value at the airgap) is  $9\mu\text{m}$ -by- $10\mu\text{m}$  ( $\lambda/56$ -by-  $\lambda/50$ ) and still resides in  $\lambda/50$  level.

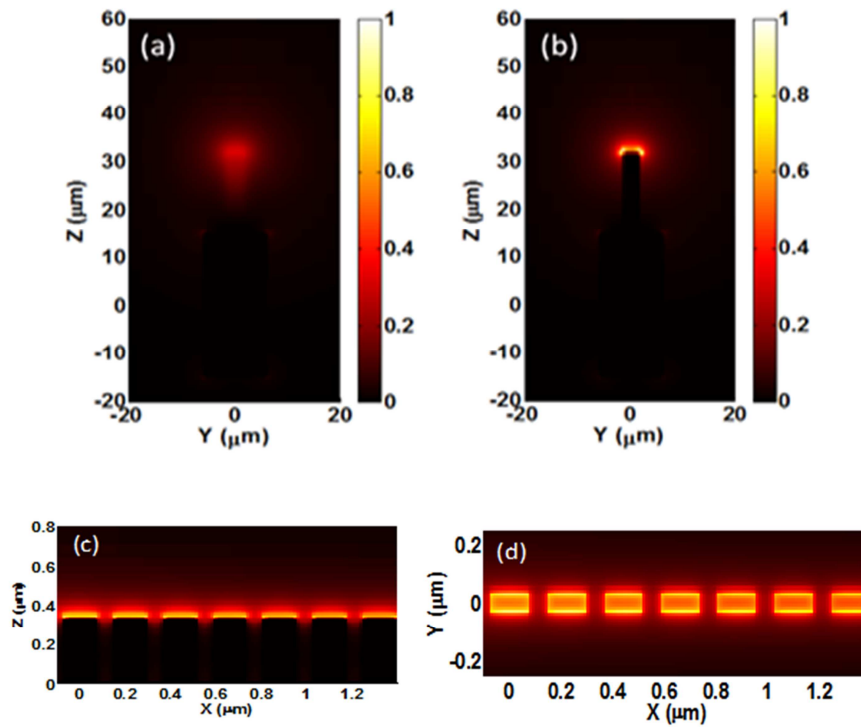


**Figure 5.5** Field or power of different views at 0.6 THz and 30 THz. Cross-section view of electric field intensity  $|E|^2$  at (a) air space between two metal posts and (b) a metal post, both at 0.6 THz. (c) Side view of power density  $\text{real}(P_x)$  in the symmetry plane and (d) top view of power density  $\text{real}(P_x)$  at  $0.01\mu\text{m}$  above the top surface of metal posts, both at 30 THz.

Figure 5.5 (c) and (d) give the side- and top-view of the MIR wave propagating near the metal surface at 30 THz, which can also help to appreciate the power distribution of the previous 0.6 THz case. The power loss from absorption and radiation can be estimated with the  $Q$  factor calculated in last section. As mentioned above, the working

frequency for Figure 5.5 (a) and (b) is chosen at 0.6 THz, away from the band edge to avoid high loss. From the dispersion curve we calculate that the group velocity at 0.6 THz is  $0.167c$  and  $Q$  value of 300. With  $a = 11 \mu\text{m}$  and from  $loss = \exp(-L\omega/Qv_g)$  (Eq. (4) of [161]), we estimate the loss per period to be  $0.01 \text{ dB}/a$ . This loss level is acceptable for this design to act as the platform of waveguides, power splitters, directional coupler and other devices alike.

When the same approach is applied to MIR region by scaling down the physical dimension of the above structure, the working frequency is shifted from 0.6 THz to 30 THz, or wavelength from  $500 \mu\text{m}$  to  $10 \mu\text{m}$ . The dispersion of the first band gives a cutoff frequency of 50 THz, higher than the working frequency we picked up (30 THz). At this frequency, germanium is preferred ( $n = 4.003$ ) to silicon to act as the background material because of its comparatively lower loss. The mode size from 3-D FDTD calculation is  $0.18\mu\text{m}$ -by- $0.2\mu\text{m}$  ( $\lambda/166$  - by -  $\lambda/100$ ), which resides well inside deep-subwavelength level. The calculated loss per period is  $0.03 \text{ dB}/a$  at 30 THz.

The dispersion diagrams are acquired from a lattice with Bloch boundary condition. As mentioned earlier, the band diagram will not change much compared to using lossless metal which can be simulated with a very small dielectric constant (a negative real number such as  $\epsilon = -10000$ ) in FDTD. The simulation of the whole waveguide is performed using a magnetic dipole source that will excite the quasi-TM surface propagation mode. Non-uniform meshing is configured to resolve sharp corners or material boundary, as well as the skin depth of metal. The finest mesh size of the simulation is  $1/1000$  of vacuum wavelength.

#### 5.4 Proposed fabrication steps

A major advantage regarding the substitution from air to other materials is on its easiness of demonstration. The microstructure of metal can be indirectly defined by firstly etching the dielectric substrate (background material). Since most power delivery happens along the surface of this interface (Figure 5.5), the situation is well approximated by calculations performed previously even if there is no overcoat on metal.

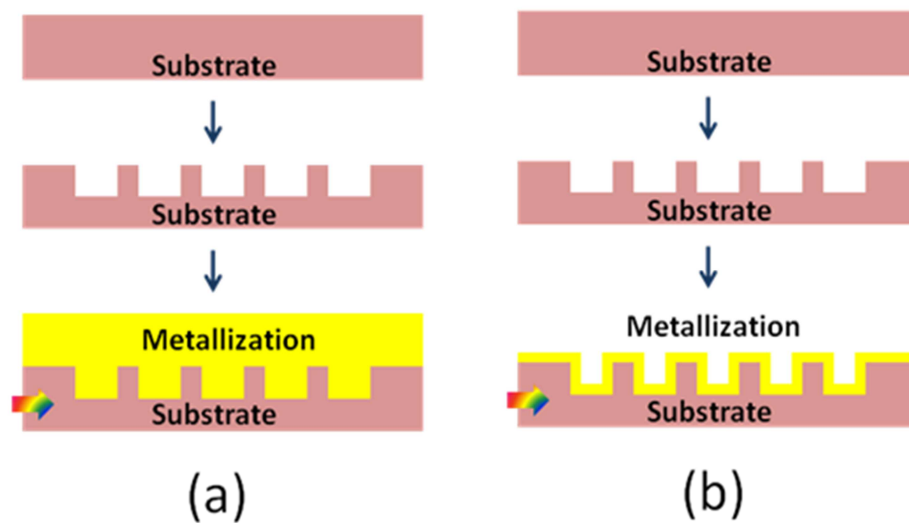


**Figure 5.6** Proposed fabrication steps. (a) Conventional metallization. (b) Sputtering onto sidewalls only.

A schematic fabrication process is shown in Figure 5.6. Starting with a silicon or germanium substrate, it is necessary to do a micro-patterning using micro- or nano-lithography. After pattern-transfer via an etching process, the corrugation on the background material can be again transferred to a thin metal film. A fast deposition of electroplating other than sputtering or evaporation may be preferred to fill the ‘holes’ on dielectric background completely (Figure 5.6(a)). It is also possible to use sputtered metal to coat the side walls of the holes instead of filling them completely (Figure 5.6(b)), in

which case the thickness of deposition should be large enough to exceed the skin depth, which is small at this frequency and easy to obtain. To characterize the waveguide, an excitation can be applied directly near the interface between metal and background.

## **5.5 Conclusions**

We explored the possibility of using different background material with spoof plasmonic waveguides in the THz and MIR regimes, to achieve extremely tiny mode size and to outperform the conventional scheme, which normally surrounds the metamaterial waveguides with air. We have used 3-D FDTD approach to show that the working wavelength of these waveguides can be increased by using high-index background material (silicon or germanium), with the attractive deep subwavelength field confinement being well preserved. We have also suggested a fabrication scheme based on wafer platform that is straightforward and CMOS-compatible. This may help to launch broader applications of spoof plasmonics for spectroscopy, sensing and communications.

---

## 6 MULTILAYERED METAL-INSULATOR STACKS GUIDING SUPER PLASMON WAVES

---

In this chapter, the dispersion of the fundamental super mode confined along the boundary between a multilayer metal-insulator (MMI) stack and a dielectric coating is theoretically analyzed and compared to the dispersion of surface waves on a single metal-insulator (MI) boundary. Based on the classical Kretschmann setup, the MMI system is experimentally tested as an anisotropic material to exhibit plasmonic behavior and a candidate of “metametal” to engineer the preset surface plasmon frequency of conventional metals for optical sensing applications. The conditions to obtain artificial surface plasmon frequency are thoroughly studied, and the tuning of surface plasmon frequency is verified by electromagnetic modeling and experiments. The design rules drawn in this chapter would bring important insights into applications such as optical lithography, nano-sensing and imaging [165].

### 6.1 Introduction

The multilayer metal-insulator (MMI) stack system (also termed as metal-dielectric composite or MDC) has been widely used as an optically-anisotropic composite [166]-[168], utilized for imaging [169]-[173], optical lithography [174] and subwavelength sensing/detecting [175]. One of the most attractive features of this stratified medium is its ability to engineer the dispersion of engaged electromagnetic waves, and to tune the frequency range where interesting optical phenomena could occur. As a fundamental form of 2-D periodic structure, the optical property of MMI stack has

been extensively studied [169]-[182] and both rigorous formalism and approximation approach have been developed. Based on a rigorous transfer-matrix method (TMM) [169], the transmittance and reflectance of any incident beams at any layer can be accurately obtained. The effective medium theory (EMT) [170] [178], on the contrary, has been applied to approximate the macroscopic behavior of the MMI system as a uniform anisotropic material, and offers more control than TMM towards a demand-oriented design procedure, while important corrections related to non-local effect [180], [181] has been made.

As a promising approach towards deep subwavelength optics, plasmonics have attracted great research interests for optical sensing and imaging in recent years. However, plasmonic materials are generally scarce in variety plus the working frequency is limited because of the preset plasma frequency of each plasmonic metal. This problem is worse off in optical frequency, as almost no substitutions (mostly doped semiconductor compounds) can be chosen to replace the overwhelmingly used metals such as aluminum (for DUV), silver and gold (for visible and NIR) due to high loss. It would therefore be significant for optical sensing or imaging applications to explore stratified medium as a plasmonic material or “metametal” and understand how its plasmonic features could be controlled, so as to broaden the frequency window for imaging or sensing applications [167] [175]. As one of the most important prototype for plasmonic sensing, Kretschmann configuration can accurately pick off the surface wave’s resonant point at metal-dielectric half-plane by exciting the fundamental TM surface mode on the boundary [167] [179]. In this chapter, we investigate this surface mode thoroughly and manage to highlight the background (host) material as an important factor, which is rarely noticed in prior art.

Specifically, we outline explicit design rules for shifting surface plasmon frequency to not only lower [175], but also higher, for optical sensing. The results have also been compared with a rigorous transfer-matrix method with great accuracy. We have then experimentally verified the tuning of surface plasmon frequency in optical frequency based on Kretschmann setup. The conclusions would bring important insights into plasmonic applications from optical lithography to nano-sensing and imaging.

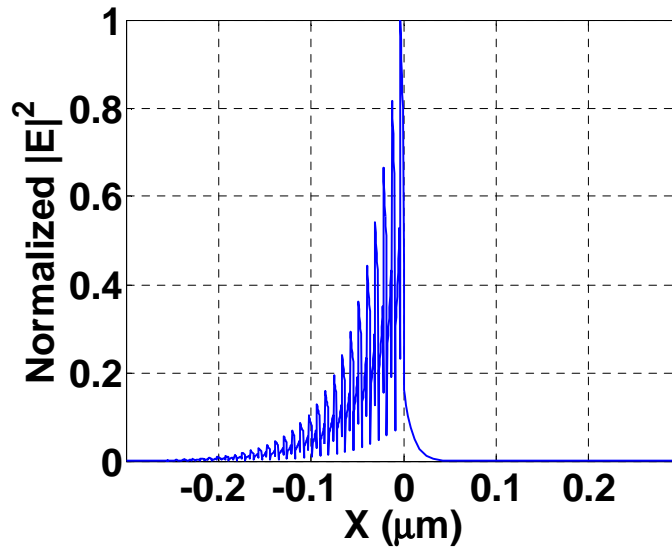


**Figure 6.1** E-field Intensity of a bounded super surface wave hosted by the multilayered metal-dielectric composite at a wavelength of 630 nm.

## 6.2 Theoretical Analysis

### 6.2.1 Bounded surface waves for multilayer

Multilayered metal-insulator stacks have been investigated as waveguides to support various kinds of modes. One of the most important modes with plasmonic nature is the fundamental TM mode, in which the transverse electric fields point across the multilayer. When we designate this mode as plasmonic, we are trying to limit our analysis in those spectra that the metal's real permittivity has the negative sign and the

loss is moderate. A momentum-matching setup can be easily simulated in 2-D FDTD simulations and to further show the mode profile of this fundamental TM mode (Figure 6.1). In this figure, the MMI composite manages to support a confined mode at the boundary between a topcoat and the multilayer, after momentum matching condition is met in a Kretschmann-like setup (Figure 6.2). The maximum of the field locates at the interface and exponentially decay into both directions. This is very much alike to the plasmonic field distribution of a metal-insulator interface. Inside the thin layers, the fields also have local maximum at metal-insulator boundaries. The behavior makes this 2-D problem (especially the case of the fundamental TM mode) attainable for the effective index approach [170].

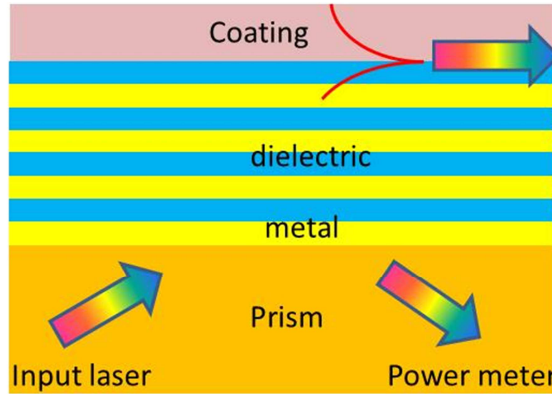


**Figure 6.2** The Kretschman setup used for the excitation of super surface waves on the boundary between MMI and a top coat.

### 6.2.2 Effective index method and effective surface plasmon frequency

Starting from the anisotropy of MMI structure, the effective permittivity tensor is obtained as [169]

$$\varepsilon_x = \varepsilon_z = \frac{\varepsilon_1 + \eta \varepsilon_2}{1 + \eta}, \quad \frac{1}{\varepsilon_y} = \frac{1}{1 + \eta} \left( \frac{1}{\varepsilon_1} + \frac{\eta}{\varepsilon_2} \right), \quad (6.1)$$

where  $\eta$  is the filling ratio of the layer thickness defined by  $\eta = d_2/d_1$ , and the axes are setup in Figure 6.3(a). In the following derivation, we treat  $\epsilon_1$  as the insulator and  $\epsilon_2$  as the metal. Regarded as a single anisotropic medium, it can be placed next to the semi-space of a dielectric material ( $\epsilon_d$ ) and form a boundary as host of surface waves. Assuming a fundamental TM-polarized surface wave (super mode) propagating along this boundary and applying proper boundary conditions, the MMI-insulator boundary supports a propagation surface mode with the dispersion relation obtained as

$$\beta = \frac{\omega}{c} \sqrt{\frac{\epsilon_d(\epsilon_d - \epsilon_x)\epsilon_y}{\epsilon_d^2 - \epsilon_x\epsilon_y}} = \frac{\omega}{c} \sqrt{\frac{(1+\eta)\epsilon_d^2 - \epsilon_d(\epsilon_1 + \eta\epsilon_2)}{\epsilon_d^2(1/\epsilon_1 + \eta/\epsilon_2) - (\epsilon_1 + \eta\epsilon_2)}}. \quad (6.2)$$

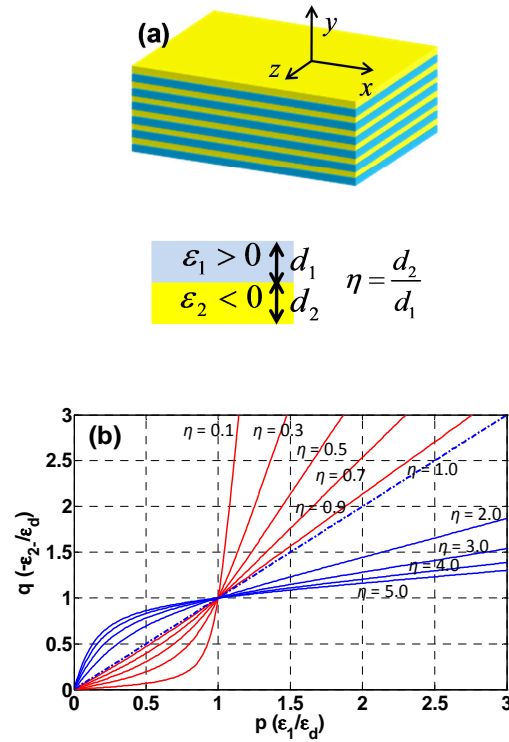


**Figure 6.3** (a) The multilayer metal-insulator (MMI) scheme and definitions of parameters; (b) The  $q$  vs.  $p$  curve used to analyze different conditions for tuning effective surface plasmon frequency with a semi-space dielectrics  $\epsilon_d$ .

To ensure this wave is confined to the boundary, an additional condition is applied as  $\varepsilon_x < 0$ , or

$$\eta > \left| \frac{\varepsilon_1}{\varepsilon_2} \right|. \quad (6.3)$$

When  $\eta$  approaches infinite as the MMI gradually becomes a uniform metal layer, Equation (6.2) can be simplified to

$$\beta = \frac{\omega}{c} \sqrt{\frac{\varepsilon_d \varepsilon_2}{\varepsilon_d + \varepsilon_2}}, \quad (6.4)$$

which is exactly the well-known dispersion relation for a metal-insulator (MI) boundary. When  $\omega$  approaches zero,  $|\varepsilon_2|$  approaches infinite and the dispersion curve overlaps with

$$\beta = \frac{\omega}{c} \sqrt{\varepsilon_d}, \quad (6.5)$$

which is the lightline of the dielectric coating.

The similarity of the dispersion between MMI-insulator and MI-insulator structure revealed in Equations (6.4) and (6.5) gives a possibility to develop a concept of effective surface plasmon frequency (ESPF), especially when MMI is placed inside (or neighbored to) a dielectric semi-space to act just like a uniform metal (metametal). Firstly, we try to derive the value of the ESPF of MMI structure. Similar to the case of MI-insulator, the surface plasmon resonance (SPR) happens at the pole of the  $\beta$ - $\omega$  relation described in Equation (6.2). The poles of Equation (6.2) can be analytically obtained after solving a quadratic equation of  $\varepsilon_2$ . The solution can be expressed by  $\varepsilon_d$ ,  $\varepsilon_1$  and the filling ratio  $\eta$ , as

$$\varepsilon_2 = \frac{\varepsilon_d^2 - \varepsilon_1^2 \pm \sqrt{(\varepsilon_d^2 - \varepsilon_1^2)^2 + 4\eta^2 \varepsilon_1^2 \varepsilon_d^2}}{2\eta \varepsilon_1}, \quad (6.6)$$

while the positive root should be discarded based on the preconditions  $\varepsilon_x < 0$  applied in the related section of Equation (6.3). Based on Equation (6.1), at least one of the two materials in the multilayered medium needs to have negative permittivity to make  $\varepsilon_x < 0$ . The negative root from Equation (6.6) gives the largest dielectric constant the metametal could reach at

$$\varepsilon_2(-) = \frac{\varepsilon_d^2 - \varepsilon_1^2 - \sqrt{(\varepsilon_d^2 - \varepsilon_1^2)^2 + 4\eta^2 \varepsilon_1^2 \varepsilon_d^2}}{2\eta \varepsilon_1}. \quad (6.7)$$

To study the plasmonic property of the metametal, it is convenient to start from the Drude model of the filling metal  $\varepsilon_2 = 1 - \omega_p^2/\omega^2$ , when  $\omega_p$  is the plasmonic frequency of the filling metal. Here a characteristic frequency for the metametal can be defined as equal to ESPF ( $\omega'_{sp}$ ), which yields  $\varepsilon_2(-) \equiv 1 - (\omega_p/\omega'_{sp})^2$ . This is analogy to the definition of surface plasmon frequency defined by  $\varepsilon_2 = -\varepsilon_d \equiv 1 - (\omega_p/\omega_{sp})^2$ , in while  $\varepsilon_d$  describes the dielectric half space. It would be interesting to study the relation between  $\omega_{sp} \equiv \omega_p/\sqrt{1 + \varepsilon_d}$  and  $\omega'_{sp}$  then, as for the latter, there are many parameters that can be controlled even if the same metal is used in the system. Based on the definition above, the relation between  $\omega'_{sp}$  and  $\omega_{sp}$  can be easily appreciated by the ratio of  $\varepsilon_2(-)$  and  $\varepsilon_d$ . For simplicity, we introduced a new term  $p = \varepsilon_1/\varepsilon_d$ , and another term  $q$  for the ratio of  $\varepsilon_2(-)$  and  $-\varepsilon_d$ . From Equation (6.7), the factor  $q$  can be expressed by  $p$  and  $\eta$  as

$$q \equiv \frac{\varepsilon_2(-)}{-\varepsilon_d} = \frac{1 - p^2 - \sqrt{p^4 + 4\eta^2 p^2 - 2p^2 + 1}}{-2\eta p}. \quad (6.8)$$

Figure 6.3 (b) shows how  $q$  varies with different  $\eta$  and  $p$ . Again, the factor  $q$  is a direct indication of the relation between  $\omega_{sp}$  and  $\omega'_{sp}$  since

$$q \equiv \frac{\varepsilon_2(-)}{-\varepsilon_d} \equiv \frac{1 - \omega_p^2 / \omega_{sp}^2}{1 - \omega_p^2 / \omega'_{sp}{}^2}. \quad (6.9)$$

The observation indicates that the ratio  $q$  does change with both  $p$  and  $\eta$  as expected. More importantly,  $q$  can change from less than unity to larger than unity. From Equation (6.9), it is clear that  $\omega'_{sp}$  can also be shifted higher or lower than  $\omega_{sp}$  with different values of  $p$  and  $\eta$ . The limitation shown in Equation (6.3) adds another upper cut-off frequency and this value can be smaller than ESPF when  $\eta$  is smaller than 1, which should also be taken into account while exploiting the tunability of MMI system.

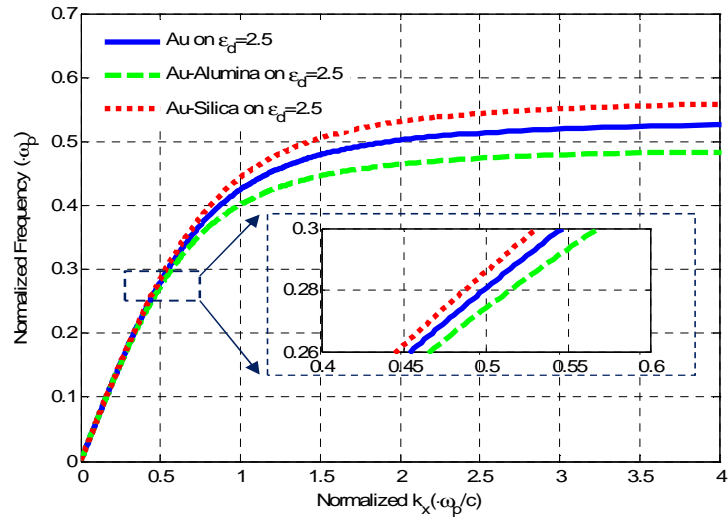
### 6.2.3 Interpretation and numerical verification

When  $p$  is larger than 1 (which means the insulator used in MMI has higher index than the background material),  $q$  is usually larger than 1. From Equation (6.9), the ESPF  $\omega'_{sp}$  will usually be smaller than the conventional surface plasma frequency  $\omega_{sp}$  for all possible filling ratio  $\eta$ . This can usually be understood as a result of smaller electron density because of the existence of dielectric filling. Note that when  $p = 1$ , the ESPF remains the same to conventional surface plasma frequency *regardless of the filling ratio*  $\eta$ . On the other hand, the ESPF  $\omega'_{sp}$  can be shifted higher and even close to  $\omega_p$  when  $\eta$  is small and  $p < 1$ , which means the tuning of surface plasma frequency can theoretically overcome the upper cut-off frequency for any fundamental TM mode supported on a single MI boundary.

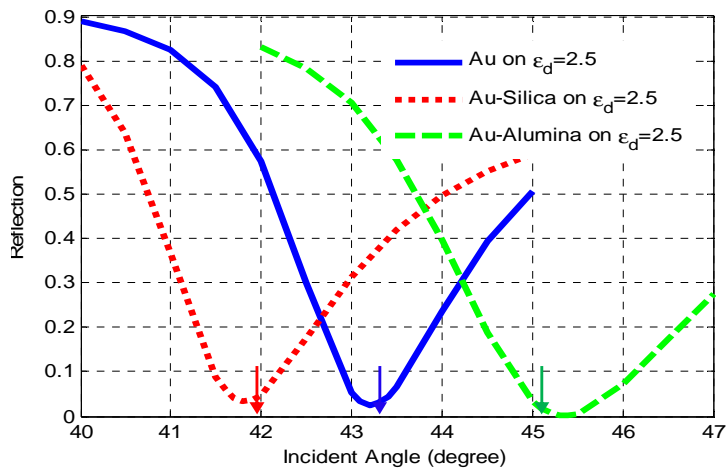
This case ( $p < 1$ ) highlights an especially interesting property of MMI stack, as the “diluting” of electron density by mixing metals with dielectrics does not sufficiently

lead to a decreased surface plasmon frequency. When a low-index filling material has applied its relaxation on the electron oscillation of a pure metal to form a MMI stack, a high-index coating (or substrate  $\epsilon_d$ ) will not be able to decrease the free electron oscillation down to  $\omega_p/\sqrt{1 + \epsilon_d}$ , as the “under-relaxed” MMI has somehow averaged or compensated for the relaxation taking place along the substrate boundary. This observation introduces new perspectives into spoof plasmonics, as an essential supplement to the conventional concept such as effective free electron density.

To verify the existence of this super resonance mode and better explain the tuning of effective surface plasmon frequency (ESPF), we introduce a specific case for an identical substrate material under uniform gold and two types of MMIs. In Figure 6.4, both MMI structures (and the uniform gold as reference) use the same substrate with  $\epsilon_d = 2.5$  (which can be regarded as a polymer-based photoresist). We then apply gold-SiO<sub>2</sub> ( $\epsilon = 2.1$  for SiO<sub>2</sub> at 633 nm) and gold-Al<sub>2</sub>O<sub>3</sub> ( $\epsilon = 3.15$  for Al<sub>2</sub>O<sub>3</sub> at 633 nm) multilayer stacks respectively to this substrate. It is obvious that the filling insulators have been chosen to make sure the ratio  $p = \epsilon_{\text{insulator}}/\epsilon_d$  can be less than unity for one case, and larger than unity for the other. Using the Equation (6.2) and the mode matching condition, we predicted the shifts of ESPF and SPR angle towards different directions (prism  $n_p = 2.6$ ). In Figure 6.4(a), the ESPF (upper cut-off for the TM band) is below and above the preset SPFs for different cases.



(a)



(b)

**Figure 6.4** (a) The analytical dispersion curves calculated by effective medium theory. The upper cut-off frequencies are treated as the effective surface plasmon frequencies (ESPFs) for two MMI cases. Near 633 nm, the shift of wave vectors are shown in the inset for uniform gold (blue), gold- $\text{Al}_2\text{O}_3$  MMI (green) and gold- $\text{SiO}_2$  MMI (red); (b) FDTD simulation for the shift of surface plasmon resonance (SPR) angles based on uniform gold (blue), gold- $\text{Al}_2\text{O}_3$  MMI (green) and gold- $\text{SiO}_2$  MMI (red). All three curves are on top of the same  $\epsilon = 2.5$  substrate. The small arrows mark the calculated angles based on mode matching.

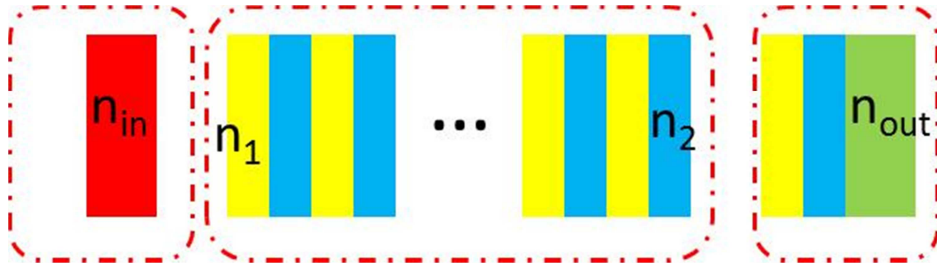
The FDTD modeling of these 3 structures under a Kretschmann setup is shown in Figure 6.4(b). MMI stacks are defined as 10 nm gold ( $\epsilon = -11.84 + j1.24$ ) plus 10nm

insulator for 5 cycles, and the shifts of SPR angle apparently go to opposite directions for different  $p$  value, verifying the theoretical calculations above. The simulated angles match well with the analytical results marked by small arrows (Figure 6.4(b)). The insets of Figure 6.4(a) also imply that under the light source of the same frequency, MMI stack can host a surface wave with a different wave vector as well as the mode size, which can be useful for optical lithography [174]. Although in the theoretical analysis above we have limited the discussion to real propagation constant, we find that the general conclusion can still be applied even to visible spectrum when the ohmic loss from metal is moderate.

### **6.3 Transfer-Matrix Method (TMM)**

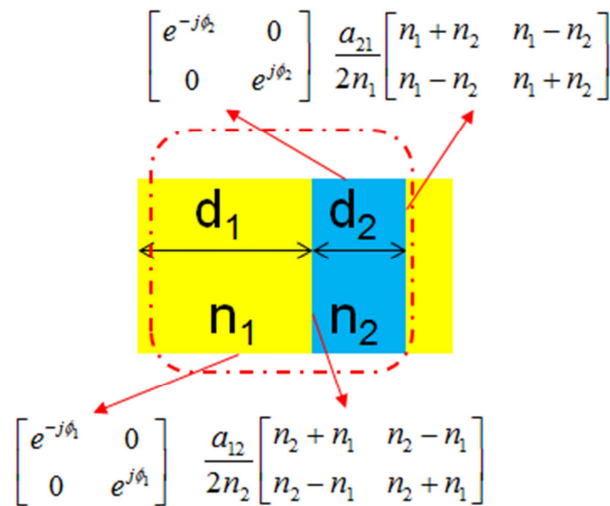
#### **6.3.1 TMM review**

The transfer-matrix method (TMM) [170] for multilayer stacks in general gives more accurate results compared with the effective index method shown in last section. As pointed out, effective medium theory could adapt to multilayer designer's requirement faster, and TMM would yield fast and robust results especially for the theoretical modeling of Kretschmann's attenuated total reflection (ATR). The implementation of TMM for periodic multilayer films can follow either the  $[E H]$  transfer matrix [170] or S-Matrix [183]. A demo code for single-layer ATR calculation is attached in Appendix 10.B. Based on TMM method, it is also convenient to determine how much power is reflected, transmitted or absorbed in the form of surface plasmon waves. It is also shown that the TMM method can be also applied to solving complex multilayer waveguides promptly [184] [185]. But in this dissertation, we only focus on the evanescent light coupling problem [186].



**Figure 6.5** Transfer matrix problem with an unmatched top coat (noted by the different values between  $n_{out}$  and  $n_2$ ).

The transfer-matrix method uses the Fresnel's law to determine the propagation constant of the propagating surface waves. In other words, the tangential part of the incident beam's wave vector is regarded as constant once the incident angle of the beam is set. The S-matrices of cascaded systems can be multiplied directly if the interface between each system is matched. Otherwise, an additional S-matrix (built directly from Fresnel's law) can be added to correct the mismatch (Figure 6.5).



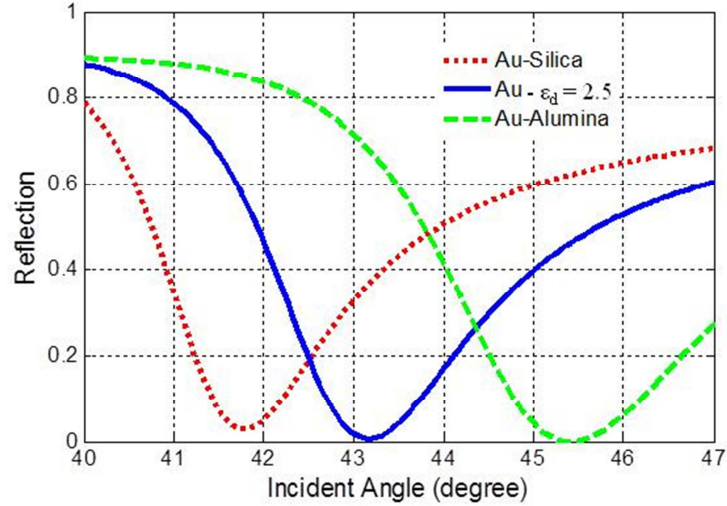
**Figure 6.6** Example for one pair of metal-dielectric unit in a cascaded transfer matrix system. Two boundaries and two “free propagations” are labeled for their respective transfer matrix.

Figure 6.6 shows a unit of the metal-dielectric case and the formation of several matrices. The phase term  $\phi_i$  is analogy to the phase change of waves propagating in a transmission line in microwave systems, which can be defined as  $n_i k_0 d_i \cos \theta_i$ , when  $k_0$  denotes the vacuum wave vector and  $\theta_i$  the incident angle [183]. It is important to note that in metal-dielectric composite, the physical meaning of this phase term is not as straightforward. If the “transmission line” describes a thin dielectric layer, the propagation does not induce amplitude but only phase change. In other word, the phase change of light propagated in dielectric will be determined by the propagation distance regardless of the direction travelled if the real propagation constant is known. The propagation constant will be a negative real number if an evanescent wave in the “positive” direction (usually the same direction as the incidence), and a positive real if a propagation wave. On the other hand, if the “transmission line” describes a thin metal layer in the multilayer system, there will be both amplitude and phase change because of the complex propagation constant. In this case, the complex propagation constant needs to have proper definition of the sign [187].

### 6.3.2 An ESPF case study with TMM

The 5-period case shown in Figure 6.4 is recalculated using TMM Figure 6.7, showing great match with FDTD results but with much less computing time. TMM can potentially be used to further optimize the performance of multilayer stacks because of its faster calculation compared to numerical methods such as FDTD. For example, to get one ATR curve like in Figure 6.7, it takes about 10 points to complete a smooth curve. In FDTD it means 10 individual simulations. At large incident angles, because of the

weakened absorption of PMLs, it could take even longer for the simulation to stabilize and finish.



**Figure 6.7** TMM calculations for the structures calculated by FDTD shown in Figure 6.4. Note that the curve plotted by solid blue line is a multilayer case compared to the single layer case shown in Figure 6.4.

## 6.4 Experimental Demonstration and Discussion

### 6.4.1 Experiment design

To verify the tuning of surface plasma frequency, we have modeled a Kretschmann prism-coupling process (Figure 6.8) for 633-nm light engaging a uniform gold film and an MMI gold-alumina stack (both cases have 50-nm total thickness of metal) using FDTD Solutions of Lumerical [92]. Previous effort [179] has successfully demonstrated the existence of complex modes supported by MMI systems, while here we focus on the link between the tunability of surface waves and the  $p$  parameter. Here we try to launch incident beams from a dielectric prism ( $n_p = 2.6$ ) to excite the surface waves when the plasmons are neighbored to silicon dioxide ( $n = 1.45$ ) or silicon nitride ( $n = 2.01$ ). The dielectric constants of gold ( $\epsilon = -11.84 + j1.24$ ) and alumina ( $n = 1.776$ ) are

fitted data from [131] and [39] respectively. According to momentum matching condition for SPR, the incident angle can be calculated theoretically as

$$n_{prism} k_0 \sin \theta_{sp}(\omega) = k_{sp}(\omega). \quad (6.10)$$

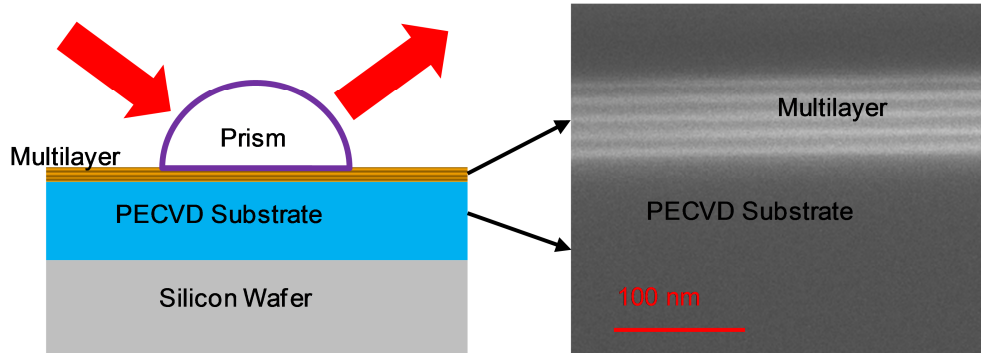


**Figure 6.8** Experimental setup for studying multilayer metal-insulator stacks and the cross-sectional view of the fabricated multilayer sample (SEM). Each individual layer is 10 nm and there are 10 layers (5 pairs) in total.

Note that for Kretschmann setup and the calculation from Equation (6.10), the mode of the greatest interest here is the confined fundamental TM mode. Although MMI could support more complex modes [179]-[181], the analysis in last section is sufficient to predict the sharpest resonance point of bounded SPP waves under this condition. It has been shown in [179]-[181] that there could be several reflection dips for these multilayer structures, as also verified in section 6.4.3. The physical meaning and the technical significance is temporarily out of the focus and will be explored elsewhere.

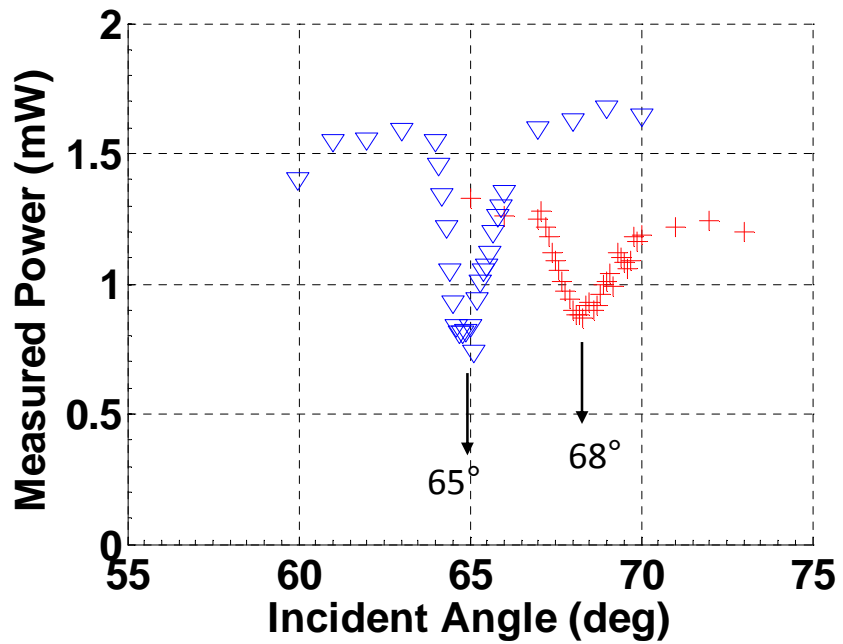
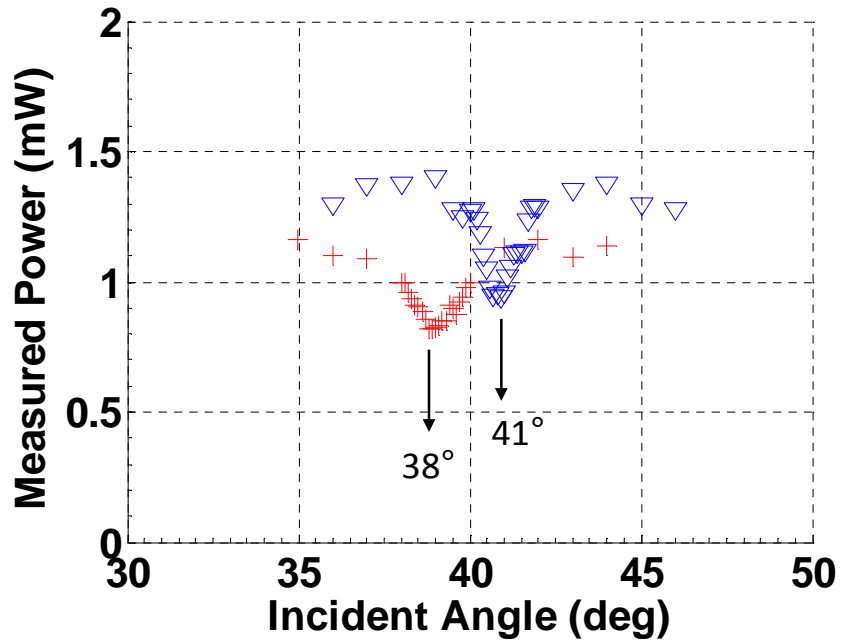


Figure 6.9 Experimental results of reflection vs. incident angle for (a) increased ESPF with SiO<sub>2</sub> substrate and (b) decreased ESPF with Si<sub>3</sub>N<sub>4</sub> substrate. Red crosses and blue triangles denote the measured results.

#### 6.4.2 Preliminary experimental result

As the original surface plasmon frequencies are shifted lower (silicon dioxide substrate, Figure 6.9(a)) and higher (silicon nitride substrate, Figure 6.9(b)), the  $k$ -vectors are shifted larger and smaller accordingly. The variation of the incident angle for minimum reflection can then be used to observe the tuning of surface plasmon frequency. Based on Equation (6.10), we have theoretically calculated the resonant angle shift for  $+2^\circ$  for silicon oxide substrate, and for  $-9^\circ$  for silicon nitride substrate. This corresponds to the excitation angles shifting from  $38^\circ$  to  $41^\circ$  for tuning down (silicon dioxide substrate), and  $71^\circ$  to  $61^\circ$  for tuning up (silicon nitride substrate), which match well with the TMM results.

Measured reflected power from a Kretschmann setup with a ZnSe ( $n = 2.6$ ) hemispherical prism are collected by an optical power meter from multiple samples illuminated by a collimated TM-polarized He-Ne laser beam (Figure 6.8, left). The SiO<sub>2</sub> and Si<sub>3</sub>N<sub>4</sub> substrates are deposited via plasma-enhanced chemical vapor deposition (PECVD), while the gold single-layer and gold-alumina multilayer are deposited via e-beam evaporation (Figure 6.8, right). The thickness of deposition is kept identical to the simulations performed above. The red crosses and the blue triangles in Figure 6.9 denote the results of gold single layer and gold-alumina multilayer respectively. The observed SPR angles shift from  $39^\circ$  to  $41^\circ$  for silicon dioxide substrate, and  $68^\circ$  to  $65^\circ$  for silicon nitride substrate. The shift direction of SPR agrees with the major conclusion regarding the refractive index relation between the substrate and the filling dielectric film. The discrepancy between the exact observed SPR angle and the calculation might be caused by fabrication disorder and the variation of dielectric constants compared to fitted data,

but the disagreement of the effective indexes of super modes between the measured and calculated values are all below 2.5% level.

### **6.4.3 Discussion and data fitting**

The discrepancy could be partially addressed by reversely fitting the material database, or implementing more variables in numerical and theoretical results. There are at least three other factors contributing to the discrepancy, and some of them can be addressed by data fitting.

Firstly, there could be differences in physical properties between the realistic materials used in sample preparation and those found in published material handbook such as Palik's or CRC's. Both the plasmonic materials (gold) and the substrate dielectrics (Silicon Nitride or Silicon Dioxide) could vary from tabulated values depending on the deposition conditions. It would be then necessary to measure the actual films using ellipsometer to determine their physical properties, although the in-situ deposition of multilayers could make this measurement difficult. Secondly, the mechanical condition in this experiment, especially the airgap between the prism and the substrate could change the relative reflection drop. The comparatively large refractive index of the prism used also makes it difficult to find a matching fluid to fill this gap. Without reversely fitting the thickness of the airgap, the reflection dip will not display the same contrast as predicted in simulations or calculations. Finally, the numerical models developed for FDTD simulations, as well as the theoretical analysis based on the traditional EMT theory and smooth films, might have not fully captured the nature of realistic composition of the multilayers. The roughness of the evaporated films could

form complex composites at the interface, as has been reported in [188] to use Maxwell Garnett approach to quantify this effect.

Based on the transfer-matrix method implemented and described in last section, a refractive index fitting for the substrate material ( $\text{SiO}_2$  or  $\text{Si}_3\text{N}_4$ ) as well as an airgap distance fitting is necessary to lessen the discrepancy. In this fitting process, we keep gold and  $\text{Al}_2\text{O}_3$ 's dielectric constants same to their nominal values found in [131] ( $\epsilon = -11.84 + j1.24$ ) and [39] ( $n = 1.766$ ) respectively.

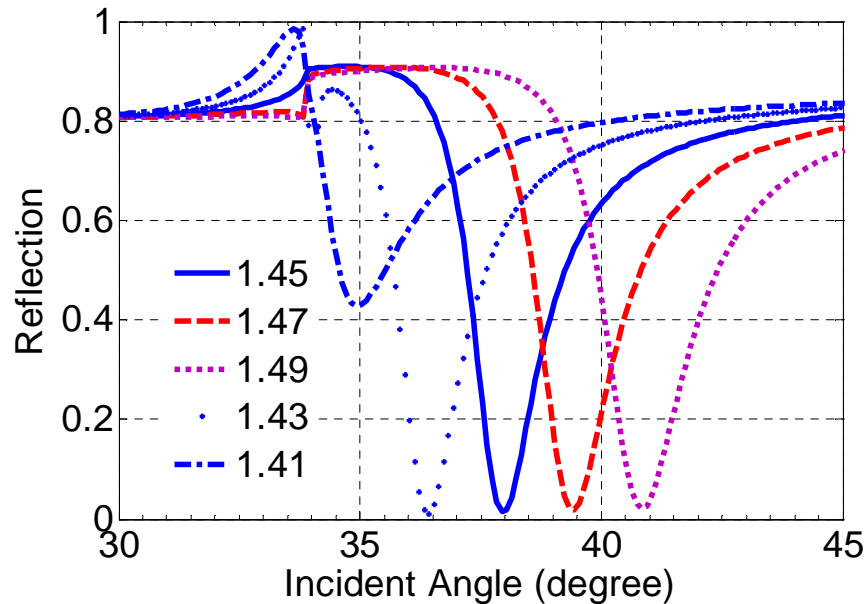


**Figure 6.10** Substrate scan and curve change for 50nm gold only

Here we isolate the effects of different factors to gain a better understanding of their physical impact on the  $R-\theta$  curve. Firstly, we change the substrate material's index moderately and examine the  $R-\theta$  curve. This change is practical for the inevitable variation of material property because of complex deposition conditions. As an example,

we change the SiO<sub>2</sub> substrate's index for a  $\Delta n = \pm 0.5$  around its nominal value  $n = 1.45$ . The results are shown in Figure 6.11.

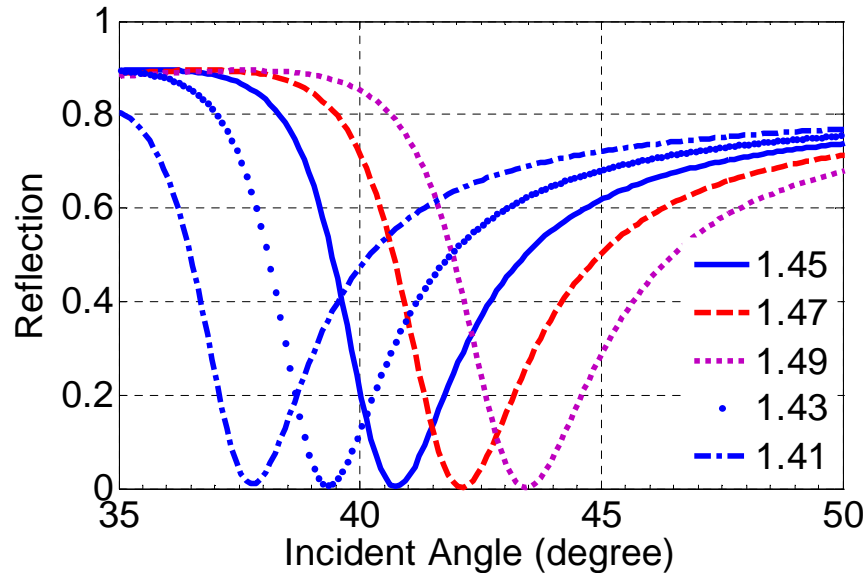
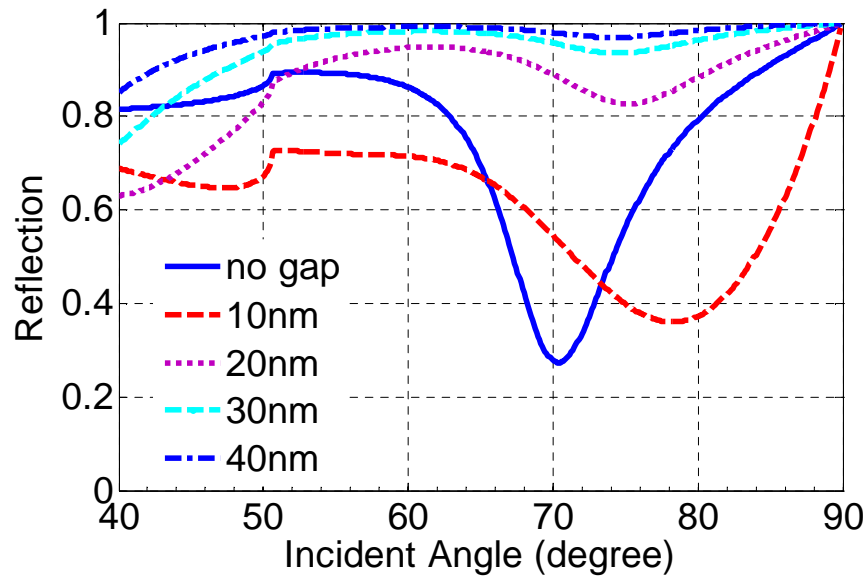


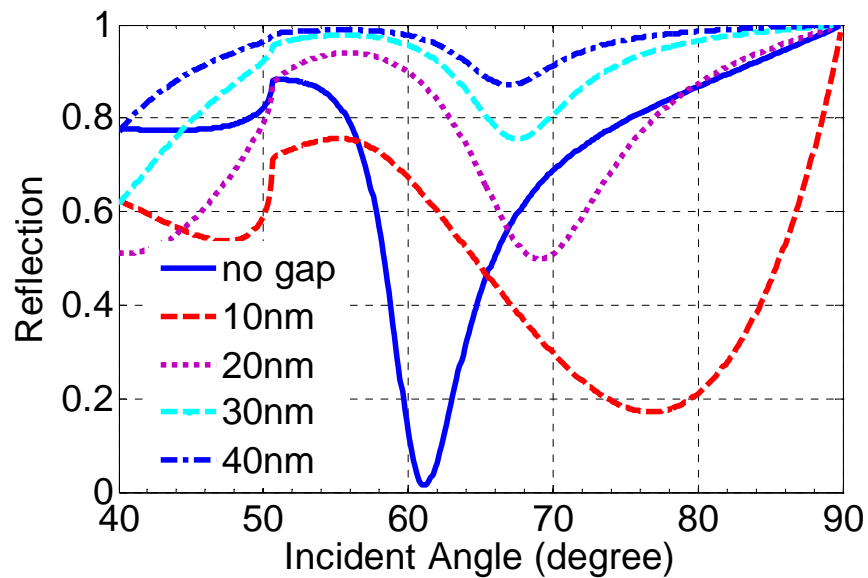
**Figure 6.11** Reflection curves changed with different SiO<sub>2</sub> substrate's refractive index. In general, a larger refractive index of substrate will shift the SPR angle to a larger value.

From Figure 6.11, we find that the SiO<sub>2</sub>'s refractive index variation will indeed shift the reflection dip. In general, a larger refractive index of substrate will shift the SPR angle to a larger value. It can also be clearly seen that the multilayer's R- $\theta$  curves are in general similar in nature. No additional sharp dip shows up around the angles to our interest. This is important for the experiment verification.

Secondly, we introduce an additional airgap to the designed platform between the high-index prism and the multilayered medium. First we use the Si<sub>3</sub>N<sub>4</sub> substrate as the reference (Figure 6.12). It can be seen that the curve is very sensitive to the gap distance, for both the dip contrast and the position (incident angle). However, it is also evident that an additional airgap will not nullify the shifting direction of the ESPF.



(a)



(b)

**Figure 6.12 Comparison of fitting different gap widths for (a) Si<sub>3</sub>N<sub>4</sub> and (b) gold and alumina multilayer on Si<sub>3</sub>N<sub>4</sub>.**

As a comparison, the case for SiO<sub>2</sub> substrate is shown in Figure 6.13. The sensitivity regarding the gap widths is obviously less compared to the Si<sub>3</sub>N<sub>4</sub> case, but a wider gap will still reduce the contrast of the reflection dip. Again it is clear that with the

existence of an airgap, the multilayer device will usually have larger SPR angle. So the qualitative observation in the experiment (angle shifting direction) remains legitimate while there might be unavoidable quantitative discrepancy.

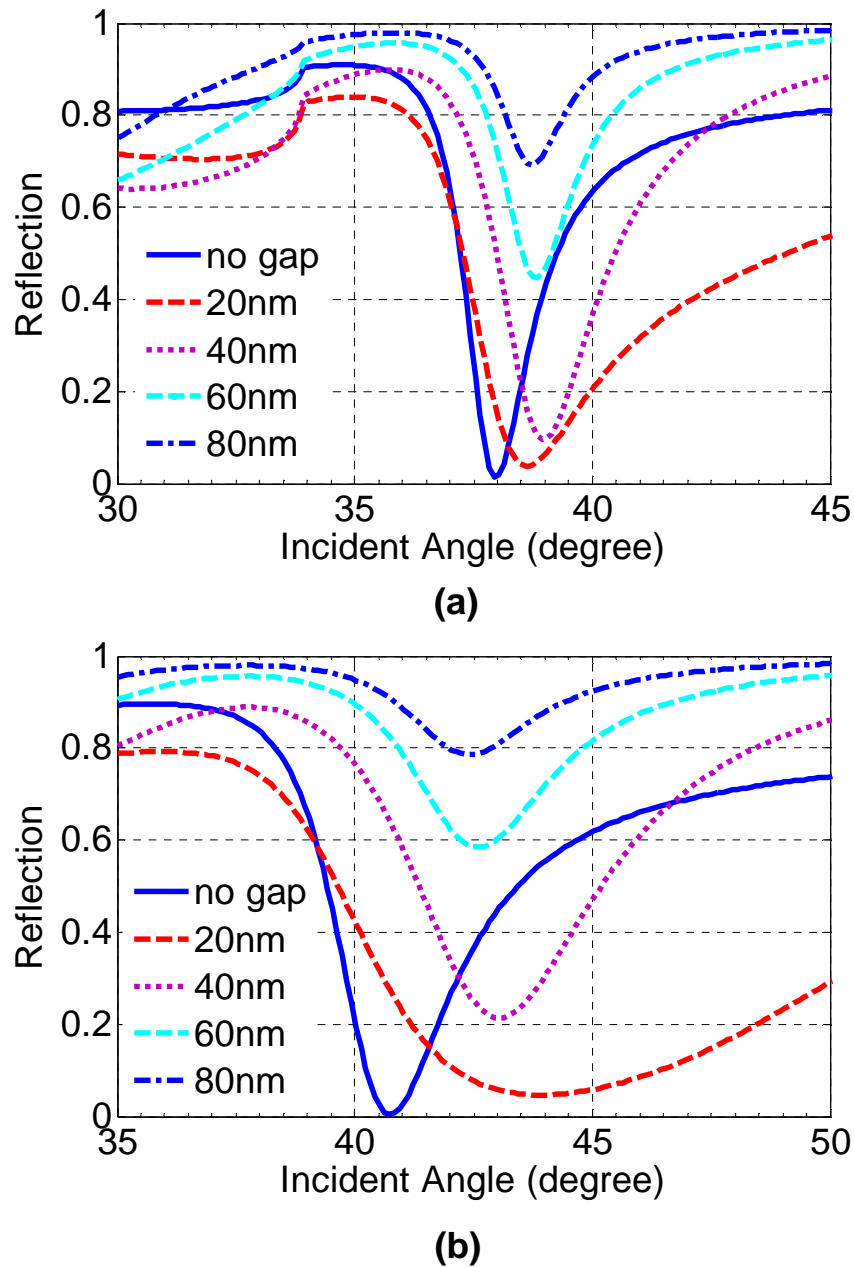
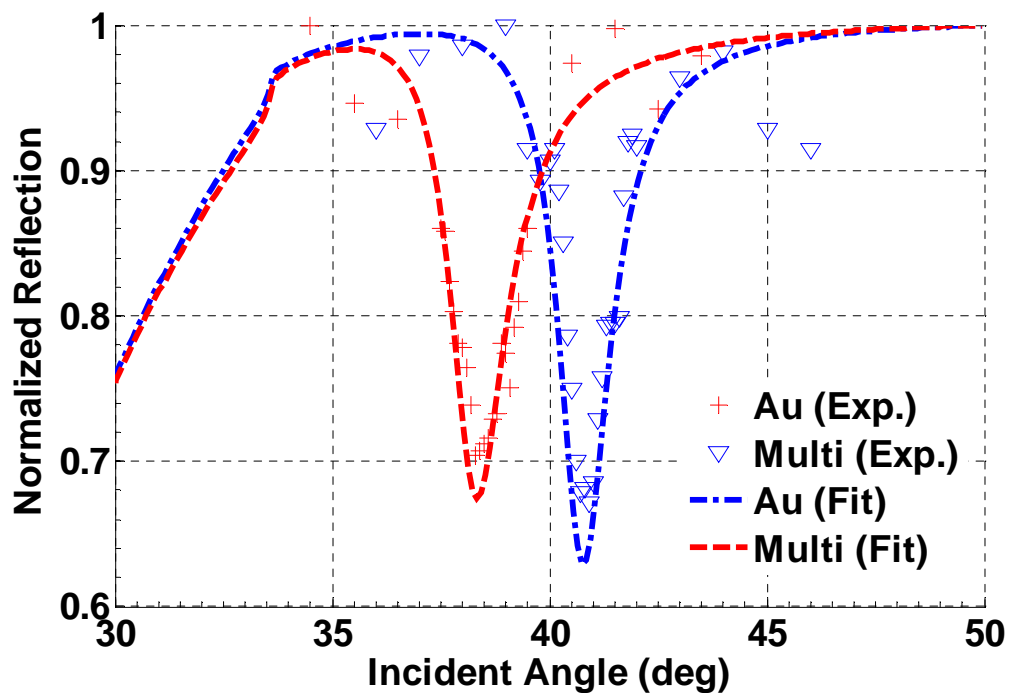


Figure 6.13 Comparison of fitting different gap widths for (a) gold on SiO<sub>2</sub> and (b) gold and alumina multilayer on SiO<sub>2</sub>.

Based on the study above, a multiple-parameter fitting is performed. The idea behind this fitting is to use the airgap width to tune the contrast about how deep the reflection dip is, and to use the variation of the substrate material to tune the resonance angle. Figure 6.14 plot the fitted results for the SiO<sub>2</sub> substrate and their match with experimental results. Fitting parameter here is  $n = 1.44$  for the substrate, gap width = 80 nm for both gold only and gold-alumina multilayer. A slightly more absorptive gold with  $n = 0.1-j*3.62$  have been used for the multilayer case, compared to the nominal value ( $n=0.18-j*3.446$ ) used in the gold only case.



**Figure 6.14** Fitting curves for the two samples on SiO<sub>2</sub> substrate. Fitting parameter here is  $n = 1.44$  for the substrate, gap width = 80 nm for both cases. The multilayer case uses  $n=0.1-j*3.62$  for gold's refractive index, while the gold only case uses  $n=0.1799-j*3.4456$ .

A resonant-angle-only fit is performed with 20-nm gap for  $n = 1.95$  substrate (Figure 6.15), aligning the reflection dips close to the measurement (65° and 68°). We

have noticed that under the current fitting range, it is difficult to fit the contrasts and dip widths for the  $\text{Si}_3\text{N}_4$  substrate (Figure 6.15), which might need further investigation in future with more advanced and accurate measurement setup as well as thorough material characterization. As a summary for the discussion above, the experimental results at this stage could qualitatively verify the tuning of the ESPF with the relative change of the resonance angle (reflection dip).

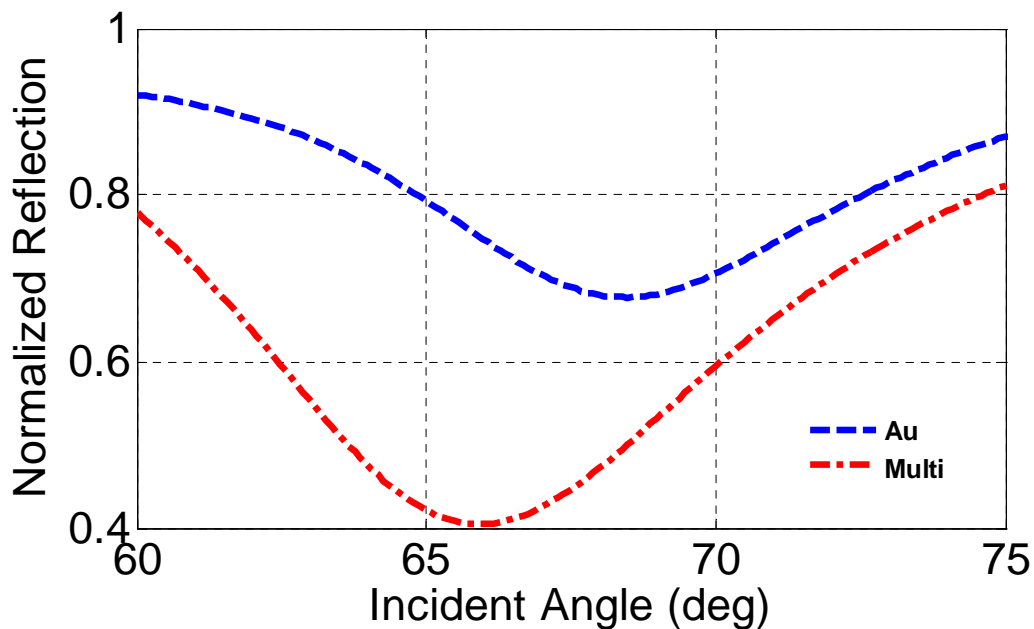


**Figure 6.15** Fitting curves for the two samples on  $\text{Si}_3\text{N}_4$  substrate. Fitting parameters are 20-nm gap and  $n = 1.95$  substrate for both cases.

## 6.5 Further Numerical Modeling for ESPF Tuning

The results shown in Figure 6.9 do not only verify the analytical basis of last section for optical sensing based on SPR, but also suggest possibilities of using MMI stack to achieve manageable mode size and wider frequency range for plasmonics applications. Specifically, as the surface plasmon frequency is tuned down, the dispersion curve “flattens” faster in MMI case and therefore at the same frequency of incident light,

the propagation constant is increased and smaller wavelength of surface waves can be created which is impossible using uniform metal. On the other hand, by tuning up the ESPF it is possible to broaden the frequency range of surface waves.

As an example, in Figure 6.9(a,b), we use the design rules mentioned above to illustrate how the increased ESPF allows super surface modes at frequencies beyond the conventional surface plasmon frequency. In this modeling we use normalized frequency and length unit. We set the background material as  $\epsilon_d = 2.5$ , and the MMI system consists of 20 pairs of thin layers ( $\epsilon_1 = 1.25$  and  $\epsilon_2 = -1.8$ ) for a filling ratio  $\eta = 3$ . If a Drude metal is used here, the working frequency will locate at approximate  $0.6\omega_p$ , larger than the conventional cutoff of  $\omega_p/\sqrt{1 + \epsilon} = 0.53\omega_p$ . For uniform metal at this frequency, there will be no surface waves supported at the boundary (Figure 6.16(a)). With the tuning of ESPF from MMI, however, the working frequency can now exceed  $0.58 \omega_p$ . Here we use COMSOL [189] to simulate the propagation of the super surface mode (Figure 6.16(b)), showing the subwavelength confinement of the engineered super surface mode bounded and propagated along. Note that in this simulation, the thickness of each repeated unit is  $0.04 \lambda_0$  ( $d_2 = 0.03 \lambda_0$ ,  $\eta = d_2/d_1 = 3$ ), and the EMT theory could well approximate the behavior of the super surface mode. The mesh-size is small enough to resolve the finest layer  $d_1$ .

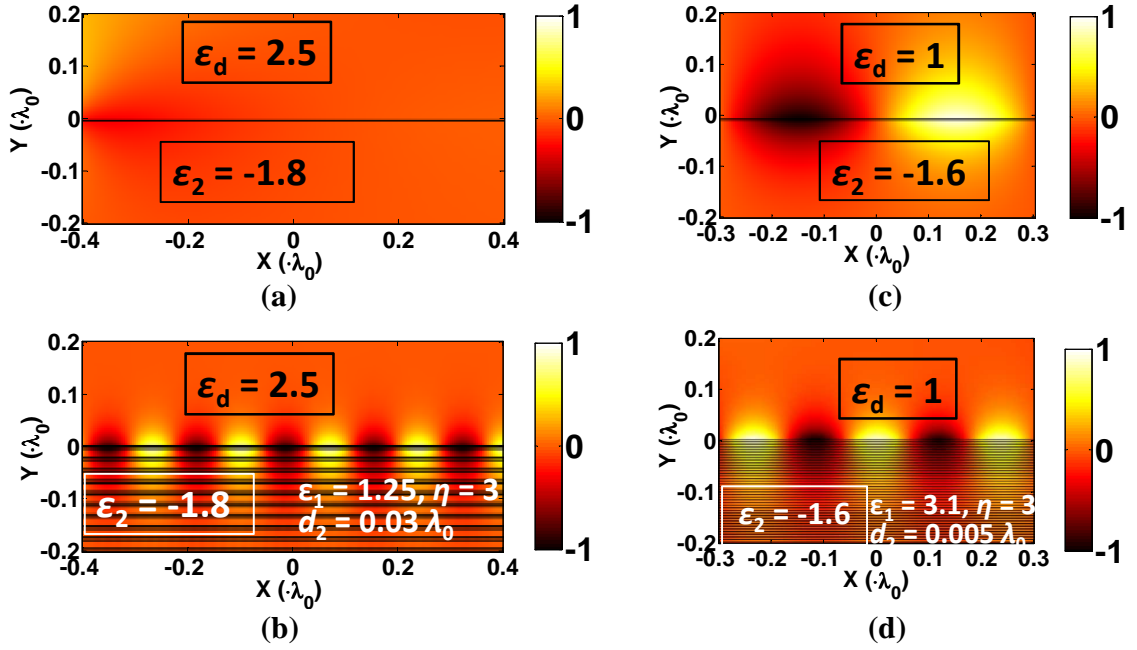


**Figure 6.16** *H*-field distribution for: (a) No bounded surface modes above surface plasmon frequency; (b) Bounded surface wave beyond conventional cutoff frequency defined in (a); (c) Bounded surface wave propagated on a single metal-insulator interface; (d) Bounded surface wave on a MMI-insulator boundary with shorter wavelength and manageable mode size compared to (c).

Figure 6.16(c) and (d) gives another pair of illustration for mode size engineering with multilayer stack. Here the background material is  $\epsilon_d = 1.0$ , and the MMI system consists of 35 pairs of thin layers ( $\epsilon_1 = 3.1$  and  $\epsilon_2 = -1.6$ ) for a filling ratio  $\eta = 3$ . According to the design rule, a low-index coating will decrease the ESPF as well as the wavelength of the super surface wave. The metal-insulator boundary shown in Figure 6.16(c) supports the fundamental TM surface wave for a wavelength of  $0.61 \lambda_0$ , as can also be calculated from Equation (6.4). When the uniform metal is replaced by “metametal”, the dispersion curve will bend faster away from lightline (Figure 6.4(b)). Therefore, a larger wave vector plus a decreased wavelength ( $0.26 \lambda_0$ ) is expected. According to the dispersion relation, this trend will also shrink the length of the

exponential tail in the dielectric side, as can be clearly seen comparing the  $H$  field distribution in the  $\varepsilon_d = 1.0$  region of Figure 6.16(c) and (d). We have also observed the variation of wavelength relative to the thickness of each repeated unit, as have been mentioned in [170], which indicates the limit of EMT and a general preference of using thin layers to match EMT's prediction given by Equation (6.2).

## 6.6 Conclusions

We have theoretically and experimentally investigated the MMI stack as a plasmonic metametal and studied its capability of supporting surface waves and engineering surface plasmon frequency. The analysis suggests a concept of effective surface plasmon frequency that can be well controlled, and provides new insight into using MMI stacks to accomplish deep subwavelength imaging and artificial dispersion of electromagnetic waves. The outlined design rules would empower researchers to excite more confined surface waves from a limited pool of plasmonic materials for optical lithography and subwavelength imaging, as well as to envision and demonstrate novel detecting/sensing scheme.

---

# 7 ACTIVE PLASMONICS

---

## 7.1 Introduction

Surface plasmon waves are formed by the combination of optical EM fields and free electron gas oscillation. For one thing, the combination maintains the frequency of optical waves, which is usually at the higher end of telecommunications above 100 THz. For the other, the free electrons exhibit negative permittivity and could possibly yield subwavelength mode spread and hence extreme field confinement. These two features are highly attractive for the development of communication systems or photovoltaic (PV) energy systems, which usually demand both fine devices/waveguides and high operation frequency (Figure 7.1, adopted from [190]). It is therefore important to explore “active” plasmonics, especially the possibility to modulate or detect plasmonic waves as well as to enhance the optical absorption with the assistance of plasmonic elements.

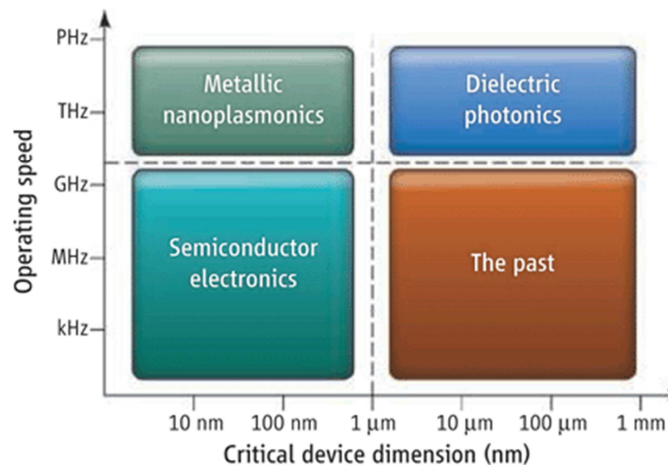


**Figure 7.1 Plasmonics for faster operation and smaller dimension. Adopted from [190].**

As a fairly new and advanced topic in nanoplasmonics, active plasmonics have been a heated topic for more than 5 years [191] regarding the development of plasmonic source [192], plasmonic modulators [44], plasmonic detectors [193] and plasmonic-enhanced solar cells [194]. In this chapter, the author will present possible approaches toward active plasmonic devices with numerical simulations and possible fabrication steps.

## 7.2 Approaches

Plasmonic waveguides are never known as of incredibly low loss and long propagation length. Instead, it features acceptable loss for on-chip signal transmitting, extreme confinement for high density deployment and enhanced light-matter interaction. Due to the ohmic loss of metals, it is also difficult to design plasmonic cavities for ultra-high  $Q$ -factors. Following the argument made above, it is reasonable to consider plasmonics' role in monolithic OIC as active modules with small foot-prints, fast responses and critical sensitivity.

Several important discoveries have been reported for active plasmonics. Regardless of the comparatively low  $Q$  of plasmonic cavities, prototypes have been developed for plasmonic lasing source [192]. Atwater *et al.* has demonstrated a field-effect device controlled by electric modulation [54], while optical modulation of plasmonic waves has been reported in [118]. Recently, Berini *et al.* [193] has also shown that a Schottky diode can be made through the formation of plasmonic waveguides. The inspiring research mentioned above predicts at least two promising approaches toward active plasmonic devices. The first is based on external electromagnetic fields, which could change the property of materials in plasmonic structures. In this way, one can either

change the propagating mode's propagation length by increasing the loss of an involved material or even eliminate the original guided mode and make another mode dominant (usually with drastic change of propagation distance) [54]. This concept can also be designed into resonant devices with nonlinear medium for better performance at narrower working bandwidth [55]. The second is to use plasmonic modules as detectors or antennas for fast paced signal beyond terahertz spectrum. This can usually be implemented by designing Schottky diode [193]-[196], or even tunneling (Esaki) [197] diodes [198]. Based on the approaches mentioned above as well as the structures presented in previous chapters, future work and further efforts are suggested in the next section.

Moreover, the surface waves bounded by plasmonic materials could not only carry signals but also help to effectively deliver and store optical energy. With more and more concerns given to development of clean or green energy, the technique to directly convert solar radiation into electrical energy, known as Photovoltaics (PV), has undergone great progress [199] [200]. The structures that can absorb solar radiation and produce electrical current are generally referred to as solar cell. Under current scientific lab condition, 24.7% conversion efficiency is reported [199]. Based on the pace of past and recent development of solar cell efficiency, this conversion ratio is expected to be close to ~30% by 2040 [200]. As a newly emerged energy solution, however, PV technology uses cost per watt of electric power generated as the major figure of merit, instead of the conversion efficiency. The most significant impact of this economical consideration is the domination of silicon in PV industry, while silicon is in no way a perfect material for solar cell at the first glance [200]. According to [200], the element of

silicon in its various forms (amorphous, crystalline, etc.) takes 99% market share in PV technology for the year of 2002, and the cost of silicon takes almost 50% of the whole PV modules manufactured in the world.

Thin-film silicon PV structure, therefore, is potentially competent in reducing module cost, while sustaining stable performance (~15% conversion efficiency is acceptable for thin-film PV) [200]-[202]. Based on the overwhelmed use of silicon and the well-developed silicon VLSI technology, thin-film silicon solar cells have great design freedom and have already had several prototypes for further development. One of the following sections will discuss the designs of thin-film silicon platform, on which metal contact is formed and plasmonic structures are incorporated.

### **7.3 Electric Field for Modulation**

#### **7.3.1 Background**

Guiding modes in plasmonic waveguides are deemed sensitive to small changes in guiding materials. For a metal-insulator-metal (MIM) or metal-insulator-semiconductor (MIS) waveguides including an insulator core for mode confinement, this small change can take place in either the insulator layer or cladding layer. For a 20-nm lossless insulator with refractive index  $n=1.45$  buried in gold, at  $1.55 \mu\text{m}$  the propagation constant of the fundamental TM mode (2-D case) will be about 2.654 with a propagation loss of  $3.00 \text{ dB}/\mu\text{m}$ . To achieve amplitude modulation, the guiding area can be filled with active materials. For 0.01 variation in the imaginary part ( $n=1.45-j0.01$ ) of its refractive index, the real part of the propagation constant will still be close to 2.654, but the propagation loss be risen to  $3.46 \text{ dB}/\mu\text{m}$ . In the example shown above, a -3 dB modulation can be achieved for a propagation length of  $6.5 \mu\text{m}$ . A trade-off regarding the

core dimension is expected. For one thing, a thinner insulator layer requires less power to switch, while for the other, a slightly thicker active layer will generate more absorption. Based on this approach, one can introduce the perturbation of the refractive index in insulator layers to a 3-D single mode MIM waveguides previously described in Chapter 4, in which further optimization regarding the guiding layer's thickness is expected.

Another prior approach worth a special mention is to change the refractive index of the metallic layers, as shown in [118], to explore the interband transition of plasmonic materials. Similar methods can be applied to different field-effect devices with a semiconductor layer as the cladding layer. Usually a MIS device can possibly support various guided modes with different propagation lengths. Different external voltages will be able to push dominant modes from one to another and therefore change the throughput with careful designs [52] [203] .

The field effect devices switched by vertically-sent electric signals, as reported by Atwater *et al.* [54], can be adapted for a variety of active plasmonic devices. For example, Lu and Zhao [203] have tried to explore the possibility of integrating graphene layers into plasmonic waveguides to form an ultra-sensitive channel for bias voltage. Based on the approach suggested in Figure 7.2 (reorganized from Figure 2 in [203]), one platform of interest made of multilayers have been fabricated by the author, and will be prepared for graphene transfer in near future.

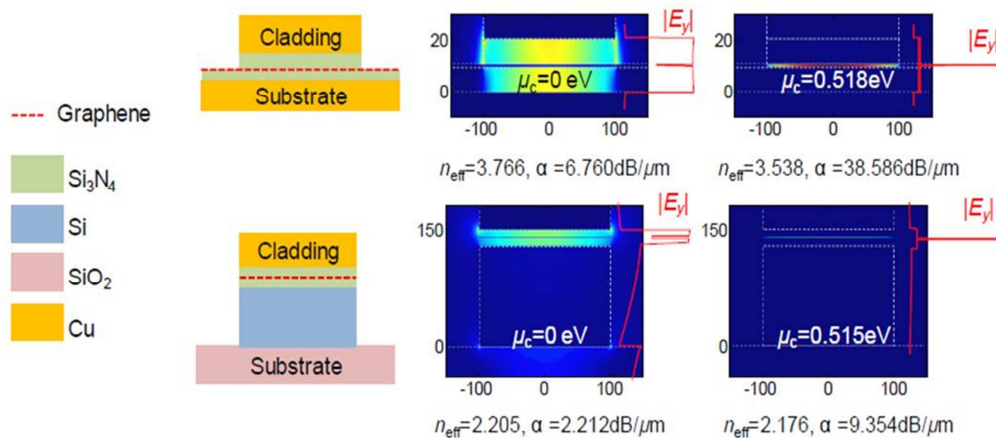


Figure 7.2 Comparison of transverse E-field profiles with or without external voltage ( $\mu_c = 0$ ) for two graphene-based designs. Adopted from Figure 2 in [203].

### 7.3.2 Fabrication approach

Specifically, the platform fabrication can start with a double-side polished wafer, which will be later etched through after the supporting layers of graphene are successfully deposited. Based on the approaches shown above, one possible design with doped polysilicon for about 150 nm is shown in Figure 7.3.

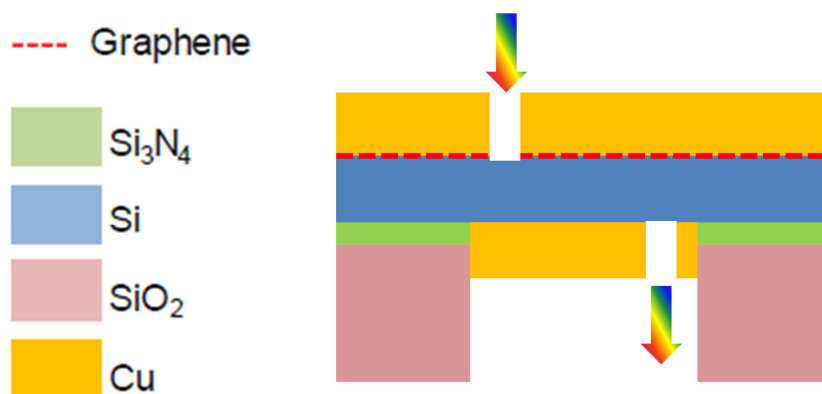
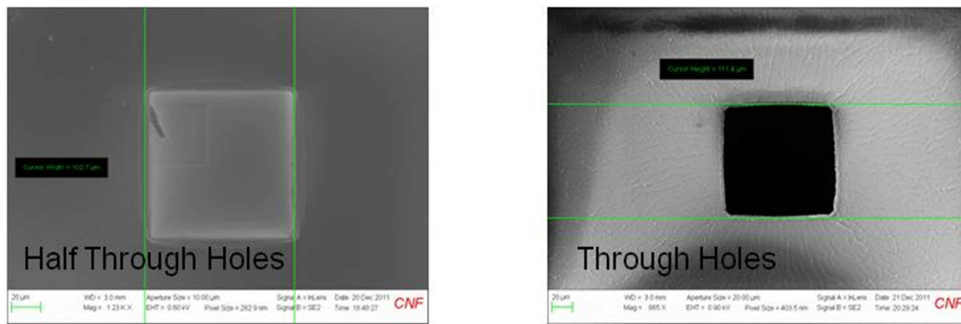


Figure 7.3 One possible design with doped polysilicon as the supporting layer. The substrate silicon is not shown in this figure. Silicon nitride layer is deposited between silicon dioxide and polysilicon to make the supporting layer more tensile.

Firstly, about  $1.5\ \mu\text{m}$  thermal silicon dioxide is grown on the bare double-side polished wafer. This is followed by sequential deposition of silicon nitride for 50 nm and polysilicon for 150 nm. The silicon nitride should be of tensile nature to balance the compressed silicon dioxide underneath. Polysilicon on top will then be doped by placing the wafer in anneal furnace for N-type dopants. As only the top side of the polysilicon will be functional, the silicon nitride and polysilicon on bottom side will then be etched by  $\text{SF}_6/\text{O}_2$  in Oxford 80 while the top side is protected by S1813 photo resist.



**Figure 7.4 SEM images of half through holes (with  $200\ \mu\text{m}$  silicon left, left) and through holes into  $500\ \mu\text{m}$  silicon substrate (right) after etched by Oerlikon.**

Secondly, the bottom side will be patterned by a two-stepped etching process. The first step is to pattern the silicon dioxide hard mask, which is made possible by coating SPR-220 photoresist at 2-2.5 krpm for a target thickness of  $> 7\ \mu\text{m}$ . The silicon dioxide is then etched by  $\text{CHF}_3/\text{O}_2$  in Oxford 80 until approximately 100-nm is left, when the thickness of left-over oxide can be measured by FilMetrics F40. The rest oxide layer will bear over etch for 2-3 min into Silicon in Oxford 80 with  $\text{CF}_4$  as the gas. After removing the edge bead, the wafer is etched by Oerlikon deep silicon etcher. The half-through holes with approximately  $200\ \mu\text{m}$  silicon left and the final through holes are shown in Figure 7.4.

Finally, the silicon dioxide on top side can be removed by wet etch before graphene transfer and electrodes formation. All the materials, processing details and tools mentioned in this section are accessed through Cornell Nanofabrication Facility ([www.cnfusers.cornell.edu](http://www.cnfusers.cornell.edu)).

## **7.4 Tunneling Diode for NIR Light Detector**

### **7.4.1 Background**

Detection of NIR light in telecom regime can be challenging because of its low energy, especially for silicon-based optical circuitry. NIR plasmonic waveguides, on the other hand, can also be regarded as NIR signal carrier and have been explored as an effective platform for detection. Metal layers in plasmonic waveguides can naturally form electrodes, and could make the detecting unit potentially more compact. Waveguide-integration of Schottky diodes have been studied theoretically [193] [195], and have also been developed to yield high efficiency internal photoemission (IPE) [196].

Another approach towards NIR detection comes from the tunneling effect of electrons across the metal-insulator-metal barrier [204]. Tunneling diodes (Esaki diodes [197]) have been extensively studied for millimeter or THz wave detection [205]. External radiation is received by a rectifying antenna (rectenna) which usually contains capacitors with very thin insulator layers. Waveguide-integrated tunneling has also been reported [198], pushing the detection limit to  $1.6 \mu\text{m}$ . With the size of MIM diodes decreasing further to operate at NIR spectrum, it is natural to exploit the possibility of combining MIM waveguides and MIM diodes together to achieve a compact detecting solution.

### 7.4.2 Theoretical evaluation

To this end, the direct coupling process from dielectric waveguides to plasmonic waveguides can again be used to excite SPP waves in MIM waveguides as shown in Chapter 3 and 4, in which the optimization of the coupling efficiency will finally yield high signal-noise-ratio for a detector. The cut-off frequency of a MIM diode can be estimated by  $1/2\pi ZC$  (Figure 7.5, adopted from [206]), where the value  $Z$  is related to the impedance of the antenna or waveguide and  $C$  is the capacitance made of the MIM's overlap [206]. For gold-SiO<sub>2</sub>-gold waveguides with < 10 nm barrier and 40-nm width, it is calculated that a 50-nm overlap (forming a 50nm by 40nm MIM diode) is sufficient to rectify signals as fast as 300 THz.

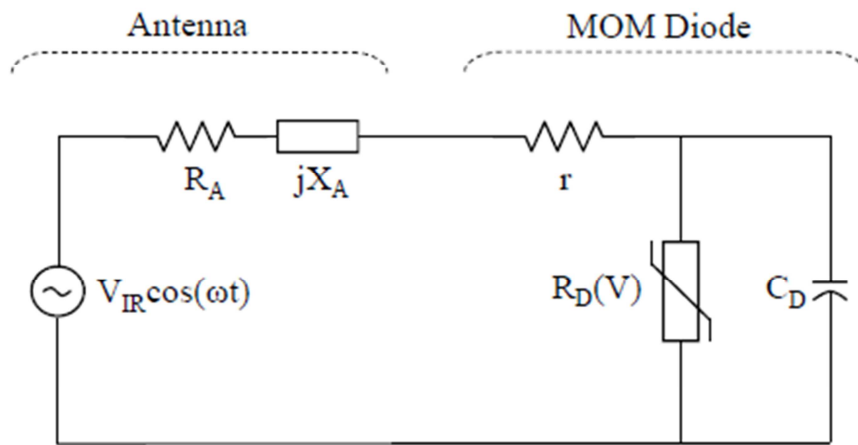


**Figure 7.5** Equivalent circuit to evaluate the cutoff frequency of an MIM tunneling diode. Adopted from [206].

The estimation above assumes the waveguide impedance as the value  $Z$ . This will not be practically possible because to isolate the diode area, and there must be discontinuity in the MIM waveguide area. The oscillation of free electrons has shown to

be able to “leap” across and small gap area and maintain the surface resonance, as shown in Bloch surface plasmons [207]. This feature can be applied to design MIM diode with ultra-small capacitance area, although the waveguide impedance will need to be corrected. For standalone insulating gaps, a few feeding schemes have been explored numerically as shown in Figure 7.6, in which the diode area will be further connected with electrodes.

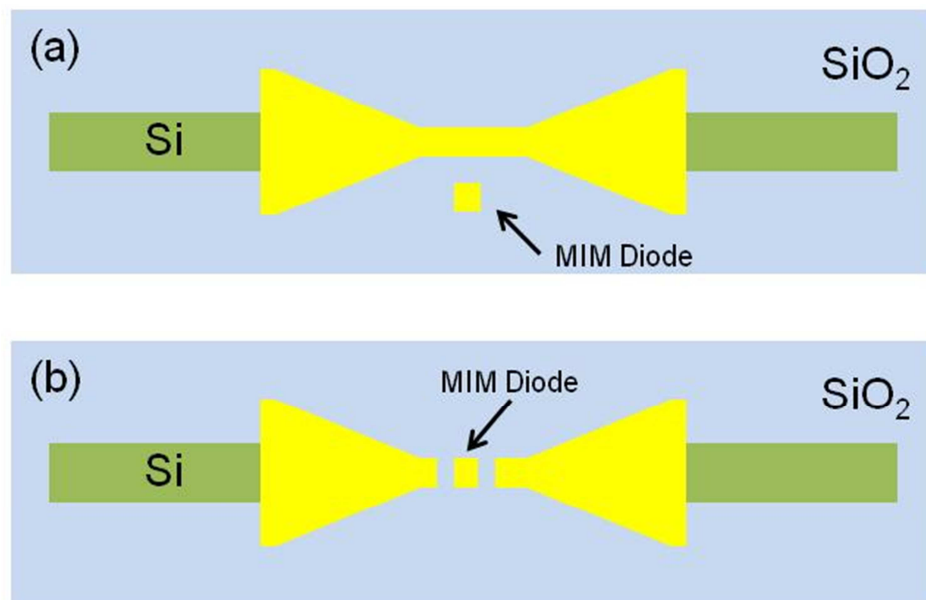


**Figure 7.6** Top-view of possible diode formation in (a) side coupled and (b) point fed.

The demonstration of this type of diode requires fine alignment between different levels. The bus waveguides and bottom electrodes can be aligned using e-beam lithography, following the basic fabrication approach introduced in Section 4.3. Because the insulator in MIM waveguides for this application is thinner and the quality requirement is extreme for tunneling devices, it might be better to use atomic layer

deposition (ALD) to deposit the insulator for a thickness of about 10 nm. The top electrode again needs critical alignment to previous layers.

## **7.5 Plasmonic-enhanced Solar Cell Prototype**

### **7.5.1 Background**

Silicon is the dominating material in PV market. Like in other semiconductor industry, the cheap raw material makes silicon a first option for large-scale PV module manufacturing. However, as mentioned above, even crystalline silicon has indirect bandgap and therefore the absorption is less likely to happen compared to direct bandgap material, which means the thickness of the absorption layer required for sufficient solar power conversion is greatly increased. It is calculated that at least 100- $\mu\text{m}$  film is required for silicon-based design if the module is aiming at practical use or commercialization [200]. Smaller thickness, as well as any defects or impurities inside silicon will decrease the total number of photon-generated free carriers that can be channeled out by contacts, in the form of unwanted recombination. There have been several approaches to address the disparity between the desire to reduce film thickness and the comparatively low absorption of silicon. One of the most straightforward methods is to use thin films with surface textures to increase the optical path of incident beam inside silicon region, to reduce the back-reflection and as a result to partially compromise the comparatively small diffusion length of photon-generated carriers in silicon. However, the surface features are general in the order of hundreds of nanometers and even higher [201] [202], which limit the material that can finally be saved from using thin films.

Two schemes for plasmonic enhanced absorption have been discussed recently, thanks to the growing interest in Plasmonics [208]. Plasmonic behavior is known to be related with subwavelength field or power confinement, huge field enhancement in near-field, rich physical interaction on structures' surface or tip, etc. The first type of application of plasmonics on solar cell design, which has been an active research topic, is related to metallic surface features on the front side (facing the sun) of the module [209] [210]. The plasmon enhanced light-trapping can replace the thick and complex surface features of silicon [211]. In this case, metallic 'islands' on top of silicon interact with sun rays firstly, help as a transceiver to transmit more power into the active region below. Samples with considerable absorption improvement with plasmonic effect [212] [213] have been demonstrated. The second type, recently proposed by [194], shapes a metal layer on the back side of the silicon absorbing layer, acting both as a plasmonic structure and a back contact. In this case, the metal layer scatters light that have gone through the thin silicon layer, redirecting part of them into in-plane propagating mode of either photonic or plasmonic nature. It has been estimated that the SPP loss of these plasmonic structures will not destroy the performance of thin-film solar cells. Instead, a bold estimation of over 85% efficiency can be theoretically achieved by using wisely designed plasmonic features [214]. Both of these two approaches have shown the promising future of plasmonics for enhanced light absorption, with very clear advantages over conventional schemes based solely on dielectric material.

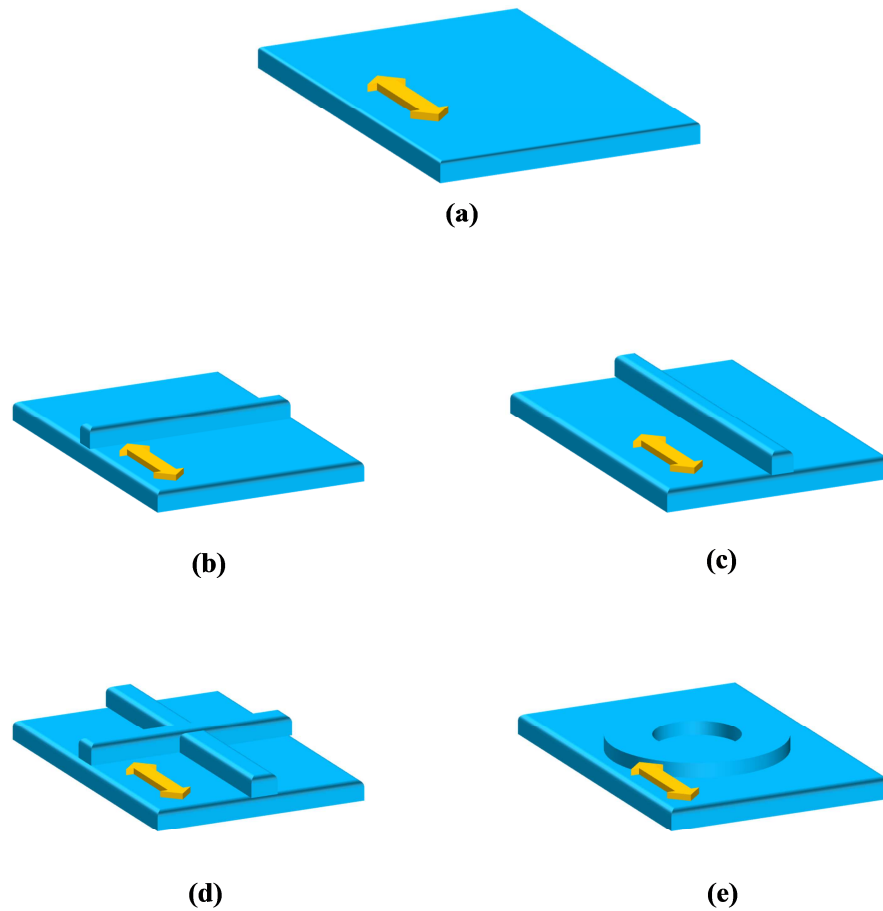


**Figure 7.7** Physical structure of typical plasmonic scattering sources. (a) Plain silver, (b) bar element extended normal to electric field, (c) bar element parallel to electric field, (d) cross element and (e) ring element. The golden arrows show the polarization of electric field, while the blue body presents silicon. The structure is upside-down to show the shapes clearly. The silver substrate is therefore omitted in these sketches. A sketch with metal included is shown in Figure 7.13.

### 7.5.2 Numerical analysis

Here we try to boost absorption by novel design of scattering structure below the thin-film silicon layer to improve the performance via plasmonic behavior. As recent development of plasmonics has inspired researchers to use metal to harness the propagation of light for solar energy concentration, the key target is to exploit the redirecting ability of plasmonic structure, while maintaining acceptable operation

bandwidth. To achieve this, one needs surface features to tune the random, broad-band sunlight more similar to an in-plane waveguide mode. This texture-facilitated coupling process will give more freedom for beam-redirecting, because certain plasmonic configurations support low-loss sharp turn.

The pioneered work of this approach [194] has given 2-D numerical results with conceptual 3-D layouts included. The prototype not only gives competent results of absorption enhancement, but also provides a platform to develop new designs. While the original calculation is limited to 2-D, it is necessary to perform 3-D analysis based on plane-wave excitation to better understand the process of light absorption. Here we use the full-vectorial numerical method to design metal scattering source, in pursuit of steady and significant improvement over plain silicon. To simulate the proposed prototype, we have used finite-difference time-domain (FDTD) method to model the interaction between a broad-band plane wave and the PV shell. The absorption in the same unit with power can be easily retrieved in FDTD simulation. The conventional and reliable way to evaluate the absorption comes from taking the divergence of Poynting vector inside the active region (in our case inside the silicon thin-film). This can be simplified further by considering  $Abs(\omega) = \nabla \cdot (\frac{1}{2} real(\overline{E(\omega)} \times \overline{H(\omega)}) = \frac{1}{2} \omega |\overline{E(\omega)}|^2 Im(\epsilon_{Silicon})$  . All parameters in the equation above can be accessed from FDTD simulation results. A broadband simulation is usually needed, and the contribution from different wavelengths can be resolved from AM 1.5 [215].

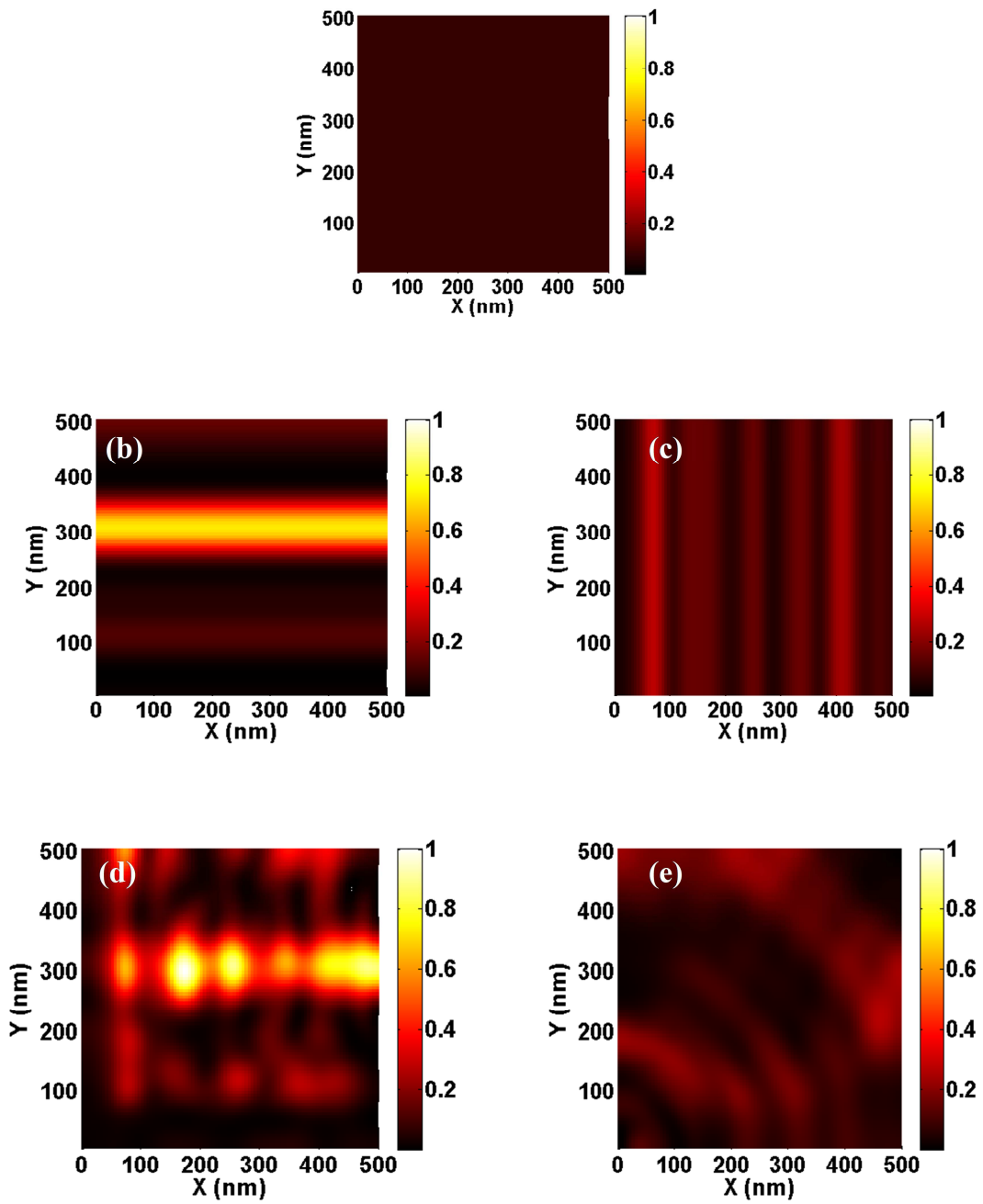


**Figure 7.8** Absorption profiles of topview (1/4 of the total area) at 50 nm above the boundary between silicon and silver for (a) plain silver, (b) bar element extended normal to the electric field, (c) bar element parallel to the electric field, (d) cross element and (e) ring element.

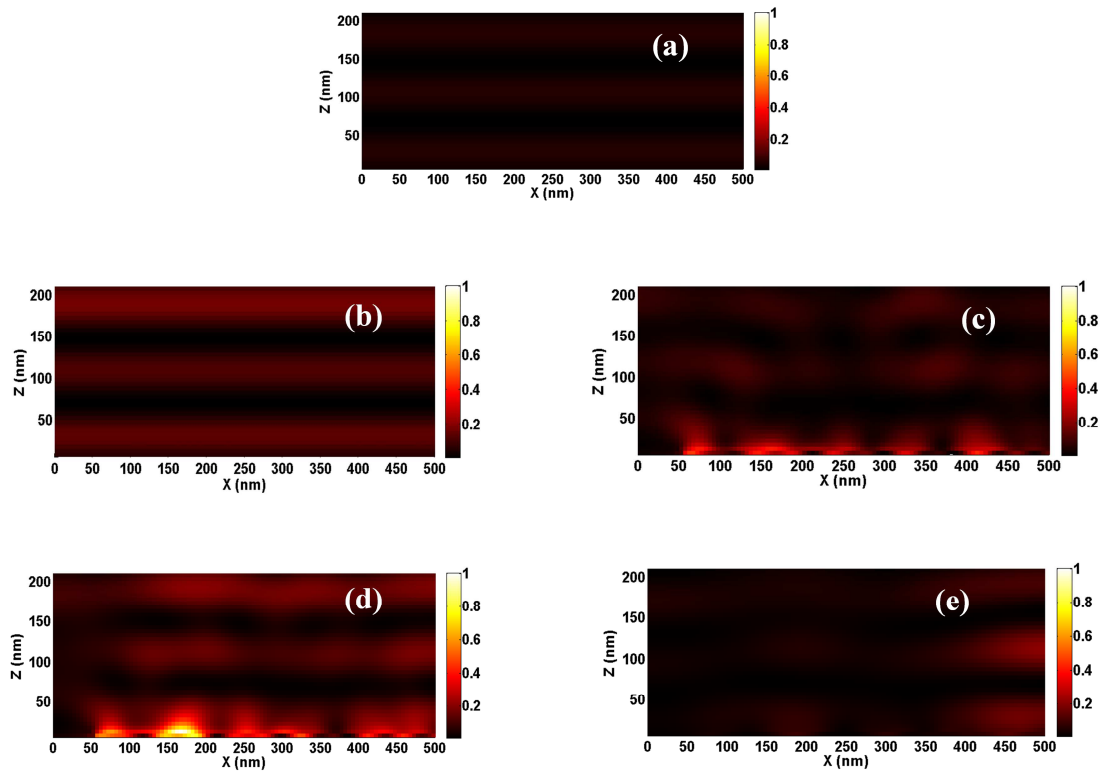


**Figure 7.9** Absorption profiles of side view at  $y=0$  (half of the total area) for (a) plain silver, (b) bar element extended normal to the electric field, (c) bar element parallel to the electric field, (d) cross element and (e) ring element.

We have performed several 3-D FDTD calculations for a number of different scattering sources (Figure 7.7) below silicon film to verify the absorption enhancement coming from plasmonic behavior. The absorption profiles are plotted for comparison as shown in Figure 7.8 - Figure 7.10, followed by the calculated enhancement factor (normalized to the absorption from plain silicon) versus wavelength (Figure 7.11). They show clearly the amount of energy absorbed by the silicon thin-film, and its dependence on the polarization. They also show that the ‘bar’ element (with the electric field going across the bar, not along), and also the ‘cross’ element, have significant surface waves’ contribution. This is quite expected after previous study of surface waves excited from

nano-size slits [59] [63], which explained how the orientation of nano-size slit determines the efficiency of power coupling from free space to surface waves. In the bar element case, each small segment of the whole bar can be regarded as a nano-slit that effectively ‘incouples’ plane wave into surface wave. It is also shown that the ‘cross’ element gives higher absorption than any other displayed configurations for most wavelengths (Figure 7.11).

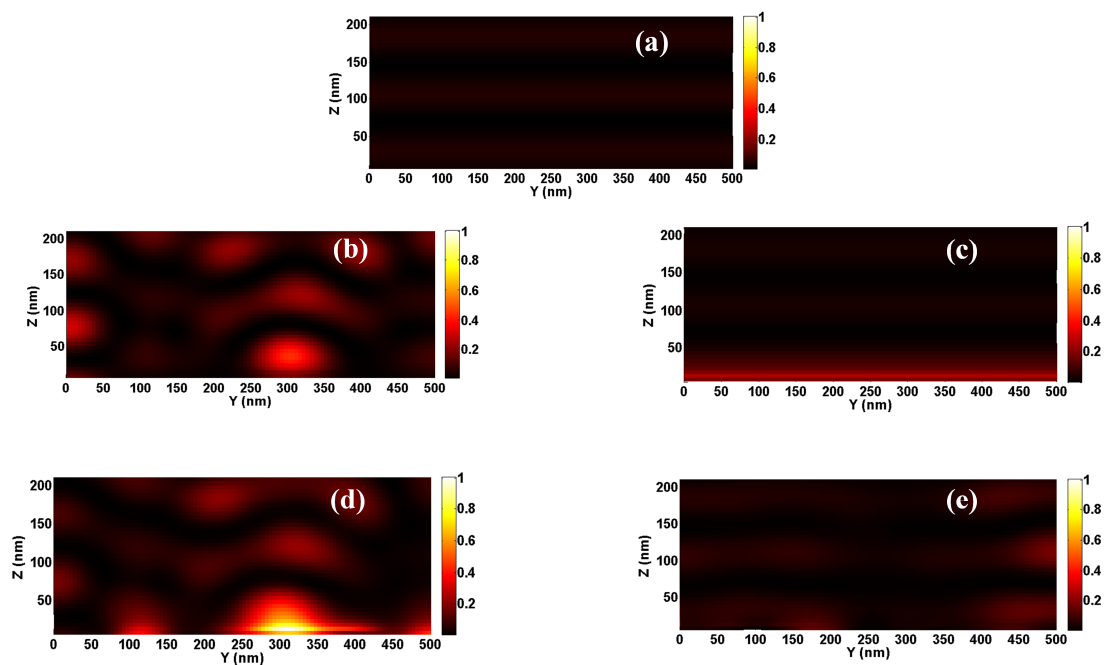


**Figure 7.10** Absorption profiles of side view at  $x=0$  for (a) plain silver, (b) bar element extended normal to the electric field, (c) bar element parallel to the electric field, (d) cross element and (e) ring element.

Based on these 3-D results, new designs can be initiated to improve the performance of bar element, with at least two apparent approaches:

- (1) Combine bottom features with front ‘islands’ to ‘double’ the enhancement.
- (2) Re-design the back scattering pattern for better light harvesting.

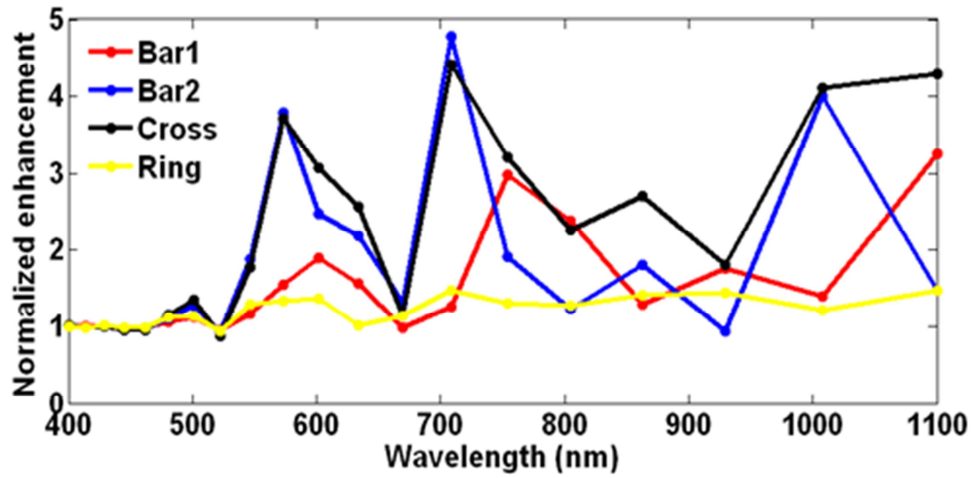


**Figure 7.11** Normalized enhancement ratio of 4 different scattering methods. Note that the ‘Bar1’ curve is related to the structure of Figure 7.7 (b), while the ‘Bar2’ curve to Figure 7.7 (c).

Regarding the simulation setup, two concerns are worth mentioning. The first is about the lateral boundary of simulation region. Since we are more interested in the behavior of a single scattering source, it is possible to only simulate one scattering source by using periodic boundary condition. But since solar rays will be random mixtures of all, the way to arrange single scattering source into periodic or random array is also crucial. If the scattering sources are periodically arrayed, a parameter scan of the periodicity is necessary to optimize the performance. The second concern is on the role of polarization. For the 2-D calculations found at [194] and other relevant literatures, the polarization is oriented in the favored direction for surface plasmon waves. While previous simulation favors the ‘cross’ shape that gives sufficient scattering into surface waves, the random nature for polarization of sunlight should not be neglected. At least two ways to arrange the cross element are possible (Figure 7.12), laying scattering elements out either orderly or randomly. The preferred layout will need to be verified on experimental level.

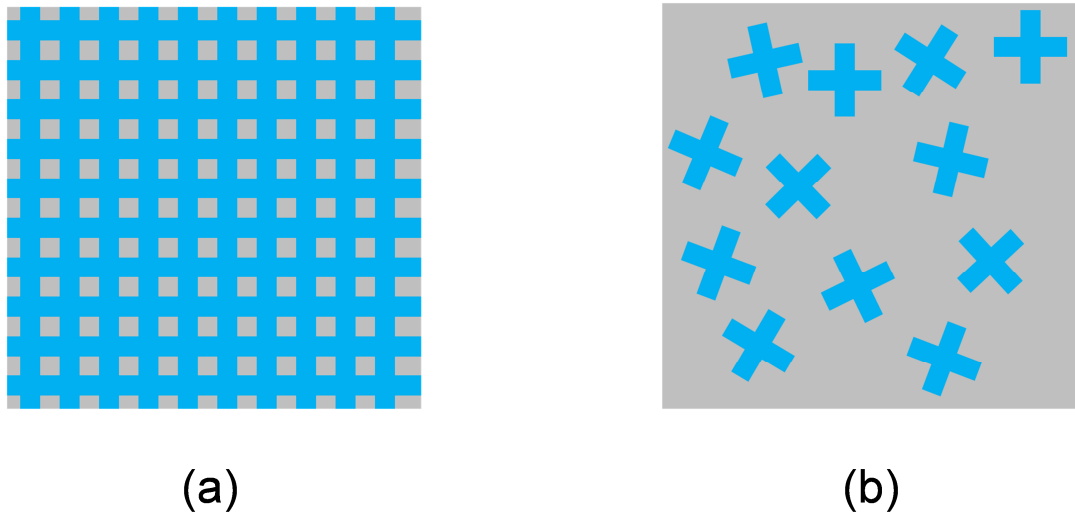


**Figure 7.12** Two schemes to lay out the scattering sources. (a) “Cross” elements in a crystal-like array; (b) “Cross” elements in random.

### 7.5.3 Future Plan

Following the numerical results reported above, we can start from theoretical study combined with numerical modeling and optimization, and then proceed to demonstration and experiments.

Firstly, it is necessary to look through all the designs that can incorporate plasmonic effect based on the back scattering platform. For example, the concept of plasmonic antenna [125] [216] can provide a better insight into the scattering from metal textures. One possible approach is to start from the factor of polarization, and then to a formalism of the matching problem as in antenna theory. From the direct coupling concept between optical mode and plasmonic mode [119], it is possible to figure out novel and efficient coupling schemes that can best fit into thin-film PV modules.

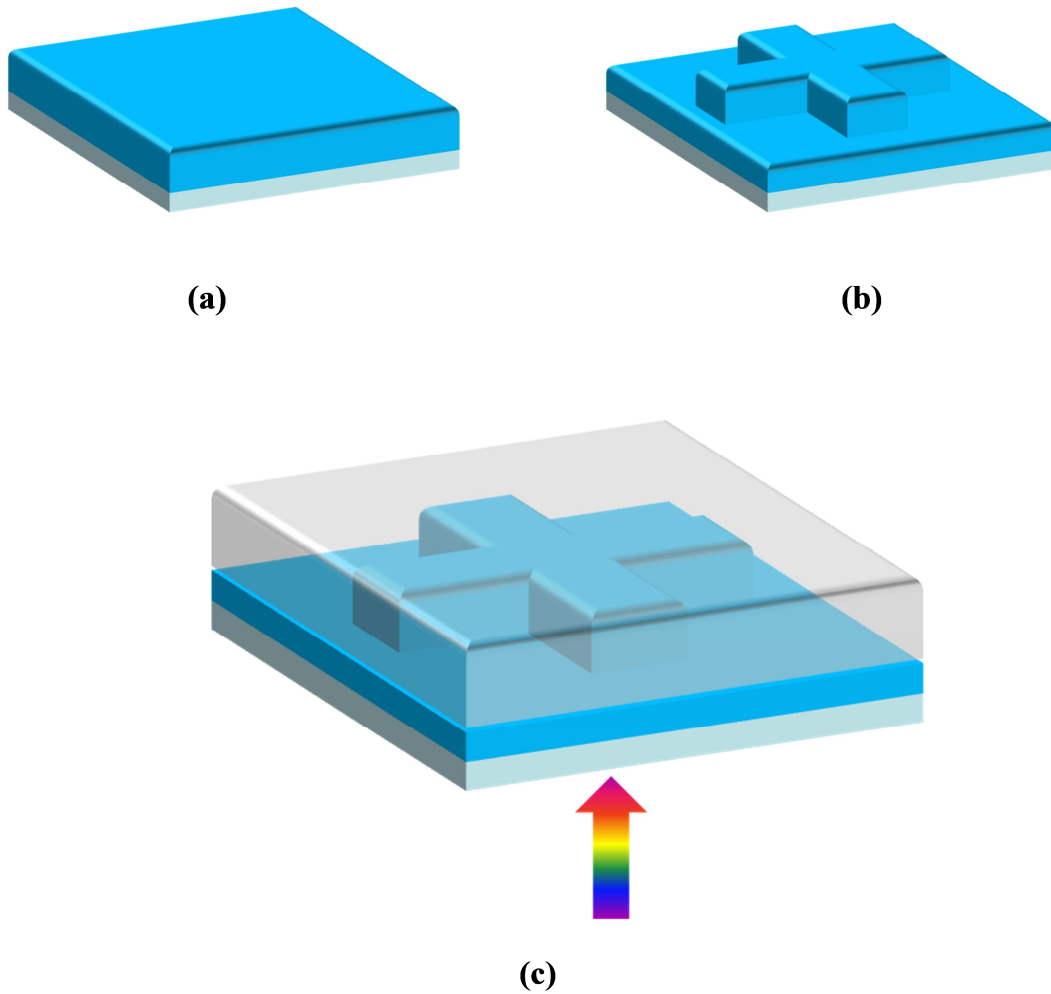


**Figure 7.13** (a) Amorphous silicon deposition on glass, (b) Silicon patterning, (c) Metal evaporation on top of silicon. Sunlight input from glass (front) side. The upside-down looking is for illustration purpose only.

With better understanding into the physics related to solar radiation and plasmonic scattering source, it is still crucial to perform 3-D FDTD simulation for better designs. This is to be followed by the fabrication and demonstration of these new designs.

The first step of measurement is to make optical transmission/reflection measurement on PV substrates. Optical measurement is straightforward with results easy to understand, which is good for qualitative evaluation of a prototype and making primitive optimization. For simplicity, straightforward fabrication scheme can be used.

The fabrication process of this sample can be initialized on a glass wafer piece, followed by deposition of amorphous silicon as absorption layer. The silicon can then be patterned using RIE to form the profile of scattering source (Figure 7.13). Finally the evaporation of metal will cover the whole silicon area and at the same time form the contact. The measurement will be performed to calculate the reflection from the sample using spectroradiometer when illuminated by simulated sunlight either from basic illumination system or from more complex and accurate setup. The results can then be normalized to that without any surface scatterers. It is expected to observe a decreased back reflection from the front side when designed rear contacts are used, because more power will be directed to in-plane propagation.

Secondly, the electrical performance of the sample can be characterized by a combination of illumination system and electrical probe stations. For electrical measurement, the top contact must be realized. It is possible to choose the single-sided electrodes setup upon the design progress available, when both P and N type region for electrodes are formed on rear side. With all the above accomplished, an overall performance evaluation regarding the conversion efficiency can be done. The enhancement from the surface feature design of rear contacts can therefore be obtained according to the actual electric performance.

## **7.6 Conclusions**

We have discussed the advantages of integrating plasmonic devices into optical integrated circuitry or PV energy systems. Two examples of active plasmonics for communications systems are given to show the promising future of on-chip plasmonic modules, in the context of low-power modulation and fast sensing. The modulation

scheme is expected to be developed on active materials such as graphene, and the preliminary fabrications results are presented. The near-infrared sensing utilized a tunneling diode formed by a plasmonic waveguide cavity. An equivalent circuit is used to estimate the performance, while a few proposed structures are shown. This is then followed by exploring the possibility to integrate plasmonic scatterers into solar cell substrate to enhance the light absorption efficiency. The plasmonic back-scattering structure has been numerical verified as a promising candidate to further improve the performance of silicon-based thin-film PV systems.

---

## 8 CONCLUSIONS

---

In this dissertation, subwavelength plasmonics have been studied and explored analytically, numerically and experimentally for various potential applications, such as optical communications, data storage, subwavelength imaging, optical sensing, etc. As an important branch recently established within the family of photonics, plasmonics has the potential to overcome critical limitations of traditional photonics such as diffraction-limit, while maintaining the attractive features of optics such as fast operation. The research covered in this dissertation tried to address several complex issues on different aspects of nanoplasmonics, with a concentration on the integration of plasmonic features to optical subsystems, so as to make the interesting features of plasmonics more effectively realized.

### 8.1 Compact and efficient plasmonic coupling

In Chapters 2-4, the monolithic launching and excitation of SPP waves are treated as the key issue. All three chapters design integrated plasmonic devices with simple and straightforward interface for efficient coupling between optical and plasmonic domains, and concentrate on exploiting the small-footprint plasmonic modules as plasmonic junctions or optical focusing devices. Specifically, experimental validation reported in Chapter 4 is one of the first demonstrations of monolithic 3-D MIM plasmonic waveguides with deep subwavelength scale (sub-100nm in transverse directions for 1550 nm light) waveguiding, based on the numerical design and optimization presented in Chapter 3.

All the plasmonic devices presented in Chapters 2-4 use the direct coupling scheme for plasmonic excitation. This approach harmonizes the motivation of building plasmonic features into compact optical structures and platforms. Numerical simulations using the FDTD method have helped to verify the possibility of expanding 2-D direct coupling to 3-D, and integrated devices are demonstrated on the versatile silicon-on-insulator (SOI) substrate. The reported prototypes are not only integrated devices based on direct coupling, but also examples of plasmonic modules on top of the dominating SOI platform for on-chip optical circuitry. The coupling and integration approach mentioned here is a competent candidate for development and deployment of future plasmonic building blocks.

The full potentials of the reported plasmonic devices in Chapters 2-4 have yet been fully unleashed. Specifically, the on-chip nanofocusing achieved in the related chapters could contribute either as a plasmonic junction in the middle of an optical path, or a standalone plasmonic probe to sample or radiate miniscule energy. The near-field radiation of plasmonic heads can produce unparalleled confinement of electromagnetic wave and be invaluable for nanophotonics. The confinement is so extreme that advanced near-field measurement such as NSOM is usually required to characterize the radiation. As discussed in Chapter 4, radiation in such small scale has already been utilized for next-generation magnetic recording. It is also possible to foresee the plasmonic heads themselves as delicate detecting channels as part of future characterization methods.

The work reported in Chapters 2-4 above are among the first a few discoveries made for compact plasmonic coupling. **The demonstration of direct coupling and mode transformation delivers one of the first prototypes for efficient plasmonic**

**couplers to squeeze near-infrared (1550-nm) light into sub-100nm scale in the transverse direction.**

## **8.2 Spoof plasmonics and indefinite metamaterials**

Chapters 5 and 6 explored the possibility of utilizing periodic structures for subwavelength waveguiding platform as a type of indefinite metamaterial, with a concentration on the expansion of conventional frequency range predetermined by plasmonic metals. Chapter 5 followed the designer surface plasmon approach to push the frequency limit of spoof plasmonics to THz and even GHz regimes. Chapter 6 explored the tunability of periodic multilayered stacks for engineered, propagating surface waves with arbitrary surface plasmon frequency. Effective medium theory, transfer-matrix method, FDTD simulation and Kretschmann ATIR experiments have been sought to verify the shifting of surface plasmon frequency.

The concept behind Chapter 5 and 6 is the indefinite metamaterials and their tunable electromagnetic (EM) property, for the common purpose of engineering and tailoring the EM behavior of carefully designed structures based on traditional materials. The simulation approach mentioned in Chapter 5 helps to complete one of the first demonstrations of domino-type surface plasmon waveguides in GHz spectra. The design has also been shown to be highly scalable especially in THz and GHz spectra.

The metallic grating designed for domino surface plasmons is one example of broadening the application range of plasmonics. The surface waves are engineered to have a subwavelength evanescent tail, which is totally different to the field profile on top of a flat metal surface, especially in THz spectra. Gratings can be thought of as surface corrugations laterally modulating the materials in plane, providing one way of designing

indefinite metamaterials. It is therefore highly natural to also think of the possibility to periodically modulate the material in vertical direction, as elaborated in Chapter 6 towards the metal-dielectric multilayer. After thorough theoretical analysis, the concept of effective surface plasmon frequency for a meta-metal was proposed and quantified. Numerical simulations and experimental efforts have proved this analysis to be very efficient in designing multilayers for shifting the actual (effective) surface plasmon frequency of this type of multilayer composite or meta-metal. One possible application to be explored in near future is for development of surface plasmon resonance sensors. More work can be done to expand the 2-D analysis to 3-D, by including surface patterns for lateral mode confinement (in plane).

The results and especially the calculation approach shown in Chapter 5 have paved the way for many successful experiments performed in the author's lab. **Chapter 6 proposed for the first time the conception of effective surface plasmon frequency and applied the theory to multilayered meta-metal in an elegant and efficient manner.** It has also suggested a practical optimization possibility for optical sensing using surface plasmon resonance.

### **8.3 Active plasmonics and future work**

Chapter 7 discussed the future work based on previous chapters, especially from an active plasmonics' point of view. Preliminary fabrication results for a field-effect graphene-based modulator are presented as the platform for graphene-based active devices, followed by the theoretical analysis of an integrated tunneling diode that might be developed into a near-infrared waveguide detector. The possibility to utilize the plasmonic-assisted light harvesting in novel solar cell design is also discussed. While

further experimental work is necessary to demonstrate these concepts, the discussion and preliminary results given in this chapter has depicted a promising future of integrated plasmonics.

---

## 9 REFERENCES

---

- [1] ITRS 2007. Available: <http://www.itrs.net/Links/2007ITRS/Home2007.htm>
- [2] D. A. B. Miller, "Rationale and challenges for optical interconnects to electronic chips," *Proceedings of the IEEE*, vol. 88, no. 6, pp. 728-749, Jun. 2000.
- [3] Y. A. Vlasov, M. O'Boyle, H. F. Hamann, and S. J. McNab, "Active control of slow light on a chip with photonic crystal waveguides," *Nature*, vol. 438, no. 7064, pp. 65-69, Nov. 2005.
- [4] J. Tominaga, C. Mihalcea, D. Buchel, H. Fukuda, T. Nakano, N. Atoda, H. Fuji, and T. Kikukawa, "Local plasmon photonic transistor," *Applied Physics Letters*, vol. 78, no. 17, pp. 2417-2419, Apr. 2001.
- [5] E. Yablonovitch, "Inhibited spontaneous emission in Solid-State physics and electronics," *Phys. Rev. Lett.*, vol. 58, no. 20, pp. 2059-2062, May 1987.
- [6] S. John, "Strong localization of photons in certain disordered dielectric superlattices," *Phys. Rev. Lett.*, vol. 58, no. 23, pp. 2486-2489, Jun. 1987.
- [7] G. T. Reed, "Device physics: The optical age of silicon," *Nature*, vol. 427, no. 6975, pp. 595-596, Feb. 2004.
- [8] A. Liu, R. Jones, L. Liao, D. Samara-Rubio, D. Rubin, O. Cohen, R. Nicolaescu, and M. Paniccia, "A high-speed silicon optical modulator based on a metal-oxide-semiconductor capacitor," *Nature*, vol. 427, no. 6975, pp. 615-618, Feb. 2004.
- [9] H. Rong, A. Liu, R. Jones, O. Cohen, D. Hak, R. Nicolaescu, A. Fang, and M. Paniccia, "An all-silicon raman laser," *Nature*, vol. 433, no. 7023, pp. 292-294, Jan. 2005.
- [10] H. Rong, R. Jones, A. Liu, O. Cohen, D. Hak, A. Fang, and M. Paniccia, "A continuous-wave raman silicon laser," *Nature*, vol. 433, no. 7027, pp. 725-728, Feb. 2005.
- [11] Q. Xu, B. Schmidt, S. Pradhan, and M. Lipson, "Micrometre-scale silicon electro-optic modulator," *Nature*, vol. 435, no. 7040, pp. 325-327, May 2005.

- [12] V. R. Almeida, C. A. Barrios, R. R. Panepucci, and M. Lipson, "All-optical control of light on a silicon chip," *Nature*, vol. 431, no. 7012, pp. 1081-1084, Oct. 2004.
- [13] S. Luryi, A. Kastalsky, and J. C. Bean, "New infrared detector on a silicon chip," *Electron Devices, IEEE Transactions on*, vol. 31, no. 9, pp. 1135-1139, Sep. 1984.
- [14] J. Liu, M. Beals, A. Pomerene, S. Bernardis, R. Sun, J. Cheng, L. C. Kimerling, and J. Michel, "Waveguide-integrated, ultralow-energy GeSi electro-absorption modulators," *Nature Photonics*, vol. 2, no. 7, pp. 433-437, May 2008.
- [15] L. Colace, G. Masini, G. Assanto, H.-C. Luan, K. Wada, and L. C. Kimerling, "Efficient high-speed near-infrared ge photodetectors integrated on si substrates," *Applied Physics Letters*, vol. 76, no. 10, pp. 1231-1233, Mar. 2000.
- [16] E. N. Economou, "Surface plasmons in thin films," *Physical Review*, vol. 182, no. 2, pp. 539-554, Jun. 1969.
- [17] R. H. Ritchie, "Surface plasmons in solids," *Surface Science*, vol. 34, no. 1, pp. 1-19, Jan. 1973.
- [18] M. I. Stockman, "Nanoplasmonics: past, present, and glimpse into future," *Opt. Express*, vol. 19, no. 22, pp. 22 029-22 106, Oct. 2011.
- [19] M. A. Noginov, G. Zhu, A. M. Belgrave, R. Bakker, V. M. Shalaev, E. E. Narimanov, S. Stout, E. Herz, T. Suteewong, and U. Wiesner, "Demonstration of a spaser-based nanolaser." *Nature*, vol. 460, no. 7259, pp. 1110-1112, Aug. 2009.
- [20] D. Dai and S. He, "A silicon-based hybrid plasmonic waveguide with a metal cap for a nano-scale light confinement," *Opt. Express*, vol. 17, no. 19, pp. 16 646-16 653, Sep. 2009.
- [21] W. Nomura, M. Ohtsu, and T. Yatsui, "Nanodot coupler with a surface plasmon polariton condenser for optical far/near-field conversion," *Applied Physics Letters*, vol. 86, no. 18, pp. 181 108+, 2005.
- [22] C. Scales, I. Breukelaar, and P. Berini, "Surface-plasmon schottky contact detector based on a symmetric metal stripe in silicon." *Optics Letters*, vol. 35, no. 4, pp. 529-531, Feb. 2010.
- [23] K. F. MacDonald and N. I. Zheludev, "Active plasmonics: current status," *Laser & Photon. Rev.*, vol. 4, no. 4, pp. 562-567, 2010.

- [24] H. A. Atwater, "The promise of plasmonics," *Sci. Am.*, vol. 296, no. 4, pp. 56-62, Apr. 2007.
- [25] B. E. A. Saleh and M. C. Teich, "Electromagnetic Optics," in *Fundamentals of Photonics*, 2nd ed. Hoboken, NJ: Wiley-Interscience, 2007, pp. 291–293.
- [26] E. Abbe, "Beiträge zur theorie des mikroskops und der mikroskopischen wahrnehmung," *Archiv für Mikroskopische Anatomie*, vol. 9, no. 1, pp. 413-418, Dec. 1873.
- [27] Z. Ruan and M. Qiu, "Enhanced transmission through periodic arrays of subwavelength holes: The role of localized waveguide resonances," *Physical Review Letters*, vol. 96, no. 23, pp. 233 901+, Jun. 2006.
- [28] R. F. Oulton, V. J. Sorger, D. A. Genov, D. F. P. Pile, and X. Zhang, "A hybrid plasmonic waveguide for subwavelength confinement and long-range propagation," *Nature Photonics*, vol. 2, no. 8, pp. 496-500, Jul. 2008.
- [29] M. Silveirinha and N. Engheta, "Tunneling of electromagnetic energy through subwavelength channels and bends using  $\epsilon$ -near-zero materials," *Physical Review Letters*, vol. 97, pp. 157 403+, Oct. 2006.
- [30] K. Kim, "On the evolution of PON-based FTTH solutions," *Information Sciences*, vol. 149, no. 1-3, pp. 21-30, Jan. 2003.
- [31] M. Rothschild, "A roadmap for optical lithography," *Opt. Photon. News*, vol. 21, no. 6, pp. 26-31, Jun. 2010.
- [32] J. Eid, A. Fehr, J. Gray, K. Luong, J. Lyle, G. Otto, P. Peluso, D. Rank, P. Baybayan, B. Bettman, A. Bibillo, K. Bjornson, B. Chaudhuri, F. Christians, R. Cicero, S. Clark, R. Dalal, A. deWinter, J. Dixon, M. Foquet, A. Gaertner, P. Hardenbol, C. Heiner, K. Hester, D. Holden, G. Kearns, X. Kong, R. Kuse, Y. Lacroix, S. Lin, P. Lundquist, C. Ma, P. Marks, M. Maxham, D. Murphy, I. Park, T. Pham, M. Phillips, J. Roy, R. Sebra, G. Shen, J. Sorenson, A. Tomaney, K. Travers, M. Trulson, J. Vieceli, J. Wegener, D. Wu, A. Yang, D. Zaccarin, P. Zhao, F. Zhong, J. Korlach, and S. Turner, "Real-Time DNA sequencing from single polymerase molecules," *Science*, vol. 323, no. 5910, pp. 133-138, Jan. 2009.
- [33] W. A. Challener, C. Peng, A. V. Itagi, D. Karns, W. Peng, Y. Peng, X. Yang, X. Zhu, N. J. Gokemeijer, Y. T. Hsia, G. Ju, R. E. Rottmayer, M. A. Seigler, and E. C. Gage, "Heat-assisted magnetic recording by a near-field transducer with efficient optical energy transfer," *Nature Photonics*, vol. 3, no. 4, pp. 220-224, Mar. 2009.

- [34] M. L. Brongersma and P. G. Kik, "Surface Plasmon Nanophotonics," in *Springer Series in Optical Sciences*, Vol. 131, Berlin/Heidelberg, Germany: Springer, 2007
- [35] T. W. Ebbesen, H. J. Lezec, H. F. Ghaemi, T. Thio, and P. A. Wolff, "Extraordinary optical transmission through sub-wavelength hole arrays," *Nature*, vol. 391, no. 6668, pp. 667-669, Feb. 1998.
- [36] C. Kittel, *Introduction to Solid State Physics*. New York: Wiley, 1989.
- [37] B. E. A. Saleh and M. C. Teich, "Electromagnetic Optics," in *Fundamentals of Photonics*, 2nd ed. Hoboken, NJ: Wiley-Interscience, 2007, pp. 181–183.
- [38] M. A. Ordal, R. J. Bell, J. Alexander, L. L. Long, and M. R. Querry, "Optical properties of fourteen metals in the infrared and far infrared: Al, Co, Cu, Au, Fe, Pb, Mo, Ni, Pd, Pt, Ag, Ti, V, and W," *Appl. Opt.*, vol. 24, no. 24, pp. 4493-4499, Dec. 1985.
- [39] E. D. Palik, *Handbook of Optical Constants of Solids*. Orlando, GA: Academic Press, 1985.
- [40] J. D. Joannopoulos, S. G. Johnson and J. N. Winn, *Photonic crystals: molding the flow of light*. Princeton, NJ: Princeton University Press, 2008.
- [41] N. Engheta and R. W. Ziolkowski, *Metamaterials: physics and engineering explorations*. New York: Wiley-IEEE, 2006.
- [42] S. A. Maier, *Plasmonics: Fundamentals and Applications*. New York, Springer, 2007.
- [43] R. Gordon, "Light in a subwavelength slit in a metal: Propagation and reflection," *Physical Review B (Condensed Matter and Materials Physics)*, vol. 73, no. 15, pp. 153 405+, 2006.
- [44] J. A. Dionne, L. A. Sweatlock, H. A. Atwater, and A. Polman, "Plasmon slot waveguides: Towards chip-scale propagation with subwavelength-scale localization," *Physical Review B*, vol. 73, no. 3, pp. 035 407+, Jan. 2006.
- [45] S. I. Bozhevolnyi, V. S. Volkov, E. Devaux, J.-Y. Laluet, and T. W. Ebbesen, "Channel plasmon subwavelength waveguide components including interferometers and ring resonators," *Nature*, vol. 440, no. 7083, pp. 508-511, Mar. 2006.
- [46] G. Veronis and S. Fan, "Guided subwavelength plasmonic mode supported by a slot in a thin metal film," *Opt. Lett.*, vol. 30, pp. 3359-3361, Dec. 2005.

- [47] E. Feigenbaum and M. Orenstein, "Modeling of complementary (void) plasmon waveguiding," *J. Lightwave Technol.*, vol. 25, no. 9, pp. 2547-2562, Sep. 2007.
- [48] G. Veronis and S. Fan, "Bends and splitters in metal-dielectric-metal subwavelength plasmonic waveguides," *Applied Physics Letters*, vol. 87, no. 13, pp. 131 102+, 2005.
- [49] Ş. E. Kocabaş, G. Veronis, D. A. B. Miller, and S. Fan, "Modal analysis and coupling in metal-insulator-metal waveguides," *Physical Review B*, vol. 79, no. 3, pp. 035 120+, Jan. 2009.
- [50] R. Charbonneau, C. Scales, I. Breukelaar, S. Fafard, N. Lahoud, G. Mattiussi, and P. Berini, "Passive integrated optics elements based on Long-Range surface plasmon polaritons," *J. Lightwave Technol.*, vol. 24, no. 1, pp. 477+, Jan. 2006.
- [51] T. Nikolajsen, K. Leosson, and S. I. Bozhevolnyi, "Surface plasmon polariton based modulators and switches operating at telecom wavelengths," *Appl. Phys.s Lett.*, vol. 85, no. 24, pp. 5833-5835, 2004.
- [52] J. A. Dionne, H. J. Lezec, and H. A. Atwater, "Highly confined photon transport in subwavelength metallic slot waveguides," *Nano Letters*, vol. 6, no. 9, pp. 1928-1932, Sep. 2006.
- [53] L. Chen, J. Shakya, and M. Lipson, "Subwavelength confinement in an integrated metal slot waveguide on silicon," *Opt. Lett.*, vol. 31, pp. 2133-2135, Jul. 2006.
- [54] J. A. Dionne, K. Diest, L. A. Sweatlock, and H. A. Atwater, "PlasMOSstor: A Metal-Oxide-si field effect plasmonic modulator," *Nano Letters*, vol. 9, no. 2, pp. 897-902, Feb. 2009.
- [55] W. Cai, J. S. White, and M. L. Brongersma, "Compact, High-Speed and Power-Efficient electrooptic plasmonic modulators," *Nano Letters*, vol. 9, no. 12, pp. 4403-4411, Dec. 2009.
- [56] M. J. Levene, J. Korlach, S. W. Turner, M. Foquet, H. G. Craighead, and W. W. Webb, "Zero-Mode waveguides for Single-Molecule analysis at high concentrations," *Science*, vol. 299, no. 5607, pp. 682-686, Jan. 2003.
- [57] H. Lezec and T. Thio, "Diffracted evanescent wave model for enhanced and suppressed optical transmission through subwavelength hole arrays," *Opt. Express*, vol. 12, no. 16, pp. 3629-3651, Aug. 2004.
- [58] T. Thio, "A bright future for subwavelength light sources," *American Scientist*, vol. 94, no. 1, pp. 40+, 2006.

- [59] D. Pacifici, H. J. Lezec, L. A. Sweatlock, R. J. Walters, and H. A. Atwater, “Universal optical transmission features in periodic and quasiperiodic hole arrays,” *Opt. Express*, vol. 16, no. 12, pp. 9222-9238, Jun. 2008.
- [60] R. Merlin, “Radiationless electromagnetic interference: Evanescent-Field lenses and perfect focusing,” *Science*, vol. 317, no. 5840, pp. 927-929, Aug. 2007.
- [61] F. J. Garcia-Vidal, S. G. Rodrigo, and L. Martín-Moreno, “Foundations of the composite diffracted evanescent wave model,” *Nat. Phys.*, vol. 2, no. 12, p. 790, Dec. 2006.
- [62] L. Chen, J. T. Robinson, and M. Lipson, “Role of radiation and surface plasmon polaritons in the optical interactions between a nano-slit and a nano-groove on a metal surface,” *Opt. Express*, vol. 14, no. 26, pp. 12 629-12 636, Dec. 2006.
- [63] D. Pacifici, H. J. Lezec, H. A. Atwater, and J. Weiner, “Quantitative determination of optical transmission through subwavelength slit arrays in ag films: Role of surface wave interference and local coupling between adjacent slits,” *Physical Review B*, vol. 77, no. 11, pp. 115 411+, Mar. 2008.
- [64] G. Veronis and S. Fan, “Theoretical investigation of compact couplers between dielectric slabwaveguides and two-dimensional metal-dielectric-metal plasmonicwaveguides,” *Opt. Express*, vol. 15, no. 3, pp. 1211-1221, Feb. 2007.
- [65] R. A. Wahsheh, Z. Lu, and M. A. G. Abushagur, “Nanoplasmonic couplers and splitters,” *Opt. Express*, vol. 17, no. 21, pp. 19 033-19 040, Oct. 2009.
- [66] C. A. Balanis, *Antenna theory: analysis and design*, 3rd Ed. Hoboken, NJ: Wiley, 2005.
- [67] A. Sommerfeld, “Propagation of waves in wireless telegraphy,” *Ann. Phys.*, vol. 81, pp. 1367–1153, 1926.
- [68] J. B. Pendry, L. Martín-Moreno, and F. J. Garcia-Vidal, “Mimicking surface plasmons with structured surfaces,” *Science*, vol. 305, no. 5685, pp. 847-848, Aug. 2004.
- [69] S. Maier, S. Andrews, L. Martín-Moreno, and F. García-Vidal, “Terahertz surface Plasmon-Polariton propagation and focusing on periodically corrugated metal wires,” *Physical Review Letters*, vol. 97, no. 17, pp. 176 805+, Oct. 2006.
- [70] D. Martín-Cano, M. L. Nesterov, A. I. Fernandez-Dominguez, F. J. Garcia-Vidal, L. Martín-Moreno, and E. Moreno, “Domino plasmons for subwavelengthterahertz circuitry,” *Opt. Express*, vol. 18, no. 2, pp. 754-764, Jan. 2010.

- [71] W. Zhao, O. M. Eldaiki, R. Yang, and Z. Lu, “Deep subwavelength waveguiding and focusing based on designer surface plasmons,” *Opt. Express*, vol. 18, no. 20, pp. 21 498-21 503, Sep. 2010.
- [72] D. Bergman, “The dielectric constant of a composite material—A problem in classical physics,” *Physics Reports*, vol. 43, no. 9, pp. 377-407, Jul. 1978.
- [73] W. Cai, D. A. Genov, and V. M. Shalaev, “Superlens based on metal-dielectric composites,” *Physical Review B*, vol. 72, no. 19, pp. 193 101+, Nov. 2005.
- [74] D. R. Lide, *CRC handbook of chemistry and physics*. Boca Raton, FL: CRC Press, 2004.
- [75] MicroChem Corp. [Online]. Available: <http://www.microchem.com>
- [76] Cornell Nanofabrication Facility. (2012, April 20). *Photolithography Resist Processes and Capabilities* [Online]. Available: [http://www.cnf.cornell.edu/cnf\\_process\\_photo\\_resists.html](http://www.cnf.cornell.edu/cnf_process_photo_resists.html)
- [77] R. A. Soref, S.-Y. Cho, W. Buchwald, and R. E. Peale, “Silicon Plasmonic Waveguides,” in *Silicon Photonics for Telecommunications and Biomedical Applications*, B. Jalali and S. Fathpour, Eds. UK: Taylor and Francis, 2010.
- [78] PVD 75 Sputter Deposition from Kurt J. Lesker by CNF [Online]. Available: [http://www.cnf.cornell.edu/cnf5\\_tool.taf?\\_function=detail&eq\\_id=156](http://www.cnf.cornell.edu/cnf5_tool.taf?_function=detail&eq_id=156)
- [79] P. R. West, S. Ishii, G. V. Naik, N. K. Emani, V. M. Shalaev, and A. Boltasseva, “Searching for better plasmonic materials,” *Laser & Photon. Review.*, vol. 4, no. 6, pp. 795-808, Mar. 2010.
- [80] D. R. Andersen, “Graphene-based long-wave infrared TM surface plasmon modulator,” *J. Opt. Soc. Am. B*, vol. 27, no. 4, pp. 818-823, Apr. 2010.
- [81] F. H. L. Koppens, D. E. Chang, and F. J. García de Abajo, “Graphene plasmonics: A platform for strong Light–Matter interactions,” *Nano Letters*, vol. 11, no. 8, pp. 3370-3377, Jul. 2011.
- [82] J. T. Kim and S.-Y. Choi, “Graphene-based plasmonic waveguides for photonic integrated circuits,” *Opt. Express*, vol. 19, no. 24, pp. 24 557-24 562, Nov. 2011.
- [83] X. Li, Y. Zhu, W. Cai, M. Borysiak, B. Han, D. Chen, R. D. Piner, L. Colombo, and R. S. Ruoff, “Transfer of Large-Area graphene films for High-Performance transparent conductive electrodes,” *Nano Letters*, vol. 9, no. 12, pp. 4359-4363, Oct. 2009.

- [84] A. Reina, X. Jia, J. Ho, D. Nezich, H. Son, V. Bulovic, M. S. Dresselhaus, and J. Kong, "Large area, Few-Layer graphene films on arbitrary substrates by chemical vapor deposition," *Nano Letters*, vol. 9, no. 1, pp. 30-35, Dec. 2008.
- [85] A. N. Sidorov, M. M. Yazdanpanah, R. Jalilian, P. J. Ouseph, R. W. Cohn, and G. U. Sumanasekera, "Electrostatic deposition of graphene," *Nanotechnology*, vol. 18, no. 13, pp. 135 301+, Apr. 2007.
- [86] J. A. Stratton, *Electromagnetic Theory*. New York: McGraw-Hill, 1941.
- [87] G. Mie, "Beiträge zur optik trüber medien, speziell kolloidaler metallösungen," *Ann. Phys.*, vol. 330, no. 3, pp. 377-445, 1908.
- [88] A. Taflove, "Application of the Finite-Difference Time-Domain method to sinusoidal Steady-State Electromagnetic-Penetration problems," *Electromagnetic Compatibility, IEEE Trans. on*, vol. EMC-22, no. 3, pp. 191-202, Aug. 1980.
- [89] K. Yee, "Numerical solution of initial boundary value problems involving maxwell's equations in isotropic media," *Antennas and Propagation, IEEE Trans. on*, vol. 14, no. 3, pp. 302-307, May 1966.
- [90] J. Jing, *The Finite Element Method in Electromagnetics*, 2nd Ed. New York: Wiley, 2002.
- [91] J.-P. Berenger, "A perfectly matched layer for the absorption of electromagnetic waves," *J. of Computational Physics*, vol. 114, no. 2, pp. 185-200, Oct. 1994.
- [92] FDTD Solutions, Lumerical, Vancouver, <http://www.lumerical.com>
- [93] R. Yang, R. A. Wahsheh, Z. Lu, and M. A. Abushagur, "Efficient light coupling between dielectric slot waveguide and plasmonic slot waveguide," *Opt. Lett.*, vol. 35, no. 5, pp. 649-651, Mar. 2010.
- [94] S. I. Bozhevolnyi, V. S. Volkov, E. Devaux, and T. W. Ebbesen, "Channel Plasmon-Polariton guiding by subwavelength metal grooves," *Physical Review Letters*, vol. 95, no. 4, pp. 046 802+, Jul. 2005.
- [95] D. M. Koller, A. Hohenau, H. Ditlbacher, N. Galler, F. Reil, F. R. Aussenegg, A. Leitner, E. J. W. List, and J. R. Krenn, "Organic plasmon-emitting diode," *Nature Photonics*, vol. 2, no. 11, pp. 684-687, Sep. 2008.
- [96] L. Tang, S. E. Kocabas, S. Latif, A. K. Okyay, D.-S. Ly-Gagnon, K. C. Saraswat, and D. A. B. Miller, "Nanometre-scale germanium photodetector enhanced by a near-infrared dipole antenna," *Nature Photonics*, vol. 2, no. 4, pp. 226-229, Mar. 2008.

- [97] E. Verhagen, A. Polman, and L. K. Kuipers, "Nanofocusing in laterally tapered plasmonic waveguides," *Opt. Express*, vol. 16, no. 1, pp. 45-57, Jan. 2008.
- [98] A. Otto, "Excitation of nonradiative surface plasma waves in silver by the method of frustrated total reflection," *Zeitschrift für Physik A Hadrons and Nuclei*, vol. 216, no. 4, pp. 398-410, Aug. 1968.
- [99] R. H. Ritchie, E. T. Arakawa, J. J. Cowan, and R. N. Hamm, "Surface-Plasmon resonance effect in grating diffraction," *Physics Review Letters*, vol. 21, pp. 1530-1533, Nov. 1968.
- [100] K. Tanaka and M. Tanaka, "Simulations of nanometric optical circuits based on surface plasmon polariton gap waveguide," *Applied Physics Letters*, vol. 82, no. 8, pp. 1158-1160, 2003.
- [101] R. Zia, M. D. Selker, P. B. Catrysse, and M. L. Brongersma, "Geometries and materials for subwavelength surface plasmon modes," *J. Opt. Soc. Am. A*, vol. 21, no. 12, pp. 2442-2446, Dec. 2004.
- [102] F. Kusunoki, T. Yotsuya, J. Takahara, and T. Kobayashi, "Propagation properties of guided waves in index-guided two-dimensional optical waveguides," *Applied Physics Letters*, vol. 86, no. 21, pp. 2111-2114, 2005.
- [103] L. Liu, Z. Han, and S. He, "Novel surface plasmon waveguide for high integration," *Opt. Express*, vol. 13, no. 17, pp. 6645-6650, Aug. 2005.
- [104] D. F. P. Pile, T. Ogawa, D. K. Gramotnev, Y. Matsuzaki, K. C. Vernon, K. Yamaguchi, T. Okamoto, M. Haraguchi, and M. Fukui, "Two-dimensionally localized modes of a nanoscale gap plasmon waveguide," *Applied Physics Letters*, vol. 87, no. 26, pp. 2611-2614, 2005.
- [105] E. Verhagen, J. A. Dionne, L. K. Kuipers, H. A. Atwater, and A. Polman, "Near-Field visualization of strongly confined surface plasmon polaritons in Metal-Insulator-metal waveguides," *Nano Letters*, vol. 8, no. 9, pp. 2925-2929, Sep. 2008.
- [106] J. Tian, S. Yu, W. Yan, and M. Qiu, "Broadband high-efficiency surface-plasmon-polariton coupler with silicon-metal interface," *Applied Physics Letters*, vol. 95, no. 1, pp. 013504-013506, Jul. 2009.
- [107] A. Yariv, "Coupled-mode theory for guided-wave optics," *Quantum Electronics, IEEE Journal of*, vol. 9, no. 9, pp. 919-933, Sep. 1973.
- [108] R. G. Hunsperger, A. Yariv, and A. Lee, "Parallel end-butt coupling for optical integrated circuits," *Appl. Opt.*, vol. 16, no. 4, pp. 1026-1032, Apr. 1977.

- [109] R. G. Hunsperger, *Integrated Optics*. Berlin: Springer, 1995.
- [110] V. R. Almeida, Q. Xu, C. A. Barrios, and M. Lipson, "Guiding and confining light in void nanostructure," *Opt. Lett.*, vol. 29, no. 11, pp. 1209-1211, Jun. 2004.
- [111] Q. Xu, V. R. Almeida, R. R. Panepucci, and M. Lipson, "Experimental demonstration of guiding and confining light in nanometer-size low-refractive-index material," *Opt. Lett.*, vol. 29, no. 14, pp. 1626-1628, Jul. 2004.
- [112] R. Sun, P. Dong, N.-n. Feng, C.-y. Hong, J. Michel, M. Lipson, and L. Kimerling, "Horizontal single and multiple slot waveguides: optical transmission at  $\lambda = 1550$  nm," *Opt. Express*, vol. 15, no. 26, pp. 17 967-17 972, Dec. 2007.
- [113] A. H. J. Yang, S. D. Moore, B. S. Schmidt, M. Klug, M. Lipson, and D. Erickson, "Optical manipulation of nanoparticles and biomolecules in sub-wavelength slot waveguides," *Nature*, vol. 457, no. 7225, pp. 71-75, Jan. 2009.
- [114] N.-N. Feng, R. Sun, L. C. Kimerling, and J. Michel, "Lossless strip-to-slot waveguide transformer," *Opt. Lett.*, vol. 32, no. 10, pp. 1250-1252, May 2007.
- [115] Z. Wang, N. Zhu, Y. Tang, L. Wosinski, D. Dai, and S. He, "Ultracompact low-loss coupler between strip and slot waveguides," *Opt. Lett.*, vol. 34, no. 10, pp. 1498-1500, May 2009.
- [116] Z. Han and S. He, "Multimode interference effect in plasmonic subwavelength waveguides and an ultra-compact power splitter," *Opt. Commun.*, vol. 278, no. 1, pp. 199-203, Oct. 2007.
- [117] R. A. Wahsheh, Z. Lu, and M. A. Abushagur, "Efficient Couplers and Splitters from Dielectric Waveguides to Plasmonic Waveguides," in *Frontiers in Optics, OSA Technical Digest (CD) (Optical Society of America, 2008)*, paper FThS4.
- [118] K. F. MacDonald, Z. L. Samson, M. I. Stockman, and N. I. Zheludev, "Ultrafast active plasmonics," *Nature Photonics*, vol. 3, no. 1, pp. 55-58, Dec. 2008.
- [119] R. Yang, M. A. Abushagur, and Z. Lu, "Efficiently squeezing near infrared light into a 21nm-by-24nm nanospot," *Opt. Express*, vol. 16, no. 24, pp. 20 142-20 148, Nov. 2008.
- [120] E. Ozbay, "Plasmonics: Merging photonics and electronics at nanoscale dimensions," *Science*, vol. 311, no. 5758, pp. 189-193, Jan. 2006.
- [121] W. L. Barnes, A. Dereux, and T. W. Ebbesen, "Surface plasmon subwavelength optics," *Nature*, vol. 424, no. 6950, pp. 824-830, Aug. 2003.

- [122] P. Ginzburg, D. Arbel, and M. Orenstein, "Gap plasmon polariton structure for very efficient microscale-to-nanoscale interfacing," *Opt. Lett.*, vol. 31, pp. 3288-3290, Nov. 2006.
- [123] F. J. G. Vidal, H. J. Lezec, T. W. Ebbesen, and L. M. Moreno, "Multiple paths to enhance optical transmission through a single subwavelength slit," *Physical Review Letters*, vol. 90, no. 21, pp. 213 901+, May 2003.
- [124] H. J. Lezec, A. Degiron, E. Devaux, R. A. Linke, L. Martin-Moreno, F. J. Garcia-Vidal, and T. W. Ebbesen, "Beaming light from a subwavelength aperture," *Science*, vol. 297, no. 5582, pp. 820-822, Aug. 2002.
- [125] P. Muhlschlegel, H. J. Eisler, O. J. F. Martin, B. Hecht, and D. W. Pohl, "Resonant optical antennas," *Science*, vol. 308, no. 5728, pp. 1607-1609, Jun. 2005.
- [126] J. R. Krenn, A. Dereux, J. C. Weeber, E. Bourillot, Y. Lacroute, J. P. Goudonnet, G. Schider, W. Gotschy, A. Leitner, F. R. Aussenegg, and C. Girard, "Squeezing the optical Near-Field zone by plasmon coupling of metallic nanoparticles," *Physical Review Letters*, vol. 82, no. 12, pp. 2590-2593, Mar. 1999.
- [127] L. Yin, V. K. Vlasko-Vlasov, J. Pearson, J. M. Hiller, J. Hua, U. Welp, D. E. Brown, and C. W. Kimball, "Subwavelength focusing and guiding of surface plasmons," *Nano Letters*, vol. 5, no. 7, pp. 1399-1402, Jun. 2005.
- [128] M. I. Stockman, "Nanofocusing of optical energy in tapered plasmonic waveguides," *Physical Review Letters*, vol. 93, no. 13, pp. 137 404+, Sep. 2004.
- [129] P. Ginzburg and M. Orenstein, "Plasmonic transmission lines: from micro to nano scale with  $\lambda/4$  impedance matching," *Opt. Express*, vol. 15, no. 11, pp. 6762-6767, May 2007.
- [130] G. Gay, O. Alloschery, B. Viaris de Lesegno, C. O'Dwyer, J. Weiner, and H. J. Lezec, "The optical response of nanostructured surfaces and the composite diffracted evanescent wave model," *Nature Physics*, vol. 2, no. 4, pp. 262-267, Mar. 2006.
- [131] P. B. Johnson and R. W. Christy, "Optical constants of the noble metals," *Physical Review B*, vol. 6, no. 12, pp. 4370-4379, Dec. 1972.
- [132] D. F. P. Pile and D. K. Gramotnev, "Adiabatic and nonadiabatic nanofocusing of plasmons by tapered gap plasmon waveguides," *Applied Physics Letters*, vol. 89, no. 4, pp. 041 111+, Jul. 2006.
- [133] G. Veronis and S. Fan, "Modes of subwavelength plasmonic slot waveguides," *J. Lightwave Technol.*, vol. 25, no. 9, pp. 2511-2521, Sep. 2007.

- [134] W. A. Challener, C. Peng, A. V. Itagi, D. Karns, W. Peng, Y. Peng, X. Yang, X. Zhu, N. J. Gokemeijer, Y. T. Hsia, G. Ju, R. E. Rottmayer, M. A. Seigler, and E. C. Gage, "Heat-assisted magnetic recording by a near-field transducer with efficient optical energy transfer," *Nature Photonics*, vol. 3, no. 4, pp. 220-224, Mar. 2009.
- [135] R. Yang and Z. Lu, "Silicon-on-Insulator platform for integration of 3-D nanoplasmonic devices," *Photonics Technology Letters*, IEEE, vol. 23, no. 22, pp. 1652-1654, Nov. 2011.
- [136] D. K. Gramotnev and S. I. Bozhevolnyi, "Plasmonics beyond the diffraction limit," *Nature Photonics*, vol. 4, no. 2, pp. 83-91, Jan. 2010.
- [137] G. I. Stegeman, R. F. Wallis, and A. A. Maradudin, "Excitation of surface polaritons by end-fire coupling," *Opt. Lett.*, vol. 8, no. 7, pp. 386-388, Jul. 1983.
- [138] P. Berini, "Plasmon polariton modes guided by a metal film of finite width," *Opt. Lett.*, vol. 24, no. 15, pp. 1011-1013, Aug. 1999.
- [139] T. Holmgaard, S. I. Bozhevolnyi, L. Markey, and A. Dereux, "Dielectric-loaded surface plasmon-polariton waveguides at telecommunication wavelengths: Excitation and characterization," *Applied Physics Letters*, vol. 92, no. 1, pp. 011 124-011 126, Jan. 2008.
- [140] R. M. Briggs, J. Grandidier, S. P. Burgos, E. Feigenbaum, and H. A. Atwater, "Efficient coupling between Dielectric-Loaded plasmonic and silicon photonic waveguides," *Nano Letters*, vol. 10, no. 12, pp. 4851-4857, Dec. 2010.
- [141] Y. Song, J. Wang, Q. Li, M. Yan, and M. Qiu, "Broadband coupler between silicon waveguide and hybrid plasmonic waveguide," *Opt. Express*, vol. 18, no. 12, pp. 13 173-13 179, Jun. 2010.
- [142] Z. Han, A. Y. Elezzabi, and V. Van, "Experimental realization of subwavelength plasmonic slot waveguides on a silicon platform," *Opt. Lett.*, vol. 35, no. 4, pp. 502-504, Feb. 2010.
- [143] E. Verhagen, M. Spasenović, A. Polman, and L. K. Kuipers, "Nanowire plasmon excitation by adiabatic mode transformation," *Physics Review Letters*, vol. 102, no. 20, pp. 203 904+, May 2009.
- [144] R. Yang, W. Zhao, R. A. Soref, and Z. Lu, "Semiconductor-coated deep subwavelength spoof surface plasmonic waveguide for THz and MIR applications," *Proceedings of SPIE*, vol. 7938, no. 1, pp. 79 380A-79 380A-6, Feb. 2011.

- [145] B. Ferguson and X.-C. Zhang, "Materials for terahertz science and technology," *Nature Materials*, vol. 1, no. 1, pp. 26-33, Sep. 2002.
- [146] P. H. Siegel, "Terahertz technology in biology and medicine," *Microwave Theory and Techniques, IEEE Trans. on*, vol. 52, no. 10, pp. 2438-2447, Oct. 2004.
- [147] M. Tonouchi, "Cutting-edge terahertz technology," *Nature Photonics*, vol. 1, no. 2, pp. 97-105, Feb. 2007.
- [148] T. Ito, Y. Matsuura, M. Miyagi, H. Minamide, and H. Ito, "Flexible terahertz fiber optics with low bend-induced losses," *J. Opt. Soc. Am. B*, vol. 24, no. 5, pp. 1230-1235, May 2007.
- [149] S. P. Jamison, R. W. McGowan, and D. Grischkowsky, "Single-mode waveguide propagation and reshaping of sub-ps terahertz pulses in sapphire fibers," *Applied Physics Letters*, vol. 76, no. 15, pp. 1987-1989, 2000.
- [150] G. Gallot, S. P. Jamison, R. W. McGowan, and D. Grischkowsky, "Terahertz waveguides," *J. Opt. Soc. Am. B*, vol. 17, no. 5, pp. 851-863, May 2000.
- [151] K. Wang and D. M. Mittleman, "Metal wires for terahertz wave guiding," *Nature*, vol. 432, no. 7015, pp. 376-379, Nov. 2004.
- [152] V. Astley, J. Scheiman, R. Mendis, and D. M. Mittleman, "Bending and coupling losses in terahertz wire waveguides," *Opt. Lett.*, vol. 35, no. 4, pp. 553-555, Feb. 2010.
- [153] H. Han, H. Park, M. Cho, and J. Kim, "Terahertz pulse propagation in a plastic photonic crystal fiber," *Applied Physics Letters*, vol. 80, no. 15, pp. 2634-2636, Apr. 2002.
- [154] M. Goto, A. Quema, H. Takahashi, S. Ono, and N. Sarukura, "Teflon photonic crystal fiber as terahertz waveguide," *Japanese J. of Applied Physics*, vol. 43, pp. 317+, Feb. 2004.
- [155] A. Hassani, A. Dupuis, and M. Skorobogatiy, "Porous polymer fibers for low-loss terahertz guiding," *Opt. Express*, vol. 16, no. 9, pp. 6340-6351, Apr. 2008.
- [156] S.-Y. Cho and R. A. Soref, "Low-loss silicide/silicon plasmonic ribbon waveguides for mid- and far-infrared applications," *Opt. Lett.*, vol. 34, no. 12, pp. 1759-1761, Jun. 2009.
- [157] M. Nagel, A. Marchewka, and H. Kurz, "Low-index discontinuity terahertz waveguides," *Opt. Express*, vol. 14, no. 21, pp. 9944-9954, Oct. 2006.

- [158] M. Wächter, M. Nagel, and H. Kurz, "Metallic slit waveguide for dispersion-free low-loss terahertz signal transmission," *Applied Physics Letters*, vol. 90, no. 6, pp. 061 111+, Feb. 2007.
- [159] H. Zhan, R. Mendis, and D. M. Mittleman, "Superfocusing terahertz waves below  $\lambda/250$  using plasmonic parallel-plate waveguides," *Opt. Express*, vol. 18, no. 9, pp. 9643-9650, Apr. 2010.
- [160] R. Collin, *Field theory of guided waves*. New Jersey: IEEE Press, 1991.
- [161] F. J. Garcia-Vidal, L. Martín-Moreno, and J. B. Pendry, "Surfaces with holes in them: new plasmonic metamaterials," *Journal of Optics A: Pure and Applied Optics*, vol. 7, no. 2, pp. S97-S101, Feb. 2005.
- [162] B. Wang, Y. Jin, and S. He, "Design of subwavelength corrugated metal waveguides for slow waves at terahertz frequencies," *Appl. Opt.*, vol. 47, no. 21, pp. 3694-3700, Jul. 2008.
- [163] Quality Factor Calculations by Lumerical FDTD Solutions. Available: [http://docs.lumerical.com/en/fdtd/cavity\\_q\\_calculation.html](http://docs.lumerical.com/en/fdtd/cavity_q_calculation.html)
- [164] Y.-S. Lee, *Principles of Terahertz Science and Technology*, Springer, 2009, ch. 5.
- [165] R. Yang, X. Huang, and Z. Lu, "Arbitrary super surface modes bounded by multilayered metametal," *Micromachines*, vol. 3, no. 1, pp. 45-54, Feb. 2012.
- [166] D. R. Smith and D. Schurig, "Electromagnetic wave propagation in media with indefinite permittivity and permeability tensors," *Physical Review Letters*, vol. 90, no. 7, pp. 077 405+, Feb. 2003.
- [167] Z. Shi, G. Piredda, A. C. Liapis, M. A. Nelson, L. Novotny, and R. W. Boyd, "Surface-plasmon polaritons on metal-dielectric nanocomposite films," *Opt. Lett.*, vol. 34, no. 22, pp. 3535-3537, Nov. 2009.
- [168] M. Beruete, M. Navarro-Cía, and M. Sorolla, "Strong lateral displacement in polarization anisotropic extraordinary transmission metamaterial," *New J. of Physics*, vol. 12, no. 6, pp. 063 037+, Jun. 2010.
- [169] R. Nielsen, M. Thoreson, W. Chen, A. Kristensen, J. Hvam, V. Shalaev, and A. Boltasseva, "Toward superlensing with metal-dielectric composites and multilayers," *Applied Physics B: Lasers and Optics*, vol. 100, no. 1, pp. 93-100, Jul. 2010.

- [170] B. Wood, J. B. Pendry, and D. P. Tsai, "Directed subwavelength imaging using a layered metal-dielectric system," *Physical Review B*, vol. 74, no. 11, pp. 115 116+, Sep. 2006.
- [171] K. J. Webb and M. Yang, "Subwavelength imaging with a multilayer silver film structure," *Opt. Lett.*, vol. 31, no. 14, pp. 2130-2132, Jul. 2006.
- [172] Z. Jacob, L. V. Alekseyev, and E. Narimanov, "Optical hyperlens: Far-field imaging beyond the diffraction limit," *Opt. Express*, vol. 14, no. 18, pp. 8247-8256, Sep. 2006.
- [173] Z. Liu, H. Lee, Y. Xiong, C. Sun, and X. Zhang, "Far-Field optical hyperlens magnifying Sub-Diffraction-limited objects," *Science*, vol. 315, no. 5819, p. 1686, Mar. 2007.
- [174] Y. Xiong, Z. Liu, C. Sun, and X. Zhang, "Two-Dimensional imaging by Far-Field superlens at visible wavelengths," *Nano Letters*, vol. 7, no. 11, pp. 3360-3365, Oct. 2007.
- [175] C. H. Gan and P. Lalanne, "Well-confined surface plasmon polaritons for sensing applications in the near-infrared," *Opt. Lett.*, vol. 35, no. 4, pp. 610-612, Feb. 2010.
- [176] S. Kawakami, "Light propagation along periodic metal-dielectric layers," *Appl. Opt.*, vol. 22, no. 16, pp. 2426-2428, Aug. 1983.
- [177] T. Davis, "Surface plasmon modes in multi-layer thin-films," *Opt. Commun.*, vol. 282, pp. 135-140, Oct. 2008.
- [178] A. V. Kildishev, W. Cai, U. K. Chettiar, H.-K. Yuan, A. K. Sarychev, V. P. Drachev, and V. M. Shalaev, "Negative refractive index in optics of metal-dielectric composites," *J. Opt. Soc. Am. B*, vol. 23, no. 3, pp. 423-433, Mar. 2006.
- [179] I. Avrutsky, I. Salakhutdinov, J. Elser, and V. Podolskiy, "Highly confined optical modes in nanoscale metal-dielectric multilayers," *Physical Review B*, vol. 75, pp. 241 402+, Jun. 2007.
- [180] J. Elser, A. A. Govyadinov, I. Avrutsky, I. Salakhutdinov, and V. A. Podolskiy, "Plasmonic nanolayer composites: coupled plasmon polaritons, effective-medium response, and subdiffraction light manipulation," *J. Nanomaterials*, vol. 2007, p. 7, Jan. 2007.
- [181] J. Elser, V. A. Podolskiy, I. Salakhutdinov, and I. Avrutsky, "Nonlocal effects in effective-medium response of nanolayered metamaterials," *Applied Physics Letters*, vol. 90, no. 19, pp. 191 109+, 2007.

- [182] S. Hyun Nam, E. Ulin-Avila, G. Bartal, and X. Zhang, "Deep subwavelength surface modes in metal-dielectric metamaterials," *Opt. Lett.*, vol. 35, no. 11, pp. 1847-1849, Jun. 2010.
- [183] B. E. A. Saleh and M. C. Teich, "Photonic-Crystal Optics," in *Fundamentals of Photonics*, 2nd ed. Hoboken, NJ: Wiley-Interscience, 2007, pp. 246–253.
- [184] A. Ghatak, K. Thyagarajan, and M. Shenoy, "Numerical analysis of planar optical waveguides using matrix approach," *Lightwave Technology, Journal of*, vol. 5, no. 5, pp. 660-667, May 1987.
- [185] E. Anemogiannis, E. N. Glytsis, and T. K. Gaylord, "Determination of guided and leaky modes in lossless and lossy planar multilayer optical waveguides: reflection pole method and wavevector density method," *Lightwave Technology, Journal of*, vol. 17, no. 5, pp. 929-941, May 1999.
- [186] J. Chilwell and I. Hodgkinson, "Thin-films field-transfer matrix theory of planar multilayer waveguides and reflection from prism-loaded waveguides," *J. Opt. Soc. Am. A*, vol. 1, no. 7, pp. 742-753, Jul. 1984.
- [187] Sophocles J. Orfanidis, *Electromagnetic Waves and Antennas*, Ch. 7, <http://eceweb1.rutgers.edu/~orfanidi/ewa/>, retrieved in Sept. 2012.
- [188] G. J. Kovacs and G. D. Scott, "Optical excitation of surface plasma waves in layered media," *Physical Review B*, vol. 16, pp. 1297-1311, Aug. 1977.
- [189] COMSOL Multiphysics 3.3 (2007), COMSOL Inc. Available: <http://www.comsol.com>
- [190] M. L. Brongersma and V. M. Shalaev, "The case for plasmonics," *Science*, vol. 328, no. 5977, pp. 440-441, Apr. 2010.
- [191] K. F. MacDonald and N. I. Zheludev, "Active plasmonics: current status," *Laser & Photon. Rev.*, vol. 4, no. 4, pp. 562-567, 2010.
- [192] R. F. Oulton, V. J. Sorger, T. Zentgraf, R.-M. Ma, C. Gladden, L. Dai, G. Bartal, and X. Zhang, "Plasmon lasers at deep subwavelength scale," *Nature*, vol. 461, no. 7264, pp. 629-632, Oct. 2009.
- [193] A. Akbari, R. N. Tait, and P. Berini, "Surface plasmon waveguide schottky detector," *Opt. Express*, vol. 18, no. 8, pp. 8505-8514, Apr. 2010.
- [194] V. E. Ferry, L. A. Sweatlock, D. Pacifici, and H. A. Atwater, "Plasmonic nanostructure design for efficient light coupling into solar cells," *Nano Letters*, vol. 8, no. 12, pp. 4391-4397, Dec. 2008.

- [195] S. Zhu, G. Q. Lo, and D. L. Kwong, "Theoretical investigation of silicide schottky barrier detector integrated in horizontal metal-insulator-silicon-insulator-metal nanoplasmonic slot waveguide," *Opt. Express*, vol. 19, no. 17, pp. 15 843-15 854, Aug. 2011.
- [196] I. Goykhman, B. Desiatov, J. Khurgin, J. Shappir, and U. Levy, "Locally oxidized silicon Surface-Plasmon schottky detector for telecom regime," *Nano Letters*, vol. 11, no. 6, pp. 2219-2224, Jun. 2011.
- [197] L. Esaki and Y. Miyahara, "A new device using the tunneling process in narrow p-n junctions," *Solid-State Electronics*, vol. 1, no. 1, pp. 13-21, Mar. 1960.
- [198] P. C. D. Hobbs, R. B. Laibowitz, F. R. Libsch, N. C. LaBianca, and P. P. Chiniwalla, "Efficient waveguide-integrated tunnel junction detectors at 1.6  $\mu\text{m}$ ," *Opt. Express*, vol. 15, no. 25, pp. 16 376-16 389, Dec. 2007.
- [199] J. Zhao, "24.5% efficiency pert silicon solar cells on seh mcz substrates and cell performance on other seh cz and fz substrates," *Solar Energy Materials and Solar Cells*, vol. 66, no. 1-4, pp. 27-36, February 2001.
- [200] A. Goetzberger and V. U. Hoffmann, *Photovoltaic Solar Energy Generation*, Goetzberger, Ed., 2005.
- [201] A. Shah, P. Torres, R. Tscharnner, N. Wyrsh, and H. Keppner, "Photovoltaic technology: The case for thin-film solar cells," *Science*, vol. 285, no. 5428, pp. 692-698, July 1999.
- [202] R. B. Bergmann, "Crystalline si thin-film solar cells: a review," *Applied Physics A: Materials Science & Processing*, vol. 69, no. 2, pp. 187-194, August 1999.
- [203] Z. Lu and W. Zhao, "Nanoscale electro-optic modulators based on graphene-slot waveguides," *J. Opt. Soc. Am. B*, vol. 29, no. 6, pp. 1490-1496, Jun. 2012.
- [204] A. Sanchez, C. F. Davis, K. C. Liu, and A. Javan, "The MOM tunneling diode: Theoretical estimate of its performance at microwave and infrared frequencies," *J. of Applied Physics*, vol. 49, no. 10, pp. 5270-5277, Oct. 1978.
- [205] M. R. Abdel-Rahman, F. J. González, and G. D. Boreman, "Antenna-coupled metal-oxide-metal diodes for dual-band detection at 92.5 GHz and 28 THz," *Electronics Letters*, vol. 40, no. 2, pp. 116+, 2004.
- [206] J. A. Bean, "Thermal Infrared Detection Using Antenna-Coupled Metal-Oxide-Metal Diodes," *Ph.D. dissertation*, Dept. Elect. Eng., Univ. of Notre Dame, Notre Dame, IN, US, 2009.

- [207] A. Kobayakov, A. Mafi, A. R. Zakharian, S. A. Darmanyany, and K. B. Sparks, "Fundamental and higher-order bloch surface plasmons in planar bimetallic gratings on silicon and glass substrates," *J. Opt. Soc. Am. B*, vol. 25, no. 9, pp. 1414-1421, Sep. 2008.
- [208] S. A. Maier and H. A. Atwater, "Plasmonics: Localization and guiding of electromagnetic energy in metal/dielectric structures," *J Appl Phys*, vol. 98, no. 1, pp. 1-10, 2005.
- [209] S. H. Lim, W. Mar, P. Matheu, D. Derkacs, and E. T. Yu, "Photocurrent spectroscopy of optical absorption enhancement in silicon photodiodes via scattering from surface plasmon polaritons in gold nanoparticles," *Journal of Applied Physics*, vol. 101, no. 10, pp. 104 309+, 2007.
- [210] C. Rockstuhl, S. Fahr, and F. Lederer, "Absorption enhancement in solar cells by localized plasmon polaritons," *Journal of Applied Physics*, vol. 104, no. 12, pp. 123 102+, 2008.
- [211] K. Yamamoto, M. Yoshimi, Y. Tawada, Y. Okamoto, A. Nakajima, and S. Igari, "Thin-film poly-si solar cells on glass substrate fabricated at low temperature," *Applied Physics A: Materials Science & Processing*, vol. 69, no. 2, pp. 179-185, August 1999.
- [212] B. P. Rand, P. Peumans, and S. R. Forrest, "Long-range absorption enhancement in organic tandem thin-film solar cells containing silver nanoclusters," *Journal of Applied Physics*, vol. 96, no. 12, pp. 7519-7526, 2004.
- [213] S. Pillai, K. R. Catchpole, T. Trupke, and M. A. Green, "Surface plasmon enhanced silicon solar cells," *Journal of Applied Physics*, vol. 101, no. 9, pp. 093 105+, 2007.
- [214] P. N. Saeta, V. E. Ferry, D. Pacifici, J. N. Munday, and H. A. Atwater, "How much can guided modes enhance absorption in thin solar cells?" *Opt. Express*, vol. 17, no. 23, pp. 20 975-20 990, Nov. 2009.
- [215] Renewable Resource Data Center, "Reference Solar Spectral Irradiance: ASTM G-173," <http://rredc.nrel.gov/solar/spectra/am1.5/ASTMG173/ASTMG173.html>
- [216] M. Schnell, A. Garcia-Etxarri, A. J. Huber, K. Crozier, J. Aizpurua, and R. Hillenbrand, "Controlling the near-field oscillations of loaded plasmonic nanoantennas," *Nat Photon*, vol. 3, no. 5, pp. 287-291, May 2009.

---

## 10 APPENDICES

---

### 10.A Analytical solution of MIM waveguide

```
% 4/24/12
% fundamental TM mode, 2d mim waveguide calculation

function [gamma_c,km,kd] = waveguide_mim(d,epsm,epsd)

nm = 1e-9; c=299792458;
lambda = 1550*nm;
omega = 2*pi*c/lambda;
k=omega/c;

gamma=zeros(1,2*length(d));
start = [0;2];
options=optimset('TolFun',1e-16,'MaxFunEvals',1024);
for ii=1:length(d)
[gamma,fval] = fsolve(@(gamma) ...
    [real(tanh(sqrt(epsd-(-j*gamma(1)+gamma(2))^2)/j*k*d(ii)/2) -
sqrt(epsm-(-j*gamma(1)+gamma(2))^2)...
    ./ sqrt(epsd-(-j*gamma(1)+gamma(2))^2) ...
    * epsd/epsm);
    imag(tanh(sqrt(epsd-(-j*gamma(1)+gamma(2))^2)/j*k*d(ii)/2) -
sqrt(epsm-(-j*gamma(1)+gamma(2))^2)...
    ./ sqrt(epsd-(-j*gamma(1)+gamma(2))^2) ...
    * epsd/epsm)],start,options);
% [gamma,fval] = fsolve(@disp_func_mim_multi,start,options);
alfa(ii)=gamma(1);
beta(ii)=gamma(2);
gamma_c(ii) = alfa(ii)+beta(ii)*j;
km(ii) = sqrt(epsm-(-j*gamma(1)+gamma(2))^2)/j;
kd(ii) = sqrt(epsd-(-j*gamma(1)+gamma(2))^2)/j;
end
```

### 10.B Matlab code to implement transfer matrix method, single layer case

```
% 4/24/12
% transfer matrix review for off-axis SPR
% Simple case, prism-coating-substrate
% clc;clear;
% Constant
c = 299792458;
nGlass = sqrt(2.1);
n_Ag500 = (sqrt(-8.56-1i*0.6225));
nAir = 1.0;

% Material and Spectrum Definition. lambda = 500 nm
lambda = 500e-9; k=2*pi/lambda;
nin = nGlass;
nout = nAir;

% Structure Definition, d1 as n1's thickness
```

```

din = 0;
dl = 20e-9;

% Input Angle tin for theta_input
t = linspace(20,90,200);
tin = t/180*pi;

% t calculation
% cost1 for cos(t1), costout for cos(tout)
cost1 = (sqrt(1-(nin/nl.*sin(tin)).^2));
costout = conj(sqrt(1-(nin/nout .*sin(tin)).^2));

% 1. Phase term f for phi and
% 2. polarization based ref. index np for n_prime related to
polarization
% 3. a factor
% Details seen in p253, Salen and Teich, 2nd Ed
% TM polarization
% Two interfaces case, described by 7.1-27
fin = nin*k*din.*cos(tin);
f1 = nl*k*dl.*cost1;
npin = nin./cos(tin);
npl = nl./cost1;
npout = (nout./costout);
ain = (cos(tin)./cost1);%a12
aout = ((cost1)./ costout);%a21

% Setup Matrix, Min and Mout
M11 = (npl+npin)/2./npl .*ain;
M12 = (npl-npin)/2./npl .*ain;
M21 = (npl-npin)/2./npl .*ain;
M22 = (npl+npin)/2./npl .*ain;
Min11 = M11; %.* exp(-li*fin);
Min12 = M12; %.* exp(+li*fin);
Min21 = M21;%.* exp(-li*fin);
Min22 = M22; %.* exp(+li*fin);

M11 = (npl+npout) /2.*aout./npout;
M12 = (npout-npl) /2.*aout./npout;
M21 = (npout-npl) /2.*aout./npout;
M22 = (npl+npout) /2.*aout./npout;
Mout11 = M11.* exp(-li*f1);
Mout12 = M12.* exp((+li*(f1)));
Mout21 = M21.* exp(-li*f1);
Mout22 = M22.* exp((+li*(f1)));

% Calculation
M11 = Mout11.* Min11 + Mout12 .* Min21;
M12 = Mout11.* Min12 + Mout12 .* Min22;
M21 = Mout21.* Min11 + Mout22 .* Min21;
M22 = Mout21.* Min12 + Mout22 .* Min22;

S11 = (M11.*M22-M12.*M21)./M22;
S12 = M12./M22;
S21 = -M21./M22;

```

```
S22 = 1./M22;

% Plot
figure(1), plot(t,abs(S21).^2,'--'); hold on
plot(t,abs(S11).^2.*real(nout.*costout/nin./cos(tin)),'--r'); holdoff
curve = abs(S21).^2;
spr=find(curve==min(curve))
```